

UNIVERSITÀ DEGLI STUDI DI PADOVA

Dipartimento di Fisica e Astronomia “Galileo Galilei”

Master Degree in Physics

Final Dissertation

Lattice QED photonic wavepackets on ladder geometries

Thesis supervisor

Prof. Pietro Silvi

Thesis co-supervisor

Prof. Simone Montangero

Candidate

Mattia Morgavi

Academic Year 2022/2023

Abstract

In this thesis we explore numerical simulations, including Tensor Networks (TNs) methods, to study Hamiltonian Lattice Gauge Theories (LGTs), a numerical framework for investigating non-perturbative properties of Quantum Field Theories. We develop a model-independent approach for constructing Matrix Product Operators (MPOs) representations of one-dimensional quasiparticles with definite momenta, and apply it to Hamiltonian Lattice Quantum Electrodynamics (QED) on a ladder geometry. By means of exact diagonalization at intermediate system sizes, we obtain the first excitation band states (the Bloch functions) representing the single-(quasi)particle states (the photons) expressed as entangled states of local lattice gauge fields. We then construct the corresponding maximally-localized Wannier functions through minimization of a spread functional. Once we identify, via a linear algebra problem, the operation that constructs the localized Wannier excitation from the ground state (dressed vacuum), we can express the creation operator, for any wave-packet of such quasiparticles, as a Matrix Product Operator. The aforementioned steps constitute a constructive strategy to prepare an arbitrary input state for a quasiparticle scattering simulation in real time, and the scattering process itself can be carried out with any standard algorithm for time-evolution with Matrix Product States.

Table of contents

| | |
|---|----|
| Abstract | 3 |
| Introduction | 9 |
| Lattice Gauge Theories | 10 |
| The arise of quantum technologies | 10 |
| Content of the thesis | 12 |
| 1 Theoretical Background | 15 |
| 1.1 Classical and quantum electrodynamics in vacuum | 15 |
| 1.1.1 Electrodynamics in (3+1) dimensions | 15 |
| 1.1.2 Electrodynamics in (2+1) dimensions | 16 |
| 1.1.3 Canonical quantization of the gauge fields | 17 |
| 1.2 The (2+1)-dimensional Lattice QED | 18 |
| 1.2.1 Wilson loops | 19 |
| 1.2.2 The Kogut-Susskind Hamiltonian | 21 |
| 1.2.3 Quantization of the lattice link variables | 22 |
| 1.2.4 Gauge invariance: the Gauss' Law | 23 |
| 1.3 The Quantum Link Model | 25 |
| 1.3.1 Mapping link operators to spin operators | 25 |
| 1.3.2 QLM spin notation and the Gauss' Law | 26 |
| 2 Pure Lattice QED on ladder geometries | 29 |
| 2.1 The ladder geometry | 29 |
| 2.2 The Quantum Link Model on the Ladder | 31 |
| 2.2.1 Gauss' Law and the problem of the spin representation | 32 |
| 2.2.2 The local plaquette basis | 34 |
| 2.2.3 The rules for neighboring plaquettes | 35 |
| 2.2.4 The longitudinal polarization sectors | 36 |
| 2.3 Counting the gauge invariant configurations | 37 |
| 2.3.1 Example with $\left(\frac{1}{2}, 1\right)$ | 39 |
| 2.3.2 Higher spin representations | 40 |
| 2.3.3 The case $(n/2, n)$ | 41 |
| 2.4 Construction of the operators | 42 |
| 2.4.1 The translation operator \hat{T} | 43 |

| | | |
|----------|---|-----------|
| 2.4.2 | Reflection operators \hat{R} and \hat{F} | 44 |
| 2.4.3 | The Hamiltonian operator \hat{H} | 45 |
| 2.4.4 | The local Hamiltonian operators \hat{H}_j | 46 |
| 2.5 | The energy-momentum dispersion relation | 46 |
| 2.5.1 | Dispersion relation in a continuous quantum field theory | 47 |
| 2.5.2 | Dispersion relation in a lattice theory | 48 |
| 2.5.3 | The tight binding condition | 49 |
| 2.5.4 | Dispersion relations of the ladder system | 50 |
| | Lowest spin representation $\left(\frac{1}{2}, 1\right)$ | 51 |
| | The spin representations $(1, 1), (1, 2)$ | 53 |
| | The case $s_x = 3/2$ and higher spin representations | 54 |
| 2.6 | Mapping $\left(\frac{1}{2}, 1\right)$ ladder to 1D Ising transverse field | 55 |
| 2.6.1 | The Ising Model with a transverse field | 56 |
| 2.6.2 | Mapping between Hilbert spaces | 57 |
| 2.6.3 | Electric term \hat{H}_E mapped to the Ising interaction term | 58 |
| 2.6.4 | Magnetic term \hat{H}_B mapped to the transverse field term | 59 |
| 2.6.5 | Phases and critical point | 60 |
| 2.6.6 | Hints about mapping for higher spin representations | 61 |
| 3 | Creation of the photonic wave-packets | 63 |
| 3.1 | The first energy band states | 64 |
| 3.1.1 | First energy band estimation for $\left(\frac{1}{2}, 1\right)$ with $g \rightarrow 0$ | 64 |
| 3.1.2 | Perturbative correction of the first energy band | 65 |
| 3.1.3 | Simultaneous diagonalization of \hat{H} and \hat{T} | 66 |
| 3.1.4 | Energy estimations of the first band for low g | 68 |
| 3.1.5 | Symmetry properties of the Bloch vectors | 69 |
| 3.2 | Maximally localized Wannier States | 70 |
| 3.2.1 | Symmetrization of the Bloch states | 71 |
| 3.2.2 | Wannier Functions: definition and properties | 71 |
| 3.2.3 | The energy spread functional | 72 |
| 3.2.4 | Minimizing the functional $f(\boldsymbol{\theta})$ | 75 |
| 3.2.5 | Optimize the computation of $\Lambda_{kk'}$ | 76 |
| 3.2.6 | Maximally localized Wannier states for $\left(\frac{1}{2}, 1\right)$ with $g \rightarrow 0$ | 76 |
| 3.2.7 | Numerical results for $\left(\frac{1}{2}, 1\right)$ with finite g | 77 |
| 3.3 | Constructing the excitation operator \hat{W} | 78 |
| 3.3.1 | Presentation of the problem | 79 |
| 3.3.2 | The operator in the case $\left(\frac{1}{2}, 1\right)$ and $g \rightarrow 0$ | 79 |
| 3.3.3 | A general numerical method | 80 |
| 3.3.4 | Application to $\left(\frac{1}{2}, 1\right)$ with $g \rightarrow 0$ | 82 |
| 3.3.5 | Numerical results for $\left(\frac{1}{2}, 1\right)$, small g and $L = 3$ | 83 |

| | | |
|----------|---|------------|
| 3.3.6 | Increasing the Wannier support up to $L = 13$ | 84 |
| 3.3.7 | Higher spin representations and other lattice models | 85 |
| 3.4 | The wave-packet creation operator $\hat{\Psi}$ | 86 |
| 3.4.1 | Wave-packet state $ \Psi\rangle$ from the Wannier states $ W_j\rangle$ | 86 |
| 3.4.2 | The Gaussian wave-packet | 87 |
| 3.4.3 | Wave-packet operator $\hat{\Psi}$ from the excitation operators \hat{W}_j | 88 |
| 4 | Tensor Network Methods | 89 |
| 4.1 | The Tensor Network notation | 89 |
| 4.1.1 | Notation for quantum systems | 91 |
| 4.2 | Matrix Product States and Operators | 91 |
| 4.2.1 | Matrix Product States | 91 |
| 4.2.2 | Matrix Product Operators | 92 |
| 4.2.3 | The Matrix picture | 94 |
| 4.2.4 | The Automata picture | 96 |
| 4.3 | Density Matrix Renormalization Group | 98 |
| 4.4 | Time evolution of MPS | 99 |
| 4.5 | TNs for higher-dimensional systems | 101 |
| 4.5.1 | MPS for quasi one-dimensional systems | 101 |
| 4.5.2 | Other TN structures for higher-dimensional systems | 102 |
| 5 | Numerical Simulations | 105 |
| 5.1 | TN representations and ground-state search | 105 |
| 5.1.1 | Represent the system as an MPS: the local basis choice | 105 |
| 5.1.2 | The total and local Hamiltonian MPOs for $(\frac{1}{2}, 1)$ | 107 |
| 5.1.3 | Ground-state search with MPS-DMRG | 108 |
| 5.2 | MPO wave-packet operator construction for $(\frac{1}{2}, 1)$ | 109 |
| 5.2.1 | Example of automata picture for $\hat{\Psi}$ with $w = 3$ | 109 |
| 5.2.2 | Generalization to higher w and built-in functions methods | 111 |
| 5.3 | Real-time simulations of the $(\frac{1}{2}, 1)$ ladder | 111 |
| 5.3.1 | Preparation of the initial states | 112 |
| 5.3.2 | Performing time evolution with TEBD | 113 |
| 5.3.3 | Dispersion of the localized Wannier state | 115 |
| 5.3.4 | Propagation of a single particle wave-packet | 116 |
| 5.3.5 | Photon-photon scattering | 121 |
| 6 | Conclusion and Outlook | 125 |
| | Bibliography | 127 |

Introduction

In the past century, the framework of *Quantum Field Theories* (QFTs) allowed physicists to model and analyze the quantum nature of fields and particles [1]. *Gauge theories* are a specific class of QFTs that play a fundamental role in modern theoretical physics. At its core, a gauge theory describes the dynamics of fields that possess a certain continuous *local symmetry*, described by a so-called *gauge group* G [2]. Gauge field theories provide a unified framework for matter, radiation, and their mutual interaction.

The most important application of gauge theories is the *Standard Model* (SM) of particle physics, which describes the fundamental *fermionic particles* (the matter) and their interactions through the exchange of force-carrying particles, the *gauge bosons* [2]. The SM, with a unifying insight, explains the electromagnetic, weak and strong interactions, reproducing a plethora of observed phenomena with outstanding precision.

Since the first formulations of QFTs, *scattering processes* in particle physics have been the standard experiments to discover new physics and validate the correctness of the theoretical particle models. By examining the interactions between particles during scattering processes, physicists can compare theoretical predictions with experimental data at increasing energy scales, providing critical insights into the underlying accuracy of the model.

In the early development stage of QFTs, physicists primarily relied on *perturbative methods* to theoretically compute observables from scattering processes (e.g. Feynman diagrams). For instance, in Quantum Electrodynamics (QED), which describes the electromagnetic interactions between charged particles (electrons and positrons) and photons, perturbation theory has been remarkably successful in predicting cross-sections and amplitudes, to an extremely high degree of accuracy.

However, the perturbative approaches encountered limitations when dealing with certain QFTs, most notably *Quantum Chromodynamics* (QCD) [2], the theory describing the *strong force*, which governs interactions between gluons and quarks, binding the latter into *hadrons* (protons, neutrons, etc.). Thanks to the *asymptotic freedom*, perturbative QCD can be used efficiently at high energies, but at low energies and large distances, non-perturbative phenomena starts to arise [3]. In particular, the study of QCD out-of-equilibrium real-time evolution of mesons and heavy-ions collision processes require more

modern and advanced *non-perturbative methods*.

Lattice Gauge Theories To overcome non-perturbative challenges in quantum field theories, two approaches are employed. The first is *exact analytical* methods, which offer rigorous solutions but are limited in their applicability to a restricted class of systems (e.g. integrable systems [4]). The second approach involves *numerical methods*.

In the latter context, *Lattice Gauge Theories* (LGTs) [5, 6] were introduced by K. G. Wilson [7], approximating spacetime by a *discrete lattice*, which transforms continuous field variables into lattice operators. While this approach enables numerical simulations and circumvents some perturbative issues, it introduces significant *computational challenges*: as the lattice size increases, the computational resources required for simulations grow *exponentially*, as a quantum many-body system. This makes almost impossible to tackle the thermodynamic limit: a large system would require more than the world's technological capacity to compute information [8].

At the early stages of LGTs, *Monte Carlo methods* became the main tool to address these numerical challenges [9]. By employing *stochastic sampling* of field configurations on the lattice, Monte Carlo simulations offer a numerical approach to study gauge theories beyond perturbation theory. This approach has proven essential for understanding *confinement* and computing the *masses of hadrons* [10] in the context of low-energy non-perturbative QCD.

However, the main problem of Monte Carlo simulations in *fermionic lattice gauge theories* is the *sign problem* [11]: the contribution of fermionic degrees of freedom makes the path integral oscillatory, and the cancellation of positive and negative contributions hinders the convergence of the simulations [12]. Furthermore, Monte Carlo methods cannot simulate efficiently out-of-equilibrium processes, such as the scattering processes. Therefore, since the early days of LGTs, researchers have been actively exploring also *alternative approaches* to address these limitations.

The arise of quantum technologies In the meantime, the field of *Quantum information theory* [13] has seen a rapid development, leading to various technologies with applications in computation, simulation [14], communication [15], and sensing [16]. *Quantum technologies* have promising applications in scientific fields such as high-energy physics, nuclear physics, condensed matter physics, and quantum chemistry. In this context, quantum technologies has found applications in Lattice Gauge Theory [17] through two different approaches: *quantum simulators* [18] and *Tensor Networks* (TNs) [19] (Fig. 1).

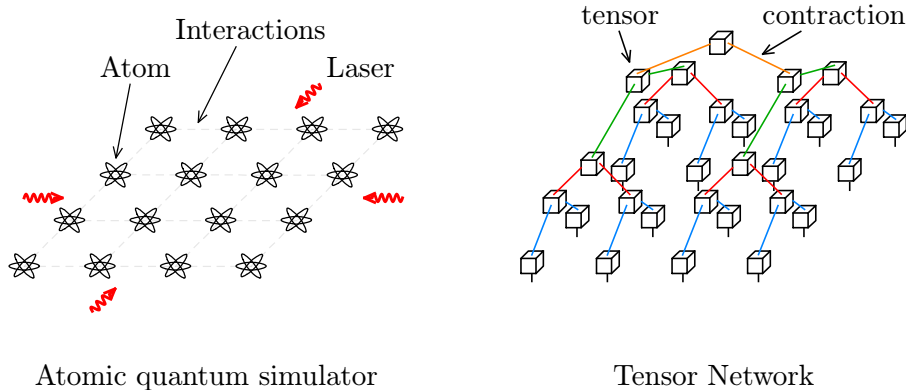


Figure 1. On the left, a graphical representation of a 2D Atomic Quantum Simulator in an optical lattice, where finely tuned atomic systems allows emulating quantum phenomena. On the right, a depiction of a 2D Tree Tensor Network, a linear algebra framework useful to efficiently represent quantum states.

One of the first insights into overcome quantum simulation problems exploiting quantum systems is attributed to R. P. Feynman in his seminal paper [20]. By analog or digital *quantum simulation* [21] we mean simulating a quantum system using *quantum devices*, such as trapped ions [22], superconducting circuits [23, 24], and neutral ultracold atoms systems [18, 25], which can be engineered and finely tuned to mimic the behavior of quantum system such as LGT models. These *quantum platforms* allow researchers to directly study the real-time dynamics of gauge fields and fermionic matter fields [26].

In this context, quantum simulation has recently revitalized interest in the *Hamiltonian formulation* of LGTs, introduced by S. Kogut and L. Susskind in the seventies [27, 28], which was overlooked since Monte Carlo methods favored the Lagrangian formalism of LGTs. The Hamiltonian formulation is well-suited for quantum information devices because it naturally describes the real-time dynamics of quantum systems.

Consequently, several other formulations of LGTs as the *Quantum Link Model* (QLM) [29] were developed as a way to bridge LGTs with spin systems. The QLM formulation provides a mapping from lattice operators to spin operators, making it amenable for efficient representation and simulation of abelian and non-abelian gauge theories using quantum information tools. The discrete configuration space of QLMs offers potential advantages in numerical and quantum simulations compared to ordinary LGTs with continuous configuration spaces [29].

Since quantum computers and quantum simulators are still at the early stages [30], alternative tools of numerical quantum information theory were developed, such as the *Tensor Network* (TN) framework [31], which will be the numerical method used in this thesis work. TNs have been proven to efficiently represent the quantum states of strongly correlated many-body quantum systems, *compressing* information using different structures of tensor contractions.

Tensor Networks, leveraging the *area law of entanglement* [32], can efficiently represent quantum states with enough low entanglement with computational cost that scales

with the system size, making them a powerful tools for simulating large-scale quantum systems, easily approaching the thermodynamic limit. In particular, quantum states of 1-dimensional systems are efficiently and naturally represented by Matrix Product States [33] (MPS) structures.

TN methods applied to LGTs offer several advantages over Monte Carlo methods: first, TNs are *sign-problem free* [34], enabling exploration of *high-baryon density phases* of QCD (e.g. quark-gluon plasma [35] and color superconductor phase [36]) which are instead very challenging for Monte Carlo simulations; secondly, TNs can perform *real-time simulations* [37], allowing investigations into out-of equilibrium dynamical phenomena such as non-perturbative scattering processes [38].

Although one of the primary goals of TN methods remains to simulate the realistic $(3+1)$ -D QCD, this non-abelian theory possess a too large number of local degrees of freedom in order to be simulated using current TN techniques. As a result, initially the researchers focused on *lower-dimensional abelian LGTs*, which are more manageable and served as a “stepping stone” to develop the necessary techniques to tackle more realistic models.

In the past decade, TN methods have been extensively applied to the well-known 1D LGTs such as the *lattice Schwinger model* [39], benchmarking the results with the theoretical predictions. While MPS is particularly well-suited TN structure for $(1+1)$ -D systems [33], also $(2+1)$ -D and $(3+1)$ -D abelian theories [40] have been studied using different higher-dimensional TN structures (PEPS, TTN and MERA). Furthermore, the ground-state properties and the phase diagram of $(1+1)$ -D non-abelian [41], and more recently, $(2+1)$ -D non-abelian LGTs were studied with TNs [42].

Content of the thesis

Although equilibrium properties of LGTs were studied, real-time scattering processes were not widely considered, mainly because of the lack of a model-independent approach to prepare initial single 1-dimensional (quasi)-particle wave-packet states with *definite size and momenta* using TNs. Recently, this problem was addressed for generic 1D quantum spin chains [43], constructing MPS of 1D quasiparticles wave-packets, while a particular approach have been studied for $(1+1)$ -D Hamiltonian QED (the lattice Schwinger model) [44].

In this work, we present a model-independent method to construct generic 1-dimensional single-particle wave-packet MPS state. This method employs an initial exact diagonalization step, followed by the localization of Wannier functions [45, 46]. To show the validity of the model, we apply it to a toy model, specifically the QLM formulation of the Hamiltonian LGT of the pure¹ QED in a quasi-1-dimensional lattice geometry: *the two-leg ladder*, which is becoming popular in recent years [47, 48]. In particular, we construct single-

1. Without fermion field, i.e. without electrons and positrons, so without matter. Actually, this condition can be in principle obtained from lattice QED with matter, setting the bare mass of the electron to infinity.

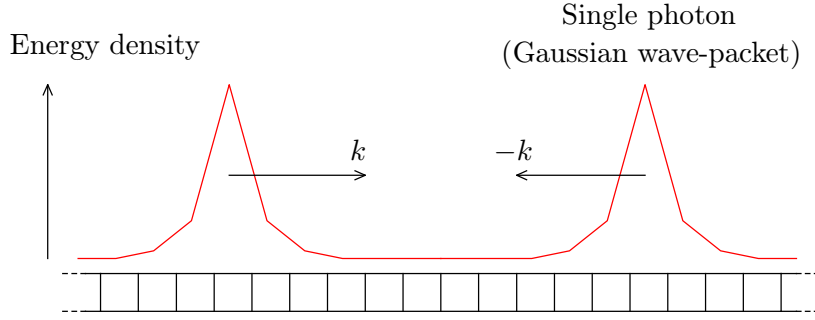


Figure 2. Energy density profile of an initial scattering state in the Hamiltonian QED on a ladder geometry. The plot depicts two Gaussian wave-packets with opposite momenta, representing prepared states ready for the scattering simulation.

particle *photonic gaussian wave-packets* of this theory, and we simulate different processes such as a single-photon propagation and *photon-photon scattering* (Fig. 2).

In the context of the true $(3 + 1)$ -dimensional QED (with matter-light interaction) it is known that the photons can effectively weakly self-interact because of the 1-loop contributions:

(1)

However, the photon-photon scattering is a marginal process because the S -matrix element given by the contribution of the amplitude (1) is small if compared to other scattering processes. Moreover, the theory we are considering is the pure QED, so the diagram (1) cannot contribute.

However, we can still carry out the analysis of this process for the following reasons:

- at least in principle we could still see effects of photon self-interaction caused by lattice artifacts or from the low space dimensionality of the system;
- even if the photons are non-interacting, this analysis could be a training exercise for more complex scattering processes.

The content of the chapters is the following:

- in **chapter 1**, we provide comprehensive overview of Lattice Gauge Theories, introducing also the concept of Quantum Link Model formulation;
- in **chapter 2**, we focus on the specific two-leg ladder system within the context of Hamiltonian Lattice Quantum Electrodynamics and discuss its key properties that make it suitable for studying single-particle wave-packet states;
- in **chapter 3**, we give details about the algorithm to construct generic one-dimensional single-particle wave-packet states; in particular, we explore the use of exact diagonalization and localization of Wannier functions, among other techniques, to create these states;

- in **chapter 4**, we delve into the fundamentals of Tensor Network (TN) methods, explaining their mathematical and computational aspects and how they are utilized in simulating quantum many-body systems;
- in **chapter 5**, we present the method to traduce the wave-packet states of chapter 3 into an MPS structure, and we perform simulations using the proposed algorithm to create initial states and TN methods for time evolution, discussing the results and the insights gained;
- in the **final chapter**, we present the conclusions drawn from our study and we discuss potential future directions, applications and generalization of the proposed method, addressing novel TN techniques and exploring scattering processes of more complex LGTs.

Chapter 1

Theoretical Background

In this chapter a brief derivation of the Kogut-Susskind [27, 28] Lattice QED Hamiltonian without fermions in a $(2+1)$ -dimensional spacetime is provided. Far from giving a detailed formal framework of Lattice Gauge Theory [5], which is not the aim of this thesis, the goal of this section is to give an heuristic but self-consistent description of the theoretical background needed to treat the model of the following chapters.

We first set some definitions and notations about classical (pure) electrodynamics and its counterpart in $2+1$ spacetime dimensions. We define the concept of Wilson loop [7] and we derive the discretized Hamiltonian directly from the continuous one, discussing the canonically quantized counterpart of the lattice theory. Finally, we present the *Quantum Link Model* formulation [29] of the system, which will be applied to the ladder geometry of the next chapter.

1.1 Classical and quantum electrodynamics in vacuum

In the following sections, we will use the notation and conventions of [2], using the Heaviside–Lorentz c.g.s. natural units system, setting $c = \hbar = 1$.

1.1.1 Electrodynamics in $(3+1)$ dimensions

We consider a $(3+1)$ -dimensional space-time with metric tensor signature such that $\eta^{\mu\nu} = \eta_{\mu\nu} = \text{diag}(1, -1, -1, -1)$.

The Lagrangian density of the electrodynamics in $(3+1)$ dimensions in vacuum (without matter) reads

$$\mathcal{L}(x) = -\frac{1}{4} F_{\mu\nu} F^{\mu\nu} = \frac{1}{2} \mathbf{E}^2 - \frac{1}{2} \mathbf{B}^2, \quad (1.1)$$

where $F^{\mu\nu}$ is the electromagnetic field strength tensor, defined in terms of the electromagnetic gauge field A_μ as

$$F^{\mu\nu} = \partial^\mu A^\nu - \partial^\nu A^\mu = \begin{pmatrix} 0 & -E_x & -E_y & -E_z \\ E_x & 0 & -B_z & B_y \\ E_y & B_z & 0 & -B_x \\ E_z & -B_y & B_x & 0 \end{pmatrix}. \quad (1.2)$$

The equations of motion derived from the Lagrangian (1.1) are the covariant Maxwell equations in vacuum

$$\epsilon^{\mu\nu\rho\sigma} \partial_\nu F^{\rho\sigma} = 0, \quad \partial_\mu F^{\mu\nu} = 0. \quad (1.3)$$

which can be written explicitly with respect the electric and magnetic field as

$$\left\{ \begin{array}{ll} \nabla \cdot \mathbf{E} = 0 & \text{Gauss' Law (for } E); \\ \nabla \cdot \mathbf{B} = 0 & \text{Gauss' Law (for } B); \\ \nabla \times \mathbf{E} = -\dot{\mathbf{B}} & \text{Faraday's Law;} \\ \nabla \times \mathbf{B} = \dot{\mathbf{E}} & \text{Ampère's Law.} \end{array} \right. \quad (1.4)$$

The Maxwell's equations (1.3) are invariant under local gauge transformations

$$A'_\mu = A_\mu + \partial_\mu \chi. \quad (1.5)$$

where $\chi(x)$ is an arbitrary smooth function of the spacetime.

The conjugate momenta of the gauge fields are

$$\Pi_0 = \frac{\delta \mathcal{L}}{\delta(\partial_0 A^0)} = 0, \quad \Pi_i = \frac{\delta \mathcal{L}}{\delta(\partial_0 A^i)} = -E_i. \quad (1.6)$$

Since, in the next section, we will break Lorentz invariance symmetry in the lattice, we can use a non-Lorentz invariant gauge such as the temporal gauge

$$\phi = A^0 = 0. \quad (1.7)$$

In this gauge, from the definition of vector potential, we simply have

$$E^i = -\partial_0 A^i, \quad (1.8)$$

so as dynamical degrees of freedom of our system we can just consider the spatial components of the fields A^i and E^i , because the temporal ones are vanishing. The Hamiltonian density can be obtained via Legendre transformation. In particular, using the temporal gauge:

$$\mathcal{H} = \Pi_0 \partial_0 A^0 + \Pi_i \partial_0 A^i - \mathcal{L} = \frac{1}{2} E^2 + \frac{1}{2} B^2. \quad (1.9)$$

Integrating (1.9) with respect the space (with time fixed) we obtain the energy, i.e. the Hamiltonian of the system at time t :

$$H = \int d^3x \mathcal{H} = \frac{1}{2} \int d^3x (E^2 + B^2) = H_E + H_B, \quad (1.10)$$

where we defined the electric and magnetic terms of the Hamiltonian as as

$$H_E \equiv \frac{1}{2} \int d^3x E^2(x), \quad H_B \equiv \frac{1}{2} \int d^3x B^2(x). \quad (1.11)$$

1.1.2 Electrodynamics in (2+1) dimensions

The electrodynamics in (2+1) dimensions is a simplified version of the electromagnetic theory in which spacetime is assumed to have two spatial dimensions and one temporal dimension.

Overall, $(2+1)$ -dimensional electrodynamics provides a fascinating arena to explore the behavior of electromagnetic fields and their interactions in a reduced dimensional space, leading to unique physical properties and theoretical insights [49, 50]. In particular, this simplification allows also for computationally tractable results. In this thesis, this reduction is useful to derive in a simple way the discretized version of the Hamiltonian (1.10), done in section 1.2.2.

In $(2+1)$ dimensions, the gauge field A_μ is a three-component vector field, where the index $\mu = 0, 1, 2$ represents the temporal and spatial components, as the three-dimensional case. The field strength tensor $F_{\mu\nu}$, analogous to the familiar electric and magnetic fields in $(3+1)$ dimensions, is defined as usual as the antisymmetric derivative of A_μ with respect to spacetime coordinates:

$$F_{\mu\nu} = \partial_\mu A_\nu - \partial_\nu A_\mu = \begin{pmatrix} 0 & -E_x & -E_y \\ E_x & 0 & -B \\ E_y & B & 0 \end{pmatrix}, \quad B \equiv B_z. \quad (1.12)$$

This is one of the possible *dimensional reductions* [51] of the electrodynamics: the only non-vanishing components of the fields are the longitudinal directions of E and the transversal one of B :

$$E_z = B_x = B_y = 0, \quad B_z = B, \quad \partial_z = 0. \quad (1.13)$$

Defining the perpendicular gradients

$$\nabla = \begin{pmatrix} \partial_1 \\ \partial_2 \end{pmatrix}, \quad \nabla_\perp = \begin{pmatrix} -\partial_2 \\ \partial_1 \end{pmatrix}, \quad (1.14)$$

where the operator “ $\nabla_\perp \cdot$ ” is the analogue of the curl “ $\nabla \times$ ” in $(2+1)$ -dimensions, it is straightforward to show that the Maxwell equations in $(2+1)$ dimensions reduce to

$$\begin{cases} \nabla \cdot \mathbf{E} = 0 & \text{Gauss' Law} \\ \nabla_\perp \cdot \mathbf{E} = -\dot{B} & \text{Faraday's Law} \\ \nabla_\perp \cdot \mathbf{B} = -\dot{\mathbf{E}} & \text{Ampère's Law} \end{cases} \quad (1.15)$$

Notice that the Gauss' Law for the magnetic field is identically satisfied in $2+1$ dimensions.

Since the definition of the Lagrangian and conjugate momenta are the same of the $(3+1)$ -dimensional case, in the temporal gauge (1.7) the Hamiltonian of the system takes the same form, with an integral in a plane instead of an integral in the three-dimensional space:

$$H = H_E + H_B = \int d^2x \mathcal{H} = \frac{1}{2} \int d^2x (E^2 + B^2). \quad (1.16)$$

1.1.3 Canonical quantization of the gauge fields

The canonical quantization of the gauge fields in quantum electrodynamics (QED) is a fundamental approach used to describe the quantum behavior of the quantum counterpart of the electromagnetic field and interactions [2]. This formalism provides a framework for calculating scattering amplitudes and understanding the underlying quantum nature of electromagnetism in QED.

The canonical quantization procedure treats the electromagnetic field as an (infinite) collection of harmonic oscillators. By imposing canonical commutation relations, the field is promoted to a quantum operator, allowing for the quantization of the electromagnetic field:

$$A_i \rightarrow \hat{A}_i, \quad \Pi_i \rightarrow \hat{\Pi}_i = -\hat{E}_i, \quad (1.17)$$

The set of *equal-time canonical commutation relations* between the gauge field and its conjugated momenta reads (in two spatial dimensions)

$$[\hat{A}_i(t, \mathbf{x}), \hat{\Pi}_j(t, \mathbf{y})] = i\delta^{(2)}(\mathbf{x} - \mathbf{y}) \delta_{ij}, \quad (1.18)$$

and since we identified Π_i as the opposite of the electric field in (1.6) we obtain

$$[\hat{A}_i(t, \mathbf{x}), \hat{E}_j(t, \mathbf{y})] = -i\delta^{(2)}(\mathbf{x} - \mathbf{y}) \delta_{ij}. \quad (1.19)$$

In the context of this theory, the quantization of the degrees of freedom of the field A^μ leads to the existence of quanta of particles associated with the electromagnetic field, called *photons* [2].

1.2 The (2+1)-dimensional Lattice QED

The regularization on a lattice is a technique used in Lattice Gauge Theory to overcome the difficulties associated with the non-perturbative nature of Quantum Field Theories. It involves discretizing spacetime into a lattice of finite spacing a . The continuum field theory is then approximated by a lattice field theory with a finite number of lattice sites. This discretization provides a well-defined framework for performing calculations and allows for numerical simulations on a computer. By introducing a lattice spacing, the ultraviolet divergences, which arise from infinitely short-distance fluctuations, are naturally regulated. The lattice spacing acts as an ultraviolet cutoff, limiting the momenta that can be exchanged between particles.

The regularization on a lattice preserves some important symmetries of the continuum theory and allows for the study of non-perturbative phenomena such as confinement and chiral symmetry breaking in gauge theories. However, in Lattice Gauge Theory, *Lorentz symmetry* is typically broken at the microscopic level due to the introduction of a finite lattice spacing. This breaking manifests as lattice artifacts, which are deviations from exact Lorentz invariant theory, which should become insignificant in the *continuum limit*, as the lattice spacing approaches to zero.

In the section 1.1 it was shown that the Hamiltonian of the Electrodynamics in the continuum space can be written as a sum of the electric and magnetic terms

$$H_E = \frac{1}{2} \int d^2x E^2(x), \quad H_B = \frac{1}{2} \int d^2x B^2(x). \quad (1.20)$$

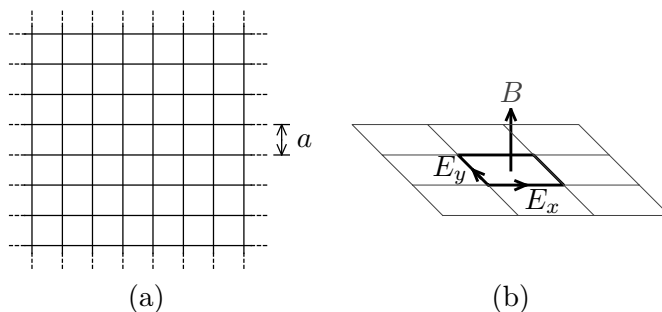


Figure 1.1. (a) A square lattice of lattice spacing a . (b) In the context of pure lattice QED, the components E_x, E_y of the electric field are living in the links of the lattice. The magnetic field $B = B_z$ is instead perpendicular to the plane, and it is associated to the plaquettes.

In this section, a discretization of the two-dimensional space is performed, using a square lattice of spacing a (Fig. 1.1a).

In order to determine the Hamiltonian after the discretization, we want to identify the new field variables associated to this model. We perform the discretization of the fields identifying the electric field components E_x, E_y on the links, and the transversal magnetic field component $B_z = B$ on the plaquettes (fig. 1.1b).

1.2.1 Wilson loops

A Wilson loop [7] is a mathematical object used to study the behavior of gauge fields. Mathematically, it is the integral of a gauge field along a closed loop in spacetime [2]. It characterizes how a quantum field interacts with the gauge field as it propagates along the loop. The loop can be any closed curve γ : the Wilson loop computes the phase acquired by the quantum field as it travels along γ .

Wilson loops are crucial in lattice gauge theories because they serve as order parameters for the confinement-deconfinement phase transition, providing insights into the behavior of quarks and gluons at different energy scales.

In the context of quantum electrodynamics in (2 + 1)-dimension, given a path γ from x to y in spacetime, we define the *Wilson line*, also known as *comparator* [2], the quantity

$$U_\gamma(x, y) \equiv \exp\left(ie \int_x^y dx_\mu A^\mu(x)\right), \quad (1.21)$$

where e is the fundamental charge. The quantity (1.21) becomes independent from A^0 in the temporal gauge $A^0 = 0$:

$$U_\gamma(\mathbf{x}, \mathbf{y}) = \exp\left(-ie \int_x^y dx_i A^i(x)\right), \quad (1.22)$$

where the minus sign comes from the contraction with the metric.

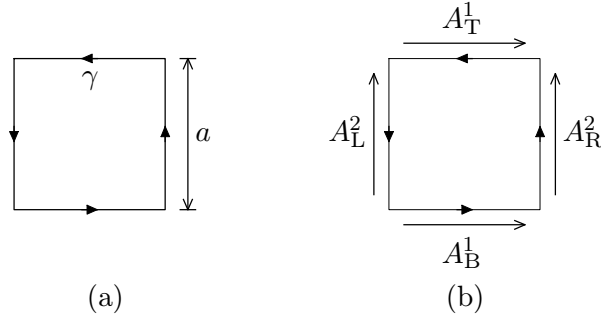


Figure 1.2. (a) A plaquette of side a counterclockwise oriented. (b) Notation used for the direction and labelling of the gauge field A^i on the sides of the plaquette.

The comparator is also known as the *parallel transporter*, and its role becomes clearer in the context of Lattice QED where gauge fields are coupled with matter. Indeed, the comparator is the quantity needed to compensate for the phase difference between the two points in the definition of the covariant derivative. However, the treatment of the geometry of the gauge fields is not the aim of this thesis, and the definition (1.21) is enough to accomplish all the following derivations.

If the path γ is closed, the parallel transporter is called the *Wilson loop* around the path

$$U_\gamma = \exp\left(-ie \oint_\gamma dx_i A^i(x)\right). \quad (1.23)$$

which is a gauge-invariant quantity. If the path is a straight infinitesimal line γ from \mathbf{x} to $\mathbf{x} + \boldsymbol{\epsilon}$, where $\boldsymbol{\epsilon}$ is a vector with infinitesimal norm ($\|\boldsymbol{\epsilon}\| \ll 1$), we can expand the comparator as

$$U_\boldsymbol{\epsilon} \simeq e^{-ie\boldsymbol{\epsilon} \cdot \mathbf{A}}. \quad (1.24)$$

Let's now consider an infinitesimal square plaquette \square with infinitesimal side length a , and we set γ as the counter-clockwise path along the border of the plaquette (fig. 1.2a) The Wilson loop, in this case known as plaquette term, can be decomposed into four infinitesimal Wilson lines of the form (1.24):

$$U_\square \equiv e^{-ieaA_B} e^{-ieaA_R} e^{+ieaA_T} e^{+ieaA_L} = U_B U_R U_T^\dagger U_L^\dagger, \quad (1.25)$$

where the signs of the exponents are consistent with the orientation of the loops with respect the positive direction of the axes (fig. 1.2b).

Regarding computing the value of (1.25) around a closed square plaquette, we can evaluate the following closed integral using the *Stoke's theorem*:

$$\oint_{\partial\square} dx_i A^i = \int_\square dx^1 dx^2 (\partial_1 A^2 - \partial_2 A^1) = \int_\square dx^1 dx^2 B(x). \quad (1.26)$$

Now, let be $x_c \equiv (x_c^1, x_c^2)$ the center of the plaquette \square . We can expand $B(x^1, x^2)$ in Taylor series around the plaquette center as

$$B(x) = B_0 + \sum_{i=1}^2 \frac{\partial B(x_c)}{\partial x^i} x^i + \sum_{i,j=1}^2 \frac{\partial^2 B(x_c)}{\partial x^i \partial x^j} x^i x^j + \mathcal{O}(x^3). \quad (1.27)$$

where we defined $B_0 \equiv B(x_c) = B(x_c^1, x_c^2)$ the field in the center of the plaquette. Now, inserting (1.27) inside (1.26) the first-order terms of the expansion cancels after integration, and we obtain

$$\oint_{\partial \square} dx_i A^i = a^2 B_0 + \mathcal{O}(a^4). \quad (1.28)$$

Hence, the phase accumulated around the plaquette is proportional to the flux of the magnetic field over that plaquette. In particular, we showed that we can express the Wilson loop (1.24) as a function of B up to corrections of fourth order in a .

Furthermore, we also notice that we can expand the real quantity

$$U_{\square} + U_{\square}^{\dagger} = e^{-ie \oint_{\partial \square} dx_i A^i} + e^{+ie \oint_{\partial \square} dx_i A^i} = 2 \cos \left(e \oint_{\partial \square} dx_i A^i \right) \quad (1.29)$$

up to sixth order in the lattice spacing a , using (1.28) and (1.29):

$$\begin{aligned} U_{\square} + U_{\square}^{\dagger} &= 2 \cos(e(a^2 B_0 + \mathcal{O}(a^4))) \\ &= 2 - 2 \cdot \frac{1}{2!} e(a^2 B_0 + \mathcal{O}(a^4))^2 + \mathcal{O}(a^8), \end{aligned}$$

from which we obtain

$$U_{\square} + U_{\square}^{\dagger} = 2 - e^2 a^4 B_0^2 + \mathcal{O}(a^6). \quad (1.30)$$

1.2.2 The Kogut-Susskind Hamiltonian

In this section, we derive the lattice version of the pure (2 + 1)-dimensional QED Hamiltonian.

First, from equations (1.21), (1.19) and $\mathbf{B} = \nabla \times \mathbf{A}$ it respectively follow the dimensions of the fields:

$$[A^i] = \frac{1}{[e][a]}, \quad [E^i] = \frac{[e]}{[a]}, \quad [B^i] = \frac{1}{[e][a]^2}. \quad (1.31)$$

We will use a square lattice in a plane, in absence of matter, mapping the continuum fields to the *dimensionless discretized fields* as follows

$$A^i \rightarrow \frac{1}{ea} A_l, \quad E^i \rightarrow \frac{e}{a} E_l, \quad B \rightarrow \frac{1}{ea^2} B_{\square}, \quad \int d^2x \dots \rightarrow \sum a^2 \dots \quad (1.32)$$

where l represents a link and \square a plaquette. Hence, the electric and magnetic Hamiltonians in the lattice can be written from (1.16) as

$$H_E = \frac{e^2}{2} \sum_l E_l^2, \quad H_B = \frac{1}{2e^2 a^2} \sum_{\square} B_{\square}^2. \quad (1.33)$$

However, we want to express the magnetic term as a function of the link variables. Using the dimensionless fields (1.32), the equation (1.30) becomes, omitting the order expansion in a :

$$B_{\square}^2 = 2 - (U_{\square} + U_{\square}^{\dagger}). \quad (1.34)$$

In this way, we can express the magnetic field as a function of the plaquette operators. Now we can express the magnetic Hamiltonian term in function of U, U^{\dagger} , inserting (1.34) inside (1.33):

$$H_B = \frac{1}{2e^2 a^2} \sum_{\square} B_{\square}^2 = \frac{N_{\square}}{e^2 a^2} - \frac{1}{2e^2 a^2} \sum_{\square} (U_{\square} + U_{\square}^{\dagger}), \quad (1.35)$$

where N_{\square} is the number of plaquettes of the system, which is divergent in the *thermodynamic limit*. For a system with finite size, i.e. finite number of plaquettes, the first term in the last member of (1.35) is a constant shift of the Hamiltonian, so it does not affect the dynamics and it can be neglected. Thus, the magnetic term of the discretized Hamiltonian reads

$$H_B = -\frac{1}{2e^2 a^2} \sum_{\square} (U_{\square} + \text{H.c.}). \quad (1.36)$$

We know that the plaquette operator is a Wilson loop which can be expressed as the product of Wilson lines around the plaquette:

$$U_{\square} = U_B U_L U_T^{\dagger} U_R^{\dagger} = e^{iA_B} e^{iA_L} e^{-iA_T} e^{-iA_R}, \quad (1.37)$$

Thus, H_B has been written as a function of the gauge field, which lives in the links of the lattice.

Finally, defining the *relative electric field strength coupling* as

$$g^2 = e^2 a, \quad (1.38)$$

we obtain the discrete form of the lattice QED *Kogut-Susskind Hamiltonian* without fermions

$$H = H_E + H_B = \frac{g^2}{2a} \sum_l E_l^2 - \frac{1}{2ag^2} \sum_{\square} (U_{\square} + \text{H.c.}). \quad (1.39)$$

Notice that the ratio between the electric field strength and the magnetic field strength is

$$\frac{g_E}{g_B} = \frac{\frac{g^2}{2a}}{\frac{1}{2ag^2}} = g^4. \quad (1.40)$$

Hence, g^4 is actually the natural perturbation parameter of this system.

1.2.3 Quantization of the lattice link variables

In order to quantize the system in the lattice, we have to consider the counterpart of the canonical commutation relation (1.19) of the dimensionless field operators

$$A_l \rightarrow \hat{A}_l, \quad E_l \rightarrow \hat{E}_l. \quad (1.41)$$

From the following dimensionless substitution of the δ function:

$$\delta^{(2)}(\mathbf{x} - \mathbf{y}) \delta_{ij} \rightarrow \frac{1}{a^2} \delta_{ll'}, \quad (1.42)$$

the commutation relations (1.19) becomes in the lattice

$$[\hat{A}_l, \hat{E}_{l'}] = -i\delta_{ll'}, \quad (1.43)$$

where \hat{E}_l, \hat{A}_l are the electric field and the vector potential operators defined for the lattice link l . In this context, the parallel transporter operator can be defined in an infinitesimal path i.e. a link l of the lattice, as

$$\hat{U}_l \equiv e^{-i\hat{A}_l}. \quad (1.44)$$

Applying the *Baker-Campbell-Hausdorff formula* we obtain:

$$\begin{aligned} \hat{U}^\dagger \hat{E} \hat{U} &= e^{i\hat{A}} \hat{E} e^{-i\hat{A}} \\ &= \hat{E} + i[\hat{A}, \hat{E}] + \frac{i^2}{2!} [\hat{A}, [\hat{A}, \hat{E}]] + \frac{i^3}{3!} [\hat{A}, [\hat{A}, [\hat{A}, \hat{E}]]] + \dots \\ &= \hat{E} + i[\hat{A}, \hat{E}] + 0 + 0 + \dots \\ &= \hat{E} - i^2 \mathbb{I} \\ &= \hat{E} + \mathbb{I}, \end{aligned}$$

From which we immediately obtain the following commutation algebra

$$[\hat{E}, \hat{U}] = \hat{U}, \quad [\hat{E}, \hat{U}^\dagger] = -\hat{U}^\dagger, \quad [\hat{U}, \hat{U}^\dagger] = 0. \quad (1.45)$$

The relations (1.45) encodes a ladder operator algebra. Indeed, if $|E\rangle$ is an eigenstate of the electric field operator with eigenvalue E

$$\hat{E}|E\rangle = E|E\rangle, \quad (1.46)$$

then the action of \hat{U} and \hat{U}^\dagger is that of increasing and decreasing the value of the electric field of a link:

$$\hat{U}|E\rangle = |E+1\rangle, \quad \hat{U}^\dagger|E\rangle = |E-1\rangle. \quad (1.47)$$

1.2.4 Gauge invariance: the Gauss' Law

We want to impose that physical states $|\Phi\rangle$ are invariant under gauge transformations. In general a gauge transformation operator has the form

$$\hat{Y} = \exp\left(-i \int d^3x \alpha(\mathbf{x}) \hat{G}(\mathbf{x})\right), \quad (1.48)$$

where $\alpha(\mathbf{x})$ is a continuous function representing the gauge freedom, and $G(\mathbf{x})$ is the local generator of the gauge transformation. If a physical state is invariant under gauge transformation then it is invariant under the action of a gauge operator:

$$\hat{Y}|\Phi\rangle = |\Phi\rangle. \quad (1.49)$$

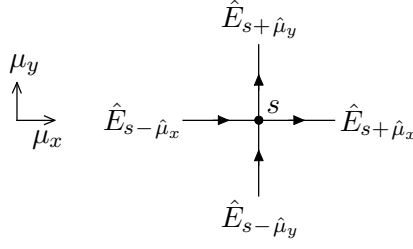


Figure 1.3. Notation for the Gauss' Law in the lattice: a site s has four neighboring sites $s \pm \hat{\mu}_i$, and the associated links with electric field operators $\hat{E}_{s \pm \hat{\mu}_i}$.

A sufficient condition to satisfy (1.49) is

$$\hat{G}(x)|\Phi\rangle = 0 \quad \forall x. \quad (1.50)$$

It can be proved that the generator of the gauge transformation is

$$\hat{G}(x) = \nabla \cdot \hat{\mathbf{E}}, \quad (1.51)$$

so that the gauge invariant states $|\Phi\rangle$ are encoded in the following condition, which is the quantum implementation of the Gauss' Law:

$$\nabla \cdot \hat{\mathbf{E}}|\Phi\rangle = 0. \quad (1.52)$$

In the lattice, it is simple to write the discretized version of the gauge generator \hat{G}_l in a lattice site, in the basis which diagonalize the electric field operators. Indeed, if

$$\hat{G}(\mathbf{x}) = \partial_x \hat{E}_x(\mathbf{x}) + \partial_y \hat{E}_y(\mathbf{x}), \quad (1.53)$$

in a lattice site s , the discretized version of (1.53) is

$$\hat{G}_s = (\hat{E}_{s+\hat{\mu}_x} - \hat{E}_{s-\hat{\mu}_x}) + (\hat{E}_{s+\hat{\mu}_y} - \hat{E}_{s-\hat{\mu}_y}), \quad (1.54)$$

where we denote with $\hat{\mu}_{x,y}$ the lattice versors, so that $s \pm \hat{\mu}_i$ are the neighboring sites of s (Fig. 1.3).

The Gauss' Law has a simple interpretation on the lattice: in the electric field basis, for each lattice site, the sum of all the ingoing electric field from the links must be equal to the sum of all the outgoing electric field from the site.

One can show that, for every site s , the Hamiltonian of the lattice commutes with the generator of the gauge transformations:

$$[\hat{G}_s, \hat{H}] = 0, \quad \forall s. \quad (1.55)$$

Hence, if a state $|\Phi\rangle$ obeys the Gauss' Law, i.e. if the state belongs to the *gauge invariant subspace* of physical states

$$\mathcal{H}_{\text{Phys}} \equiv \{|\Phi\rangle \mid \hat{G}_s|\Phi\rangle = 0 \quad \forall s\}, \quad (1.56)$$

at $t=0$, then the evolved state $|\Phi(t)\rangle = e^{-i\hat{H}t}|\Phi\rangle$ remains inside that physical subspace for all $t > 0$ (Fig. 1.4).

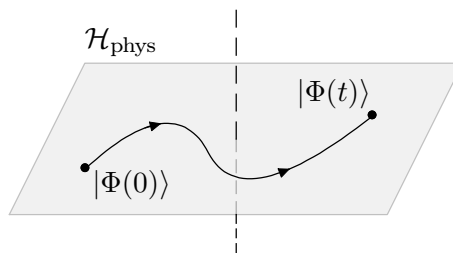


Figure 1.4. An initial state $|\Phi(0)\rangle$ belonging to the physical gauge-invariant subspace $\mathcal{H}_{\text{phys}}$ remains inside it under time evolution.

1.3 The Quantum Link Model

The spectrum of the electromagnetic operator \hat{E}_l is, at least in principle, unbounded. This means that the value of the electromagnetic field for each link can be arbitrarily high, and the local Hilbert space of a link of the lattice is infinite dimensional. This is a problem if the aim of the Lattice formulation is that of numerically simulating the system: indeed, an infinite number of basis elements is numerically intractable. Thus, we need a cutoff procedure which allows to bound the value of the electric field, preserving the algebra (1.45) but considering a finite number of electric field configurations. One possible solution is the *Quantum Link Model* (QLM) formulation [29] of Lattice Gauge Theory.

1.3.1 Mapping link operators to spin operators

The intuition behind the QLM is the observation that the algebra (1.45) is similar to the $SU(2)$ spin operator algebra

$$[\hat{S}^z, \hat{S}^+] = \hat{S}^+, \quad [\hat{S}^z, \hat{S}^-] = -\hat{S}^-, \quad [\hat{S}^+, \hat{S}^-] = 2\hat{S}^z, \quad (1.57)$$

where \hat{S}^\pm are the spin ladder operators defined as

$$\hat{S}^+ = \hat{S}^x + i\hat{S}^y, \quad \hat{S}^- = \hat{S}^x - i\hat{S}^y. \quad (1.58)$$

This brings to the following identification between link variables of the lattice and spin variables:

$$\hat{E} \rightarrow \hat{S}^z, \quad \hat{U} \rightarrow \hat{S}^+, \quad \hat{U}^\dagger \rightarrow \hat{S}^-. \quad (1.59)$$

The main problem of the QLM formulation is that the operators \hat{S}^\pm are no more unitary, namely the algebra is not preserved for the last equality of (1.45) and (1.57):

$$[\hat{U}, \hat{U}^\dagger] = 0, \quad [\hat{S}^+, \hat{S}^-] \neq 0. \quad (1.60)$$

A possible solution to the problem of unitarity is to identify the plaquette operators as

$$\hat{U} \rightarrow \frac{\hat{S}^+}{s}, \quad \hat{U}^\dagger \rightarrow \frac{\hat{S}^-}{s}, \quad (1.61)$$

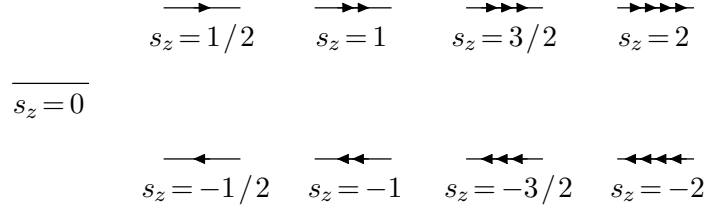


Figure 1.5. Notation for the z -projection of the spin operators in the lattice links of the Quantum Link Model.

where $s \in \mathbb{N}/2$ is the spin representation, whose $s = 1/2$ is the lowest one. Also with this identification, the first two equalities of (1.45) are preserved, while for the third one, at least in the limit of large spin representation $s \rightarrow \infty$, which is the limit we want to reach to obtain the real QED, we recover unitarity of the operators:

$$[\hat{U}, \hat{U}^\dagger] \rightarrow \frac{1}{s^2} [\hat{S}^+, \hat{S}^-] = \frac{2\hat{S}^z}{s^2} \xrightarrow{s \rightarrow \infty} 0. \quad (1.62)$$

The recovery of the unitarity of \hat{S}^\pm in the large s limit can be seen more explicitly applying the operator $\hat{U}^\dagger \hat{U}$ to a generic eigenstate $|s, s_z\rangle$ of \hat{S}^z . In particular, the operator $\hat{U}^\dagger \hat{U}$ becomes the identity for $s \rightarrow \infty$:

$$\begin{aligned} \lim_{s \rightarrow \infty} \hat{U}^\dagger \hat{U} |s, s_z\rangle &= \lim_{s \rightarrow \infty} \frac{1}{s^2} \hat{S}^- \hat{S}^+ |s, s_z\rangle \\ &= \lim_{s \rightarrow \infty} \frac{\sqrt{s(s+1) - (s_z+1)s_z} \sqrt{s(s+1) - s_z(s_z+1)}}{s} |s, s_z\rangle \\ &= 1 \cdot 1 \cdot |s, s_z\rangle \\ &= \mathbb{I} |s, s_z\rangle, \end{aligned} \quad (1.63)$$

and the same holds for $\hat{U} \hat{U}^\dagger$, hence for $s \rightarrow \infty$ the unitarity is recovered.

In the QLM formulation, the Kogut-Susskind Hamiltonian takes the form

$$\hat{H}_{\text{QLM}} = \frac{g^2}{2a} \sum_l (\hat{S}_l^z)^2 - \frac{1}{2ag^2} \sum_{\square} (\hat{S}_B^+ \hat{S}_L^+ \hat{S}_T^- \hat{S}_R^- + \text{H.c.}), \quad (1.64)$$

where $\hat{S}_B^+ \hat{S}_L^+ \hat{S}_T^- \hat{S}_R^-$ is the plaquette operator written in terms of spin variables.

1.3.2 QLM spin notation and the Gauss' Law

In the Quantum Link Model, the electric field operators of the links are identified with the \hat{S}^z spin operators. This means that the basis that diagonalizes the electric field is represented by the spin basis of the z -projection of the spin. We know that chosen a spin representation $s \in \mathbb{N}/2$ the spectrum of \hat{S}^z ranges between the $2s + 1$ integer (or semi-integer) values

$$s^z \in \{-s, -s+1, \dots, s-1, s\}. \quad (1.65)$$

To represent the lattice spin configurations of the links we can use the following notation for the z -projection of the spin (Fig. 1.5).

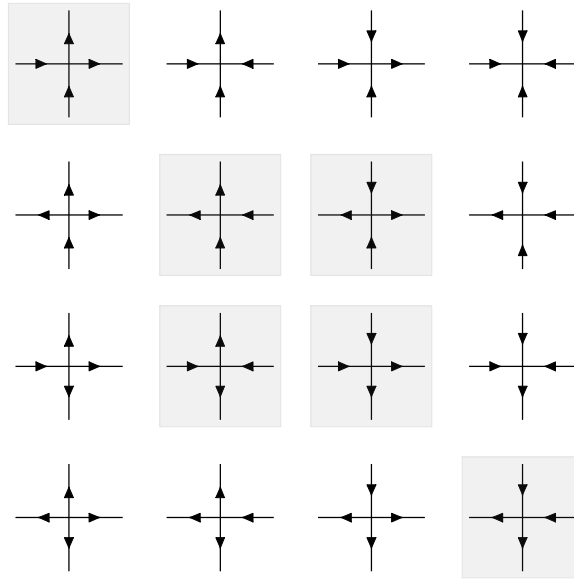


Figure 1.6. Using the spin representation $s = 1/2$, for a lattice site with four neighboring links, there are 16 total configurations. Only 6 (highlighted in this figure) are compatible with the Gauss' Law.

Thus, we can implement the Gauss' Law for each site and the neighboring links of the lattice, selecting all the allowed local configurations. For instance, for the specific case of $s = 1/2$, figure 1.6 shows the 6 gauge invariant local configurations out of the 16 possible local configurations of the electric field in a single site.

Chapter 2

Pure Lattice QED on ladder geometries

2.1 The ladder geometry

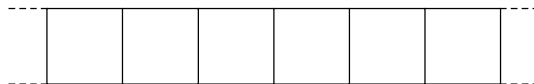
The Kogut-Susskind formulation allows, at least in principle, to perform a numerical simulation of any gauge theory in arbitrary spacetime dimension D [27]. However, we have to balance between these two disadvantages:

- the more the space dimensionality D increases, the more computational cost is needed to handle the increasingly large Hilbert space of the theory;
- conversely, the more the space dimensionality D decreases, the more the theory becomes trivial and distant from reality.

For the QED case, the $(1+1)$ - D theory is trivial, widely studied and exactly solvable even in the continuum spacetime [52] (also known as the *Schwinger Model*). Furthermore, in the $(1+1)$ -dimensional QED photons cannot propagate due to the absence of a transverse polarization component of the electric field, and the absence of the magnetic field. This fact makes impossible many phenomenological aspects of QED such as the scattering where photons are involved.

Concerning $(2+1)$ - D and $(3+1)$ - D QED, these theories become computationally intractable very quickly as the plaquette number increases.

A nice compromise as a lattice theory is to consider a “ $1+\epsilon$ ” dimensional system, which has a two-leg ladder geometry in the lattice:



We construct a “chain” of plaquettes, so that the system remains quasi-1-dimensional, but it acquires a width extension so that the magnetic field plaquette term allows photon propagation. The continuum counterpart of the ladder model could represent a matter of

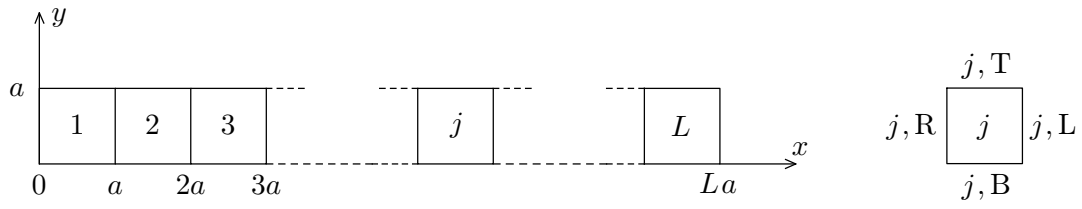
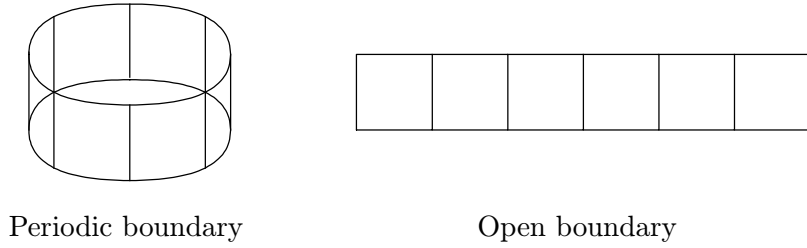


Figure 2.1. Enumeration convention of the plaquettes in the one-leg ladder system. We denote with $j = 1, \dots, L$ the plaquette number, and with B,R,T,L (which stems for Bottom, Right, Top and Left), the link associated to the plaquette.



Periodic boundary

Open boundary

Figure 2.2. The two boundary conditions applied to the two-leg ladder system.

study in the context of dimensional reduction of QED [51].

| Spacetime dimension | $(1+1)-D$ | $(\text{"}1+\epsilon\text{"}+1)-D$ | $(1+2)-D$ |
|---------------------|---------------------------------------|------------------------------------|--------------------------|
| Continuous models | | | |
| | QED ₂ (Schwinger model) | (?) | QED ₃ |
| Lattice models | | | |
| | Lattice QED ₂ | "Ladder QED" | Lattice QED ₃ |

Table 2.1. Classification of QED theories up to two spatial dimensions, using a naïve spatial representation.

Hence, the lattice geometry we are going to consider and study is the so-called two-leg ladder composed of L plaquettes. There are two topologies associated to the ladder, which sets the boundaries as open or periodic (Fig. 2.2). The latter closes the final plaquette $j = L$ with the starting plaquette $j = 1$. From now on in this chapter, unless specified otherwise,

periodic boundary conditions are used by default.

2.2 The Quantum Link Model on the Ladder

The number of links N_l of the lattice can be simply counted in open boundary and periodic boundary conditions as follows:

$$N_l^{\text{open}} = 3L + 1, \quad N_l^{\text{periodic}} = 3L. \quad (2.1)$$

We choose a spin representation $s \in \mathbb{N}/2$, so that for each link l we can represent the electric field operator \hat{E} as the spin operator \hat{S}^z . Thus, the local Hilbert space $\mathcal{H}_l^{(s)}$ for each single link has dimension $2s + 1$,

$$\mathcal{H}_l^{(s)} = \mathbb{C}^{2s+1}, \quad \dim \mathcal{H}_l^{(s)} = 2s + 1, \quad (2.2)$$

and the global Hilbert space of the whole quantum system can be obtained as a tensor product of all the local Hilbert spaces (2.2) of all the links:

$$\mathcal{H}_{\text{tot}}^{(s)} = \bigotimes_{l=1}^{N_l} \mathcal{H}_l^{(s)}, \quad \dim \mathcal{H}_{\text{tot}}^{(s)} = (2s + 1)^{N_l}. \quad (2.3)$$

In order to construct a computational basis $\{|\Psi\rangle\}$ of $\mathcal{H}_{\text{tot}}^{(s)}$ we have to find the basis $\{|\phi\rangle_l\}$ of the local Hilbert space $\mathcal{H}_l^{(s)}$. We can use the local spin- z basis $\{|s, s_z\rangle\}$ whose elements are defined as

$$|\phi\rangle_l \equiv |s, s_z\rangle \equiv \underbrace{(0, 0, \dots, 0, 1, 0, \dots, 0)}_{2s+1 \text{ entries}}^\top, \quad (1 \text{ at position } s_z + s + 1). \quad (2.4)$$

In this way, the basis $\{|\Phi\rangle_i\}$ of $\mathcal{H}_{\text{tot}}^{(s)}$ total Hilbert space is obtained as the tensor product of all the possible combinations of local basis (2.4):

$$|\Phi\rangle = \bigotimes_{l=1}^{N_l} |\phi\rangle_l. \quad (2.5)$$

Thus, a generic quantum state of the ladder can be represented choosing a set $\{\alpha_i \in \mathbb{C}\}$ of complex numbers such that

$$|\Psi\rangle = \sum_{i=1}^{\dim \mathcal{H}_{\text{tot}}^{(s)}} \alpha_i |\Phi\rangle_i, \quad \langle \Psi | \Psi \rangle = 1. \quad (2.6)$$

However, the Hilbert space (2.3) is not the space of physical states. A physical state, as discussed in the section (1.2.4) is a gauge invariant state, i.e. a state which is invariant

under gauge transformations. We showed that the condition for a state $|\Psi_G\rangle$ to be gauge invariant is

$$\hat{G}_j|\Psi_G\rangle = 0 \quad \forall j, \quad (2.7)$$

where \hat{G}_j is the generator of the local gauge transformation on the site j . Therefore, we can define the physical Hilbert space \mathcal{H}_G as the set of all the gauge invariant states, i.e. all the states which satisfy (2.7):

$$\mathcal{H}_G \equiv \{|\Psi\rangle \in \mathcal{H}_{\text{tot}} \mid \hat{G}_j|\Psi\rangle = 0 \quad \forall j\}. \quad (2.8)$$

An efficient way to construct \mathcal{H}_G is to consider only the elements $|\Phi_G\rangle$ of the basis of \mathcal{H}_{tot} which are gauge invariant

$$\{|\Phi_G\rangle\} \equiv \{|\Psi\rangle \mid \hat{G}_j|\Psi\rangle = 0\}, \quad (2.9)$$

so that the physical Hilbert space is the vector space which is spanned by that basis:

$$\mathcal{H}_G = \text{Span}\{|\Phi_G\rangle\}. \quad (2.10)$$

Which is the number of element of that basis, i.e. the dimension of the physical gauge invariant subspace \mathcal{H}_G of \mathcal{H}_{tot} ? This is, in general, a non-trivial question. For the ladder system, in section 2.3 we present an algorithm to systematically compute $\dim \mathcal{H}_G$ as a function of the number L of plaquettes of the ladder.

2.2.1 Gauss' Law and the problem of the spin representation

In the last section we noticed that in order to construct the gauge invariant subspace of the total Hilbert space \mathcal{H}_{tot} we need to search for all the gauge invariant elements of the basis of \mathcal{H}_{tot} . In the basis of \hat{S}^z , we can simply directly implementing the Gauss' Law for each lattice site of the ladder.

However, here arise a problem for the spin representations with half-integer spins. Indeed, the theory we are dealing with is the pure QED (without matter), so no fermionic excitation are allowed. Taking for instance the lowest spin representation $s = \frac{1}{2}$ we notice that, in the ladder geometry, this representation does not allow for gauge invariant configurations. In other words, there is no way to satisfy the Gauss' Law in a site with three links with $s = \frac{1}{2}$ (Fig. 2.3).

In general, we notice that this problem is extended to all the semi-integer spin representations $s = \frac{1}{2}, \frac{3}{2}, \frac{5}{2}, \dots$

Using semi-integer spins would allow us to reduce the dimensionality of the Hilbert space, in particular with the lowest spin representation $s = \frac{1}{2}$, and this is crucial in terms of computational cost. Therefore, we ask for a solution that allows us to use semi-integer

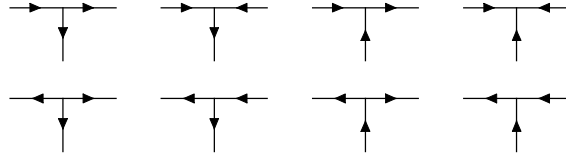


Figure 2.3. Using the spin representation $(s_x, s_y) = (\frac{1}{2}, \frac{1}{2})$, for the ladder, there are 8 total configurations. However, this representation is not compatible with the Gauss' Law: there are no allowed configurations.

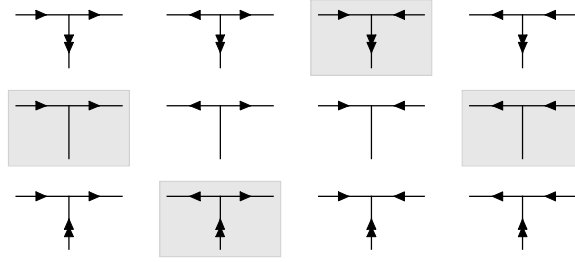


Figure 2.4. Using the spin representation $(s_x, s_y) = (\frac{1}{2}, 1)$, for the ladder, there are 12 total configurations. This representation is compatible with the Gauss' Law, because 4 configurations (highlighted in this figure) are allowed.

spins. One possibility is using different representations for different links. We notice that we want to impose the following constraints for the ladder system:

- if we want to impose *translational invariance* with respect the x -axis, all the L horizontal spin representations must be the same, and the same holds for all the $2L$ vertical spin representations;
- if we want to impose *invariance under reflection with respect the x -axis*, then for each plaquette the top and bottom horizontal spin representation must be the same;

However, we can still use different spin representations for horizontal and vertical links. Letting s_x and s_y the spin representation of the horizontal and vertical links respectively, we denote with

$$(s_x, s_y) \tag{2.11}$$

a generic spin representation of the ladder. The lowest spin representation that allows for gauge invariant configuration is the representation $(\frac{1}{2}, 1)$. Indeed, for each site, we notice that using this representation there are 4 gauge invariant configurations out of 12 total configuration of the lattice site with three neighboring links (Fig. 2.4).

Not all the representations (s_x, s_y) are sensical. In particular, we notice that

- the vertical spin representation s_y must be a *positive integer* because, due to the Gauss' Law, the z -component of the spin s_y^z is a sum or difference of two s_x^z for each site;

| | $s_x = \frac{1}{2}$ | $s_x = 1$ | $s_x = \frac{3}{2}$ | $s_x = 2$ | $s_x = \frac{5}{2}$ | \dots |
|---------------------|---|-------------------------------|---|-------------------------------|---|---------|
| $s_y = \frac{1}{2}$ | $\left(\frac{1}{2}, \frac{1}{2}\right)$ | $\left(1, \frac{1}{2}\right)$ | $\left(\frac{3}{2}, \frac{1}{2}\right)$ | $\left(2, \frac{1}{2}\right)$ | $\left(\frac{5}{2}, \frac{1}{2}\right)$ | \dots |
| $s_y = 1$ | $\left(\frac{1}{2}, 1\right)$ | $(1, 1)$ | $\left(\frac{3}{2}, 1\right)$ | $(2, 1)$ | $\left(\frac{5}{2}, 1\right)$ | \dots |
| $s_y = \frac{3}{2}$ | $\left(\frac{1}{2}, \frac{3}{2}\right)$ | $\left(1, \frac{3}{2}\right)$ | $\left(\frac{3}{2}, \frac{3}{2}\right)$ | $\left(2, \frac{3}{2}\right)$ | $\left(\frac{5}{2}, \frac{3}{2}\right)$ | \dots |
| $s_y = 2$ | $\left(\frac{1}{2}, 2\right)$ | $(1, 2)$ | $\left(\frac{3}{2}, 2\right)$ | $(2, 2)$ | $\left(\frac{5}{2}, 2\right)$ | \dots |
| $s_y = \frac{5}{2}$ | $\left(\frac{1}{2}, \frac{5}{2}\right)$ | $\left(1, \frac{5}{2}\right)$ | $\left(\frac{3}{2}, \frac{5}{2}\right)$ | $\left(2, \frac{5}{2}\right)$ | $\left(\frac{5}{2}, \frac{5}{2}\right)$ | \dots |
| $s_y = 3$ | $\left(\frac{1}{2}, 3\right)$ | $(1, 3)$ | $\left(\frac{3}{2}, 3\right)$ | $(2, 3)$ | $\left(\frac{5}{2}, 3\right)$ | \dots |
| $s_y = \frac{7}{2}$ | $\left(\frac{1}{2}, \frac{7}{2}\right)$ | $\left(1, \frac{7}{2}\right)$ | $\left(\frac{3}{2}, \frac{7}{2}\right)$ | $\left(2, \frac{7}{2}\right)$ | $\left(\frac{5}{2}, \frac{7}{2}\right)$ | \dots |
| $s_y = 4$ | $\left(\frac{1}{2}, 4\right)$ | $(1, 4)$ | $\left(\frac{3}{2}, 4\right)$ | $(2, 4)$ | $\left(\frac{5}{2}, 4\right)$ | \dots |
| $s_y = \frac{9}{2}$ | $\left(\frac{1}{2}, \frac{9}{2}\right)$ | $\left(1, \frac{9}{2}\right)$ | $\left(\frac{3}{2}, \frac{9}{2}\right)$ | $\left(2, \frac{9}{2}\right)$ | $\left(\frac{5}{2}, \frac{9}{2}\right)$ | \dots |
| $s_y = 5$ | $\left(\frac{1}{2}, 5\right)$ | $(1, 5)$ | $\left(\frac{3}{2}, 5\right)$ | $(2, 5)$ | $\left(\frac{5}{2}, 5\right)$ | \dots |
| \dots | | | | | \dots | |

Table 2.2. The first spin representations of the ladder are listed. Only the highlighted ones are consistent representations (s_y is a positive integer and $s_y \leq 2s_x$). We will mainly concentrate in the lowest spin representation $\left(\frac{1}{2}, 1\right)$ in the following sections.

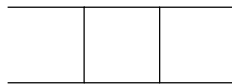
- the *maximum value* of s_y^z is obtained when two maximum values of the horizontal s_x^z converges in a site, which is $s_x + s_x = 2s_x$. Hence, we consider representations such that $s_y \leq 2s_x$.

Therefore, we can consider all the possible spin representations, whose first ones are listed in Tab 2.2.

2.2.2 The local plaquette basis

In order to construct all the gauge invariant electric field configurations of the ladder in a given spin representation, we can think the ladder as a sequence of plaquettes. Hence, having a finite set of plaquette configurations, we can construct the ladder as an ordered sequence of these plaquettes. Given a representation (s_x, s_y) , we first need to determine all the plaquette configurations.

There are many ways to define a plaquette configuration. For instance, we can list all the gauge invariant configurations of a *super-plaquette*, which is composed by a plaquette with its neighboring links:



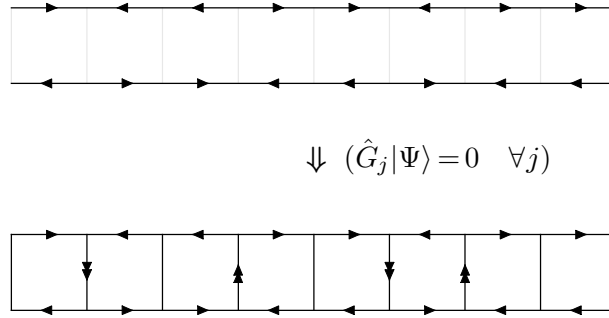


Figure 2.5. The z -projection values of the horizontal link spins are sufficient to univocally determine the z -projection values of the vertical ones, in any spin representation (s_x, s_y) . This allows to use the *semi-plaquette* basis as a local basis of configurations.

However, we adopt a method that allows us to reduce the number of local configurations. We consider instead a so-called *semi-plaquette*, which is composed only of the top and bottom horizontal links:



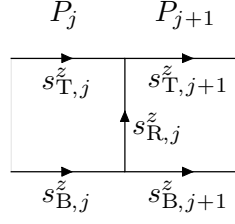
Considering this type of local basis, we notice that, imposing the Gauss' Law for each site, at least with periodic boundary conditions, all the spins of the vertical links are automatically determined (Fig. 2.5). Hence, it is sufficient to give an ordered sequence of L semi-plaquettes to determine univocally a configuration of the chain. Thus, the total number of semi-plaquettes to consider is $(2s_x + 1)^2$, and the set of all semi-plaquettes for the first values of s_x are listed in Tab. 2.3.

| | |
|---------------|--|
| s_x | |
| $\frac{1}{2}$ | |
| 1 | |
| $\frac{3}{2}$ | |
| ... | |

Table 2.3. The semi-plaquettes basis for the first three s_x spin representations.

2.2.3 The rules for neighboring plaquettes

Clearly, the s_y representation sets rules about which plaquettes can follow another one. Hence, we want to find the necessary and sufficient condition for which a semi-plaquette P_j can follow another P_{j+1} , being consistent with the Gauss' Law and with the limiting s_y representation. The two plaquettes can be represented as follows:



The first condition is set by the spin representation of the vertical link:

$$|s_{R,j}^z| \leq s_y. \quad (2.12)$$

Then, applying the Gauss' Law for the top and bottom sites we obtain:

$$\begin{aligned} \text{Gauss' Law on top site: } & s_{T,j}^z + s_{R,j}^z - s_{T,j+1}^z = 0; \\ \text{Gauss' Law on bottom site: } & s_{B,j}^z - s_{R,j}^z - s_{B,j+1}^z = 0, \end{aligned}$$

and isolating $s_{R,j}^z$ from both equations we obtain the condition

$$s_{T,j+1}^z - s_{T,j}^z = s_{R,j}^z = s_{B,j}^z - s_{B,j+1}^z, \quad (2.13)$$

which is equivalent to the condition

$$s_{T,j}^z + s_{B,j}^z = s_{T,j+1}^z + s_{B,j+1}^z. \quad (2.14)$$

Now, defining the sum of the top and bottom electric field as the *local longitudinal polarization*:

$$s_{\parallel,j}^z \equiv s_{T,j}^z + s_{B,j}^z, \quad (2.15)$$

we can write the condition (2.14) as

$$s_{\parallel,j+1}^z = s_{\parallel,j}^z. \quad (2.16)$$

We finally obtain the rule, i.e. a necessary and sufficient condition to determine if P_{j+1} can follow P_j :

$$P_{j+1} \text{ can follow } P_j \iff \begin{cases} s_{\parallel,j+1}^z = s_{\parallel,j}^z \\ |s_{R,j}^z| \leq s_y \end{cases}. \quad (2.17)$$

2.2.4 The longitudinal polarization sectors

It's interesting to notice that, since two neighboring plaquettes *must* have the same longitudinal polarization s_{\parallel}^z , then in a gauge invariant ladder configuration *all* the plaquettes must also have the same s_{\parallel}^z . Hence, the longitudinal polarization is a global property of the system, and the set of all gauge invariant configurations of the ladder splits into sets which are labelled by s_{\parallel}^z (Fig. 2.4).

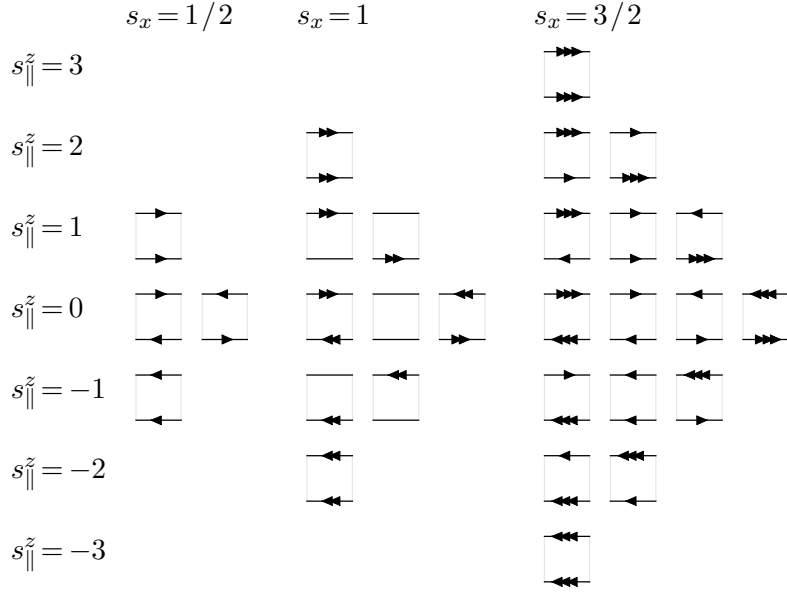


Table 2.4. Each local semi-plaquette basis of Tab. 2.3 is splitted into $4s_x + 1$ groups of semi-plaquettes, each one labeled by the (local) longitudinal polarization s_{\parallel}^z , i.e. the sum between the z -projection spin of the top and bottom horizontal links.

It is simple to show that with an horizontal representation s_x , there are $4s_x + 1$ possible values of the local longitudinal polarization, which are the following

$$-2s_x, -2s_x + 1, -2s_x + 2, \dots, 2s_x - 2, 2s_x - 1, 2s_x. \quad (2.18)$$

In particular, from this follows that the Hilbert space \mathcal{H} of the physical states splits into a direct sum of subspaces $\mathcal{H}(s_{\parallel}^z)$, each one labelled by the local longitudinal polarization

$$\mathcal{H} = \bigoplus_{s_{\parallel}^z = -2s_x}^{2s_x} \mathcal{H}(s_{\parallel}^z). \quad (2.19)$$

In the following sections, we will refer to these subspaces as *longitudinal polarization superselection sectors* because actually the longitudinal polarization operator is a dynamical symmetry invariant, i.e. it commutes with the system's Hamiltonian.

2.3 Counting the gauge invariant configurations

In the previous sections we described the local basis of semi-plaquettes, which simplifies the structure of the physical Hilbert space. However, it is still not known the dimension of the gauge invariant Hilbert subspace of the system, once fixed the spin representation of the ladder.

The problem we want to solve is the following: suppose to have a local basis $\{P_1, P_2, \dots, P_d\}$ of d plaquette configurations^{2.1}. Can we find the number $N(L)$ of configurations of length L of the form

$$P_{i_1} P_{i_2} \dots P_{i_L} \quad \text{with} \quad i_k = 1, \dots, d, \quad k = 1, \dots, L \quad (2.20)$$

that are allowed, i.e. gauge invariant? In the following, we find a systematic way to find a closed form for $N(L)$ as a function of L .

Let's define the *adjacency matrix* M as follows

$$M_{ij} \equiv \begin{cases} 1 & \text{if } P_j \text{ can follow } P_i \\ 0 & \text{otherwise} \end{cases}. \quad (2.21)$$

Now, let be $n_i(k)$ the number of possible configurations of the chain with length k that finishes with the plaquette P_i . The number $n_i(k+1)$ of possible configuration of chains with $k+1$ plaquettes that finishes with the plaquette P_i will be

$$n_i(k+1) = \sum_{j=1}^d \begin{cases} n_j(k) & \text{if } P_j \text{ can follow } P_i \\ 0 & \text{otherwise} \end{cases} = \sum_{j=1}^d M_{ij} n_j(k). \quad (2.22)$$

This is a matrix multiplication: in matrix notation, using $i = 1, \dots, d$ as vector index, we can write (2.22) as

$$\mathbf{n}(k+1) = M \mathbf{n}(k), \quad (2.23)$$

and thus we find recursively

$$\mathbf{n}(L) = M^{L-1} \mathbf{n}(1). \quad (2.24)$$

The number of configurations of a chain with a single plaquette that finishes with a plaquette P_i is 1, so we have $n_i(1) = 1$ and $\mathbf{n}(1)$ is the vector \mathbf{e} with all unit entries:

$$\mathbf{n}(1) = \mathbf{e} \equiv \underbrace{(1, 1, \dots, 1)}_{d \text{ times}}. \quad (2.25)$$

So finally the number of possible configurations N_L^{open} with open boundaries of L plaquettes is obtained summing over all the possible configurations $n_i(L)$:

$$N_L^{\text{open}} = \sum_{i=1}^d n_i(L) = \mathbf{e}^\top \mathbf{n}(L) = \mathbf{e}^\top M^{L-1} \mathbf{e}. \quad (2.26)$$

To find the configurations with *periodic* boundary conditions it is quite simple to show that

$$N_L^{\text{periodic}} = \mathbf{e}^\top (M \circ M^{L-1}) \mathbf{e}, \quad (2.27)$$

where \circ is the *Hadamard product* between matrices defined as

$$(A \circ B)_{ij} \equiv (A)_{ij} (B)_{ij}. \quad (2.28)$$

2.1. In this case, the plaquettes configuration are semi-plaquettes. However, the steps of this sections are valid for any 1-dimensional chain of objects for which we can identify a local set of elements and an adjacency matrix (2.21), i.e. a set of rules which determines what configuration can follow another.

Summing up, we can group the previous results as

$$N_L = \mathbf{e}^\top C \circ M^{L-1} \mathbf{e} \quad C_{ij} \equiv \begin{cases} 1 & \text{open boundaries} \\ M_{ij} & \text{periodic boundaries} \end{cases}. \quad (2.29)$$

Diagonalizing M , it is always possible to find a closed form of the power matrix M^{L-1} , and so a closed form of N_L from (2.29). Thus, we have reduced a combinatorial problem to a diagonalization problem.

We finally notice that the largest eigenvalue λ_{\max} of M is the exponential basis at which the number of configurations increases for very large values of L :

$$N(L) = \mathcal{O}(\lambda_{\max}^L). \quad (2.30)$$

2.3.1 Example with $(\frac{1}{2}, 1)$

In case of the lowest spin representation $(\frac{1}{2}, 1)$, we have the following basis of semi-plaquettes

$$P_1 = \begin{array}{|c|} \hline \rightarrow \\ \hline \leftarrow \\ \hline \end{array}, \quad P_2 = \begin{array}{|c|} \hline \rightarrow \\ \hline \rightarrow \\ \hline \end{array}, \quad P_3 = \begin{array}{|c|} \hline \leftarrow \\ \hline \rightarrow \\ \hline \end{array}, \quad P_4 = \begin{array}{|c|} \hline \leftarrow \\ \hline \leftarrow \\ \hline \end{array}. \quad (2.31)$$

and so, applying the rule (2.17), the adjacency matrix M reads

$$M = \begin{pmatrix} 1 & 0 & 0 & 0 \\ 0 & 1 & 1 & 0 \\ 0 & 1 & 1 & 0 \\ 0 & 0 & 0 & 1 \end{pmatrix}. \quad (2.32)$$

In this specific case the number of configurations are the same in open and periodic boundary configurations:

$$N_L = \mathbf{e}^\top (C \circ M^{L-1}) \mathbf{e} = (1 \ 1 \ 1 \ 1) \begin{pmatrix} 1 & 0 & 0 & 0 \\ 0 & 2^{L-2} & 2^{L-2} & 0 \\ 0 & 2^{L-2} & 2^{L-2} & 0 \\ 0 & 0 & 0 & 1 \end{pmatrix} \begin{pmatrix} 1 \\ 1 \\ 1 \\ 1 \end{pmatrix} = 2^L + 2. \quad (2.33)$$

We notice that this result has a simple interpretation: the 2 states which adds to the 2^L term are due to P_1 and P_4 of (2.31), and they span two 1-dimensional sectors in the Hilbert space. The remaining sector is the one of the chain composed by the two semi-plaquettes P_2 and P_3 . In this case P_2 can follow P_3 and vice versa, so there are 2^L configurations in a chain of L plaquettes. Notice that these configurations are the same of L qubits or $s = \frac{1}{2}$ spins. This is not a random fact: in section 2.6 we will show that this ladder system in representation $(\frac{1}{2}, 1)$ is mappable to the spin- $\frac{1}{2}$ quantum Ising transverse field model.

| (s_x, s_y) | $N(L)$, open boundary |
|--------------------|--|
| $(\frac{1}{2}, 1)$ | $2^L + 2$ |
| $(1, 1)$ | $\frac{1+\sqrt{2}}{2}(1+\sqrt{2})^L + \frac{1-\sqrt{2}}{2}(1-\sqrt{2})^L + 2(2^L + 1)$ |
| $(1, 2)$ | $3^L + 2(2^L + 1)$ |
| $(\frac{3}{2}, 1)$ | $2(2^L + 1) + (1+\sqrt{2})(1+\sqrt{2})^L - (\sqrt{2}-1)(1-\sqrt{2})^L + \frac{5+\sqrt{5}}{5}\left(\frac{3+\sqrt{5}}{2}\right)^L - \frac{\sqrt{5}-5}{5}\left(\frac{3-\sqrt{5}}{2}\right)^L$ |
| $(\frac{3}{2}, 2)$ | $2(3^L + 2^L + 1) + \frac{17-5\sqrt{17}}{34}\left(\frac{3-\sqrt{17}}{2}\right)^L + \frac{17+5\sqrt{17}}{34}\left(\frac{3+\sqrt{17}}{2}\right)^L$ |
| $(\frac{3}{2}, 3)$ | $4^L + 2(3^L + 2^L + 1)$ |
| $(2, 3)$ | $\frac{7+3\sqrt{7}}{14}(2+\sqrt{7})^L + \frac{7-3\sqrt{7}}{14}(2-\sqrt{7})^L + 2(2^L + 3^L + 4^L + 1)$ |
| $(2, 4)$ | $5^L + 2(4^L + 3^L + 2^L + 1)$ |
| $(\frac{5}{2}, 4)$ | $\left(\frac{41+7\sqrt{41}}{82}\right)\left(\frac{5+\sqrt{41}}{2}\right)^L + \left(\frac{41-7\sqrt{41}}{82}\right)\left(\frac{5-\sqrt{41}}{2}\right)^L + 2(5^L + 4^L + 3^L + 2^L + 1)$ |
| $(\frac{5}{2}, 5)$ | $6^L + 2(5^L + 4^L + 3^L + 2^L + 1)$ |

Table 2.5. Number of the gauge-invariant configurations of an open boundary ladder with L plaquettes for some of the first lowest spin representations.

| (s_x, s_y) | $N(L)$, periodic boundary |
|--------------------|---|
| $(\frac{1}{2}, 1)$ | $2 + 2^L$ |
| $(1, 1)$ | $(1-\sqrt{2})^L + (1+\sqrt{2})^L + 2 \cdot 2^L + 3$ |
| $(1, 2)$ | $3^L + 2(2^L + 1)$ |
| $(\frac{3}{2}, 1)$ | $\left(\frac{3+\sqrt{5}}{2}\right)^L + \left(\frac{3-\sqrt{5}}{2}\right)^L + \left(\frac{1+\sqrt{5}}{2}\right)^L + \left(\frac{1-\sqrt{5}}{2}\right)^L + 2(1+\sqrt{2})^L + 2(1-\sqrt{2})^L + 2 \cdot 2^L + 4$ |
| $(\frac{3}{2}, 2)$ | $\left(\frac{3+\sqrt{17}}{2}\right)^L + \left(\frac{3-\sqrt{17}}{2}\right)^L + 2(3^L + 2^L) + 3$ |
| $(\frac{3}{2}, 3)$ | $4^L + 2(3^L + 2^L + 1)$ |
| $(2, 3)$ | $(2-\sqrt{7})^L + (2+\sqrt{7})^L + 2(4^L + 3^L + 2^L) + 3$ |
| $(2, 4)$ | $5^L + 2(4^L + 3^L + 2^L + 1)$ |
| $(\frac{5}{2}, 4)$ | $\left(\frac{5+\sqrt{41}}{2}\right)^L + \left(\frac{5-\sqrt{41}}{2}\right)^L + 2(5^L + 4^L + 3^L + 2^L) + 3$ |
| $(\frac{5}{2}, 5)$ | $6^L + 2(5^L + 4^L + 3^L + 2^L + 1)$ |

Table 2.6. Number of the gauge-invariant configurations of a periodic boundary ladder with L plaquettes for some of the first lowest spin representations.

2.3.2 Higher spin representations

The method previously presented can be applied to higher spin representations (s_x, s_y) of the ladder. Tables 2.5 and 2.6 show the number $N(L)$ of gauge invariant configurations of a ladder of L plaquettes. $N(L)$ is the dimension of the gauge invariant physical subspace, as a function of the length L of the ladder. In particular, Tab. 2.5 shows it in the open boundary case while Tab. 2.6 in periodic boundary.

As we expected, $N(L)$ is a sum of exponentials with different basis. The largest basis, which is the highest eigenvalue of the adjacency matrix, is the leading term in the thermodynamic limit $L \rightarrow \infty$, and it sets the asymptotic behavior of the dimension of the physical Hilbert space in the large L limit. Those asymptotic behavior as a function of s_x and s_y of the spin representation (s_x, s_y) are listed in Tab. 2.7.

| (s_x, s_y) | $s_x = \frac{1}{2}$ | $s_x = 1$ | $s_x = \frac{3}{2}$ | $s_x = 2$ | $s_x = \frac{5}{2}$ |
|--------------|---------------------|---------------------------------|--|---------------------------------|--|
| $s_y = 1$ | $\mathcal{O}(2^L)$ | $\mathcal{O}((1 + \sqrt{2})^L)$ | $\mathcal{O}\left(\left(\frac{3 + \sqrt{5}}{2}\right)^L\right)$ | $\mathcal{O}((1 + \sqrt{3})^L)$ | $\mathcal{O}(2.802^L)$ |
| $s_y = 2$ | - | $\mathcal{O}(3^L)$ | $\mathcal{O}\left(\left(\frac{3 + \sqrt{17}}{2}\right)^L\right)$ | $\mathcal{O}(3.935^L)$ | $\mathcal{O}(4.182^L)$ |
| $s_y = 3$ | - | - | $\mathcal{O}(4^L)$ | $\mathcal{O}((2 + \sqrt{7})^L)$ | $\mathcal{O}(5.119^L)$ |
| $s_y = 4$ | - | - | - | $\mathcal{O}(5^L)$ | $\mathcal{O}\left(\left(\frac{5 + \sqrt{41}}{2}\right)^L\right)$ |
| $s_y = 5$ | - | - | - | - | $\mathcal{O}(6^L)$ |

Table 2.7. The asymptotic estimation for $L \rightarrow \infty$ of the number of gauge-invariant configurations of the ladder for the first lowest spin representations. The diagonal of this table is the representation $(n/2, n)$ described in section 2.3.3.

| | $L = 3$ | $L = 5$ | $L = 7$ | $L = 9$ | $L = 11$ | $L = 13$ |
|-------------------------------|---------|--------------|---------------|---------------|---------------|---------------|
| $\left(\frac{1}{2}, 1\right)$ | 10 | 34 | 130 | 514 | 2'050 | 8'194 |
| $(1, 1)$ | 33 | 149 | 737 | 3'813 | <u>20'337</u> | 111'029 |
| $(1, 2)$ | 45 | 309 | 2'445 | <u>20'709</u> | 181'245 | 1'610'709 |
| $\left(\frac{3}{2}, 1\right)$ | 70 | 366 | 2'088 | <u>12'454</u> | 76'378 | 477'636 |
| $\left(\frac{3}{2}, 2\right)$ | 118 | 1'126 | <u>11'902</u> | 132'598 | 1'527'982 | 18'040'870 |
| $\left(\frac{3}{2}, 3\right)$ | 136 | 1'576 | <u>21'016</u> | 302'536 | 4'552'696 | 70'313'896 |
| $(2, 1)$ | 121 | 685 | <u>4'225</u> | 27'301 | 181'525 | 1'230'241 |
| $(2, 2)$ | 229 | <u>2'655</u> | 33'821 | 451'309 | 6'204'619 | 87'189'985 |
| $(2, 3)$ | 301 | <u>4'765</u> | 84'109 | 1'572'781 | 30'504'829 | 607'022'077 |
| $(2, 4)$ | 325 | <u>5'725</u> | 115'525 | 2'517'805 | 57'575'125 | 1'358'125'885 |

Table 2.8. Explicit number of gauge invariant configurations of the ladder in periodic boundary conditions, computed from expressions of Tab. 2.6 in function of L and for the lowest spin representations. The underlined values represents the limit of L above which the matrix diagonalization of the Hamiltonian of the system becomes computationally intractable in an acceptable time using a laptop ($N(L) \lesssim 20000$).

The highest eigenvalue of the adjacency matrix (2.21) is a root of a characteristic polynomial. Hence, in Tab. 2.7 the basis of some exponential asymptotic behavior is only approximated because it is not possible to find a closed form in terms of square roots.

Finally, Tab. 2.8 shows the number $N(L)$ for the lowest odd L (from 3 to 13) and for the lowest spin representations.

2.3.3 The case $(n/2, n)$

Fixing the horizontal spin representation s_x , the expression for $N(L)$ simplifies as the vertical representation s_y increases. In particular, the expression for $N(L)$ in the spin representation $(n/2, n)$ is the simplest one:

$$N_{(n/2, n)}(L) = (n + 1)^L + 2(1 + 2^L + 3^L + \dots + n^L), \quad n \in \mathbb{N}. \quad (2.34)$$

This particular form is due to the longitudinal polarization sectors described in section 2.2.4. Indeed, for $(n/2, n)$ or other representations with higher s_y the second constraint of (2.17) is always satisfied if two plaquettes have the same longitudinal polarizations. Hence,

for a longitudinal polarization sector with a basis of p plaquettes, there are p^L ways to choose them in a sequence of L plaquettes. Since we discussed the result (2.19) in section 2.2.4 regarding the longitudinal polarization sectors, the number of configurations in case of $(n/2, n)$ can be deduced as

$$N_{(n/2, n)}(L) = 1^L + 2^L + 3^L + \dots + n^L + (n-1)^L + n^L + \dots + 3^L + 2^L + 1^L, \quad (2.35)$$

which is exactly the same result of (2.34).

For spin representations other than $(n/2, n)$, the pattern is no more as simple and the other longitudinal polarizations sectors are “broken”, i.e. they do not follow a simple exponential rule as (2.34). This is the reason why $N(L)$ does not have a very simple closed form.

2.4 Construction of the operators

To construct matrix operators which act on the physical Hilbert space of the ladder system we can directly test the action of the operator over the computational gauge invariant basis we constructed.

To understand the process, let's consider the simplest non-trivial case, which is $L=2$ in representation $(\frac{1}{2}, 1)$. As we showed in section 2.3.1 there is a basis of $N(L=2) = 2^2 + 2 = 6$ basis configurations $|1\rangle, \dots, |6\rangle$, which can be represented as follows (using periodic boundary conditions):

$$\begin{aligned} |1\rangle &= \begin{array}{|c|c|} \hline \rightarrow & \rightarrow \\ \hline \end{array}, & |2\rangle &= \begin{array}{|c|c|} \hline \rightarrow & \rightarrow \\ \hline \end{array}, & |3\rangle &= \begin{array}{|c|c|} \hline \rightarrow & \leftarrow \\ \hline \end{array}, \\ |4\rangle &= \begin{array}{|c|c|} \hline \leftarrow & \rightarrow \\ \hline \end{array}, & |5\rangle &= \begin{array}{|c|c|} \hline \rightarrow & \rightarrow \\ \hline \end{array}, & |6\rangle &= \begin{array}{|c|c|} \hline \leftarrow & \leftarrow \\ \hline \end{array}. \end{aligned} \quad (2.36)$$

In general, an operator acting on a Hilbert space \mathcal{H} of dimension $\dim \mathcal{H}$ can be represented as a $\dim \mathcal{H} \times \dim \mathcal{H}$ matrix using a certain basis choice. An operator \hat{A} of the ladder with $L=2$ in representation $(\frac{1}{2}, 1)$ can be represented in the computational basis (2.36) as

$$\hat{A} = \begin{array}{|c|} \hline |1\rangle \\ |2\rangle \\ |3\rangle \\ |4\rangle \\ |5\rangle \\ |6\rangle \\ \hline \end{array} \begin{pmatrix} |1\rangle & |2\rangle & |3\rangle & |4\rangle & |5\rangle & |6\rangle \\ \hline A_{11} & A_{12} & A_{13} & A_{14} & A_{15} & A_{16} \\ A_{21} & A_{22} & A_{23} & A_{24} & A_{25} & A_{26} \\ A_{31} & A_{32} & A_{33} & A_{34} & A_{35} & A_{36} \\ A_{41} & A_{42} & A_{43} & A_{44} & A_{45} & A_{46} \\ A_{51} & A_{52} & A_{53} & A_{54} & A_{55} & A_{56} \\ A_{61} & A_{62} & A_{63} & A_{64} & A_{65} & A_{66} \end{pmatrix} \quad (2.37)$$

The meaning of the matrix elements in this representation are the pre-factors of the action of the operator \hat{A} on the elements of the basis. For instance, if \hat{A} acts on C_5 as

$$|5\rangle = \begin{array}{|c|c|} \hline \rightarrow & \rightarrow \\ \hline \end{array} \xrightarrow{\hat{A}} \hat{A}|5\rangle = 3 \cdot \begin{array}{|c|c|} \hline \rightarrow & \rightarrow \\ \hline \end{array} + 7 \cdot \begin{array}{|c|c|} \hline \leftarrow & \rightarrow \\ \hline \end{array} = 3|2\rangle + 7|4\rangle \quad (2.38)$$

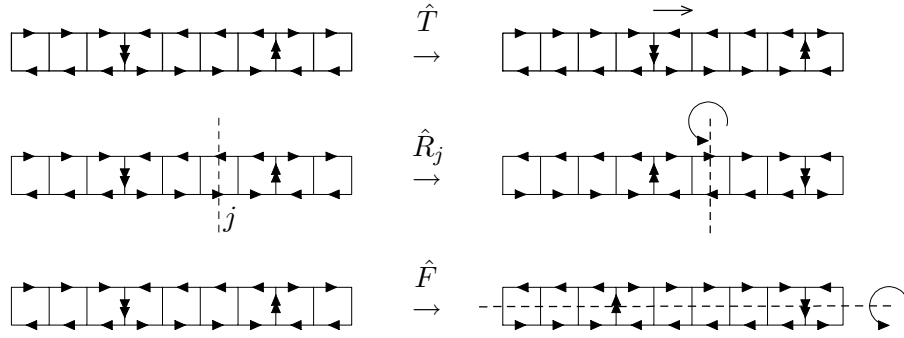


Figure 2.6. An example of the explicit action of the symmetry operators \hat{T} , \hat{R}_j and \hat{F} on a particular ladder gauge invariant configuration.

then we have to set $A_{52} = 3$ and $A_{54} = 7$ and all the others $A_{5i} = 0$. If the action of \hat{A} over a configuration is not a gauge invariant configuration (i.e. which breaks the Gauss' Law) or not admitted to the spin representation, the associated matrix element will be vanishing.

This method to construct operators in the computational basis can be extended to any basis in any spin representation, for any operator \hat{A} for which the action on every element of the computational basis is known.

2.4.1 The translation operator \hat{T}

The translation operator is well defined only in periodic boundary conditions. Given a sequence of plaquettes, i.e. an element of the gauge invariant computational basis, the translation operator \hat{T} translates *cyclically by right* all the plaquettes by one unit (Fig. 2.6).

For instance, for five plaquettes P_1, \dots, P_5 the action of \hat{T} is the following:

$$\hat{T}|P_1 P_2 P_3 P_4 P_5\rangle = |P_5 P_1 P_2 P_3 P_4\rangle. \quad (2.39)$$

Since the translation operator is a symmetry operator, it preserves the scalar products and norm of the states, hence it is a *unitary* operator:

$$\hat{T}\hat{T}^\dagger = \hat{T}^\dagger\hat{T} = \mathbb{I}, \quad \hat{T}^\dagger = \hat{T}^{-1}, \quad [\hat{T}, \hat{T}^\dagger] = 0. \quad (2.40)$$

From the operator \hat{T} we can simply find the translation operator of n units as

$$\hat{T}_{(n)} \equiv \underbrace{\hat{T}\hat{T}\dots\hat{T}}_n = \hat{T}^n. \quad (2.41)$$

For a system of length L with periodic boundary conditions applying L times is equivalent to the identity:

$$\hat{T}^L = \mathbb{I}. \quad (2.42)$$

The eigenvectors of the translation operators are denoted as $|k\rangle$, and the corresponding eigenvalues are well known complex phases:

$$\hat{T}|k, \alpha\rangle = e^{ik}|k, \alpha\rangle, \quad (2.43)$$

where α is a degeneration removing index (depending on the particular system) and k are the 1-dimensional (Bloch) quasi-momenta

$$k = \frac{2\pi}{L}\tilde{k}, \quad \tilde{k} = \begin{cases} -\frac{L-1}{2}, \dots, \frac{L-1}{2} & \text{if } n \text{ odd} \\ -\frac{L}{2} + 1, \dots, \frac{L}{2} & \text{if } n \text{ even} \end{cases}. \quad (2.44)$$

The variable $\tilde{k} \in \mathbb{Z}$ is just a rescaling of k and it is an integer value sometimes referred as (crystal) *momentum index*. Thus, we can use k or \tilde{k} to label the eigenvalues of \hat{T} . In the next chapters, we may omit the tilde \tilde{k} in some cases, referring to the momentum index to label the quasi-momenta^{2.2}.

2.4.2 Reflection operators \hat{R} and \hat{F}

A generic *reflection operator* \hat{R} can be defined with respect a given axis. It must satisfy the following properties:

- a) it is a *unitary* operator: $\hat{R}^\dagger \hat{R} = \hat{R} \hat{R}^\dagger = \mathbb{I}$, because it is a symmetry operator;
- b) it is an *involutory* operator: $\hat{R}^2 = \mathbb{I}$, because a reflection applied twice must be the identity;
- c) from properties (a) and (b) immediately follows that it must be also *Hermitian* i.e. $\hat{R}^\dagger = \hat{R}$.

From the previous properties, \hat{R} is an observable, and a generic eigenvalue of \hat{R} can be $r = \pm 1$, which is called the *parity* under a given reflection.

For the ladder system, we denote as \hat{R}_j as the reflection operator with respect an axis which is parallel to the y -axis and centered on the j -th plaquette (Fig. 2.6).

Hence, as previously said, the properties of \hat{R}_j are

$$\hat{R}_j^\dagger \hat{R}_j = \hat{R}_j \hat{R}_j^\dagger = \mathbb{I}, \quad \hat{R}_j^2 = \mathbb{I}, \quad \hat{R}_j^\dagger = \hat{R}_j. \quad (2.45)$$

It is simple to show the following property, which relates the reflection operator and the translation operator:

$$\hat{R}_j \hat{R}_l = \hat{T}^{2j-2l}. \quad (2.46)$$

The property $\hat{R}_j^2 = \mathbb{I}$ is a special case of (2.46), obtained setting $j = l$.

The action of \hat{T} and \hat{R} are not independent, and this brings to a nontrivial commutation relation:

$$[\hat{T}, \hat{R}_j] \neq 0. \quad (2.47)$$

In general, for any 1-dimensional system, one can show in a simple way the following property:

$$\hat{R}_j \hat{T} \hat{R}_j^\dagger = \hat{T}^\dagger. \quad (2.48)$$

^{2.2} The issue if k or \tilde{k} is used can be resolved depending on the context, and it will be specified if needed.

This has an intuitive explanation: applying the action of a reflection to a translation means inverting the direction of the translation, i.e. considering the inverse \hat{T}^\dagger of the translation \hat{T} . Hence, we obtain the following nontrivial commutation rule between these two operators:

$$\hat{T}\hat{R}_j - \hat{R}_j\hat{T}^\dagger = 0. \quad (2.49)$$

The reflection operator with respect the x -axis will be denoted as \hat{F} , and it will be referred as the *flip operator* of the ladder (Fig. 2.6). Being a reflection operator, it satisfies the previously listed properties:

$$\hat{F}^\dagger\hat{F} = \hat{F}\hat{F}^\dagger = \mathbb{I}, \quad \hat{F}^2 = \mathbb{I}, \quad \hat{F}^\dagger = \hat{F}. \quad (2.50)$$

Furthermore, the x -axis reflection \hat{F} is independent with respect the y -axis reflection \hat{R} and with respect the translation \hat{T} , so \hat{F} must commute with both the operators:

$$[\hat{R}_j, \hat{F}] = 0, \quad [\hat{T}, \hat{F}] = 0. \quad (2.51)$$

2.4.3 The Hamiltonian operator \hat{H}

From section 1.3.1 we can write the Hamiltonian of the ladder system as

$$\hat{H} = \hat{H}^E + \hat{H}^B = \frac{g^2}{2a} \sum_{l=1}^{N_l} (\hat{S}_l^z)^2 + \frac{1}{2ag^2} \sum_{j=1}^L (\hat{S}_{j,B}^+ \hat{S}_{j,R}^+ \hat{S}_{j,T}^- \hat{S}_{j,L}^- + \text{H.c.}), \quad (2.52)$$

where $l = 1, \dots, 3L$ runs over all the links and $j = 1, \dots, L$ runs over all the plaquettes.

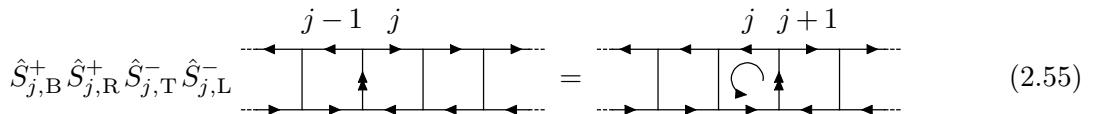
To construct the Hamiltonian operator, we have to consider the action of the spin operators on the spin basis $|s, s^z\rangle$:

$$\hat{S}^z |s, s^z\rangle = s^z \hat{S}^z |s, s^z\rangle, \quad (2.53)$$

$$\hat{S}^\pm |s, s^z\rangle = \sqrt{s(s+1) - s^z(s^z \pm 1)} |s, s^z \pm 1\rangle. \quad (2.54)$$

The operators \hat{S}_l^z are Hermitian, while the term +H.c. in (2.52) ensures that $\hat{H}^\dagger = \hat{H}$. Hence, the matrix constructed as described previously must be an Hermitian matrix.

The term \hat{H}_B is referred also as an *hopping term*, due to the particular ‘‘hopping’’ action of its 4-spin plaquette operator:



$$\hat{S}_{j,B}^+ \hat{S}_{j,R}^+ \hat{S}_{j,T}^- \hat{S}_{j,L}^- \quad (2.55)$$

Translation and reflection are symmetries of the Hamiltonian, i.e. the Hamiltonian is invariant under the action of translation and reflections operators:

$$\hat{T}\hat{H}\hat{T}^\dagger = \hat{H}, \quad \hat{T}\hat{R}_j\hat{T}^\dagger = \hat{H}, \quad \hat{T}\hat{F}\hat{T}^\dagger = \hat{H}. \quad (2.56)$$

This means that all the symmetry operator defined above commutes with the Hamiltonian:

$$[\hat{H}, \hat{T}] = 0, \quad [\hat{H}, \hat{R}_j] = 0, \quad [\hat{H}, \hat{F}] = 0. \quad (2.57)$$

2.4.4 The local Hamiltonian operators \hat{H}_j

The Hamiltonian operator can be naturally written as a sum of “local” Hamiltonians \hat{H}_j . The term “local” in this context means that each operator \hat{H}_j acts on the single j -th plaquette. In particular we have

$$\hat{H} = \sum_{j=1}^L \hat{H}_j, \quad \hat{H}_j = \hat{H}_j^E + \hat{H}_j^B. \quad (2.58)$$

where \hat{H}_j^E and \hat{H}_j^B are defined^{2.3} as:

$$\hat{H}_j^E \equiv \frac{g^2}{2a} \left[\frac{1}{2} (\hat{S}_{j,L}^z)^2 + (\hat{S}_{j,T}^z)^2 + (\hat{S}_{j,B}^z)^2 + \frac{1}{2} (\hat{S}_{j,R}^z)^2 \right], \quad (2.59)$$

$$\hat{H}_j^B \equiv \frac{1}{2ag^2} (\hat{S}_{j,B}^+ \hat{S}_{j,R}^+ \hat{S}_{j,T}^- \hat{S}_{j,L}^- + \text{H.c.}). \quad (2.60)$$

Clearly, the action of the symmetry operators over the local Hamiltonians are straightforward to derive. Indeed, the translation operator applied to the local Hamiltonian \hat{H}_j must return the local Hamiltonian of the next plaquette:

$$\hat{T} \hat{H}_j \hat{T}^\dagger = \hat{H}_{j+1}. \quad (2.61)$$

The reflection operator \hat{R}_j inverts the position of the local Hamiltonian with respect the j -th plaquette

$$\hat{R}_j \hat{H}_{j'} \hat{R}_j^\dagger = \hat{H}_{2j-j'}, \quad (2.62)$$

while each local Hamiltonian remains invariant under the action of the flip operator:

$$\hat{F} \hat{H}_j \hat{F}^\dagger = \hat{H}_j. \quad (2.63)$$

2.5 The energy-momentum dispersion relation

The dispersion relation, also known as the *energy-momentum relation*, is a fundamental concept in many-body physics. It describes the relationship between the energy (or frequency) and momentum of particles within a system. By plotting the dispersion relation on a graph, with energy on the vertical axis and momentum on the horizontal axis we

^{2.3} For each plaquette, the vertical links are common rungs between the neighboring plaquettes. Hence, to compute the electric energy per plaquette, we multiply by a factor 1/2 the vertical contribution of the electric field energy in the definition of \hat{H}_j^E .

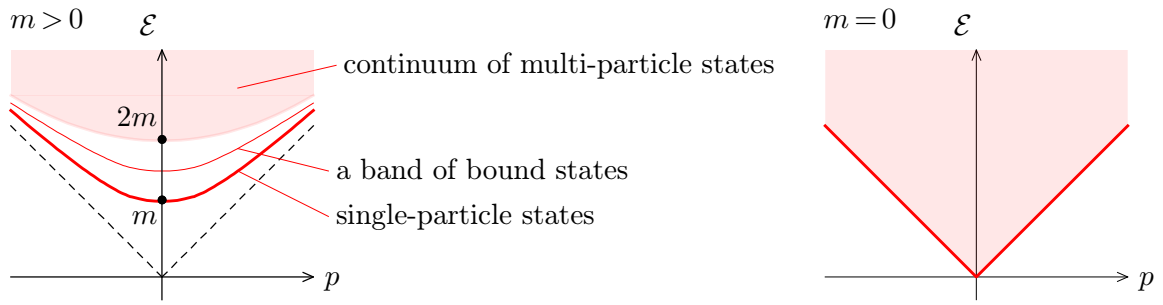


Figure 2.7. Eigenvalues of the 4-momentum operator $P^\mu = (H, \mathbf{P})$ for a relativistic quantum field theory in the case of massive particles $m > 0$ and massless particles $m = 0$.

obtain information about the behavior of the quasi-particles involved. It is crucial in understanding phenomena such as wave propagation, particle interactions, and collective excitations in condensed matter physics, quantum field theory, and other branches of physics, enabling the study and prediction of the system's dynamic properties.

The dispersion relation is obtained via simultaneous diagonalization of the Hamiltonian \hat{H} and the momentum \hat{P} operator. However, since the momentum operator \hat{P} is difficult to construct^{2.4}, we diagonalize the unitary translation operator \hat{T} to get the eigenvalues of \hat{P} , being the momentum operator the generator of the translations.

2.5.1 Dispersion relation in a continuous quantum field theory

In a typical relativistic Quantum Field Theory, the eigenvalues of the 4-momentum operator $\hat{P}^\mu = (\hat{H}, \hat{\mathbf{P}})$ for a *free* particle organize themselves into hyperboloids in the plane $|\mathbf{p}|$, \mathcal{E} . For a massive particle of mass m , the single-particle states with momentum \mathbf{p} follow the dispersion relation^{2.5}

$$\mathcal{E} = \omega = \sqrt{|\mathbf{p}|^2 + m^2}. \quad (2.64)$$

which is an hyperboloid passing through the 4-momentum point $(m, 0)$. We stress that, since we must impose the *positivity* of the energy \mathcal{E} , the hyperboloids are composed of a *single sheet* in the upper plane with $\mathcal{E} > 0$. A continuum region above the hyperboloid passing through 4-momentum point $(2m, 0)$ represents the multi-particle states, while between the single and multi-particle band states there may also be one or more hyperboloids which represents one or more bound states of the theory (Fig. 2.7).

If the particle is massless, so $m = 0$, the single particle hyperboloid coincides with the upper light-cone, and the same light-cone is the lower threshold of the continuum multi-particle state region.

^{2.4.} To compute \hat{P} we should take the matrix logarithm of \hat{T} , which is computationally a complex operation for large matrices.

^{2.5.} We recall that we are using the units convention $c = 1$, $\hbar = 1$.

The velocity β of the particle with momentum k_0 is defined as the *group velocity*, which is the derivative of the frequency ω with respect the momentum k , computable from the dispersion relation:

$$\beta(k_0) \equiv \left. \frac{d\omega(k)}{dk} \right|_{k=k_0} = \left. \frac{d\mathcal{E}(p)}{dp} \right|_{p=k_0}. \quad (2.65)$$

The second derivative of the frequency with respect the momentum of a particle with momentum k_0 instead represents the dispersion of a wave-packet formed by the states k_0 , and it is commonly referred as *dispersion slope*

$$\beta'(k_0) \equiv \left. \frac{d^2\omega(k)}{d^2k} \right|_{k=k_0} = \left. \frac{d^2\mathcal{E}(p)}{d^2p} \right|_{p=k_0}. \quad (2.66)$$

For a relativistic dispersion relation (2.64) for very large momenta we have $\beta' \rightarrow 0$. For the massless particle case, such as the photon, $\beta' = 0$ holds for all momenta^{2.6}. Hence, wave-packets corresponding to massless particles are non-dispersive, i.e. they propagate without changing shape. In order to construct a wave-packet which is less dispersive as possible, we need to localize the momentum k_0 in a region of the dispersion relation where β' is minimum.

In case of an *interacting* particle, the nature of the interaction can change its dispersion relation. However, all the considerations about the group velocity and the dispersion slope are the same: solving the interacting problem (i.e. computing the eigenvalues of the interacting energy-momentum operator), allows for the identification of wave-packets of single-particle states which propagates almost dispersionlessly, even if the particle is self-interacting. This is actually the power of the algorithm of wave-packet creation that we will present in the next chapter.

2.5.2 Dispersion relation in a lattice theory

Let's consider the case of a $(1+1)$ -dimensional spacetime. In the framework of Hamiltonian lattice gauge theory, we need to discretize only the space, while the time t remains continuous. Let's consider a discretization of the 1-dimensional space with lattice spacing a . The resulting modification of the reciprocal space of momenta k is that the space becomes *periodic* with period $2\pi/a$. The region $[-\pi/a, \pi/a]$ is the so-called *first Brillouin Zone* (BZ). Indeed, for $a \rightarrow 0$ (the continuum limit) the Brillouin Zone is the whole \mathbb{R} line.

When the space is discretized, the structure of the energy bands in the dispersion relation diagram becomes periodic in the reciprocal space and other many-body bands becomes to appear (Fig. 2.8). The exact structure of these dispersion relation diagrams is highly non-trivial and it depends on many factors such as the interactions of the theory and the way the theory has been discretized on the lattice (e.g. the truncation of the spectrum of the operators).

^{2.6} Except for $k=0$, however there is no reference frame in which a massless particle has vanishing momentum.

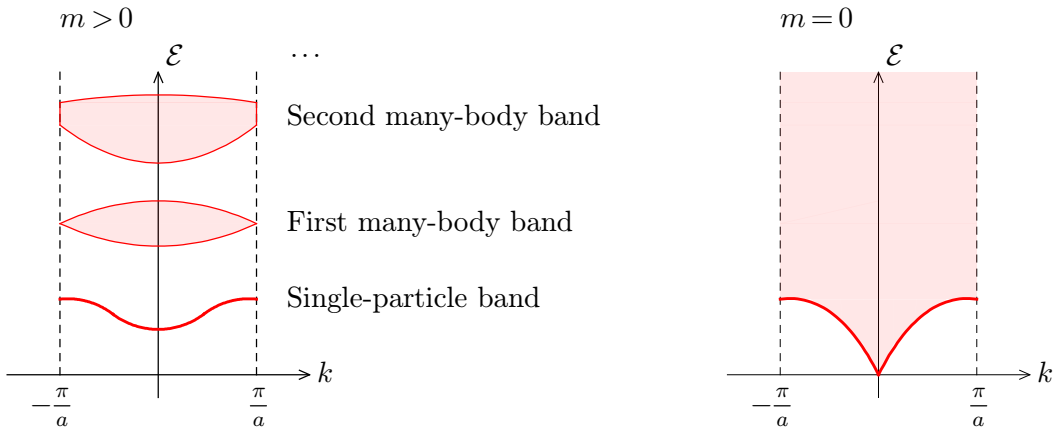


Figure 2.8. Typical dispersion relations of a 1-dimensional lattice theory with lattice discretization a , for $m > 0$ and $m = 0$. This kind of graphs can be obtained considering dispersion relation of a finite lattice with L sites and performing the thermodynamic limit ($L \rightarrow \infty$). The dispersion relation of Fig. 2.7 can be instead obtained considering low momenta ($k \sim 0$) in the continuum limit ($a \rightarrow 0$).

To compute these diagrams, one must necessarily consider a finite^{2.7} lattice with L sites in periodic boundary conditions^{2.8}. This allows to represent a state of the system in a finite Hilbert space. In this case also the number of eigenvalues of the energy-momentum operator becomes finite, and the reciprocal space becomes discrete. Hence, the continuous bands of Fig. 2.8 becomes a discretized set of points (see for instance the diagrams of section 2.5.4). Each point of the reciprocal space is labelled with the momentum eigenvalue, which are the exponents of the eigenvalues of the translation operator \hat{T} .

In this context, the single particle band represents the so called *quasi-particle* states, because particles in this systems are emergent phenomena to be intended as collective excitations of the many-body components rather than real actual particles.

2.5.3 The tight binding condition

The *tight binding* is a simplified model used in condensed matter physics to describe the electronic structure of a solid material. It is particularly useful for studying the behavior of electrons in a crystalline lattice. The model assumes that the electrons in the solid occupy atomic orbitals and interact primarily with their neighboring atoms.

When applied to a 1-dimensional lattice, i.e. a linear chain of sites, the tight binding model considers the nearest-neighbor interactions only. The Hamiltonian is constructed by taking into account the on-site energy of each atom and the hopping term between neighboring atoms. The *nearest neighboring tight binding Hamiltonian* for a 1-dimensional lattice can be written as

$$\hat{H} = \sum_j \varepsilon_j \hat{c}_j^\dagger \hat{c}_j + \sum_j t_{j,j+1} \hat{c}_j^\dagger \hat{c}_{j+1}, \quad (2.67)$$

^{2.7}. An infinite lattice is clearly computationally intractable.

^{2.8}. In order to define a translation operator \hat{T} , one has to impose periodic boundary conditions.

where j spans over all the sites of the chain, \hat{c}_j^\dagger and \hat{c}_j are the creation and annihilation operator for a (quasi)particle, ε_j is the on-site energy and $t_{i,j}$ is the hopping integral between sites i and j .

For a simple tight binding model in a periodic lattice with spacing a , the first band dispersion relation can be described by the cosine function:

$$E(k) = E_0 - 2t \cos(ak). \quad (2.68)$$

This means that, every time we find a single-band isolated dispersion relation which the form is approximated by (2.67), the dynamics of the system is approximately described by the tight-binding Hamiltonian (2.67). In particular, for the tight binding is required that the ratio between the bandwidth $\Delta\mathcal{E}$ and the gap Δ_0 is small ($\Delta\mathcal{E}/\Delta_0 \ll 1$) i.e. the energy band is distant from the others.

The tight binding model can be useful for protecting a single quasi-particle wave-packet from dispersion due to its localized nature. This is because the hopping between sites is typically stronger for nearest neighbors, and the tight binding model assumes negligible hopping beyond that. This localization can be advantageous for preserving the coherence and integrity of the wave-packet over time, allowing it to propagate through the lattice with minimal distortion or loss of information.

However, we stress that the tight binding alone is not a necessary but only a *sufficient* condition to create wave packets protected from dispersion. Additional factors, such as *conserved quantities*, can indeed play a role in preserving the non-dispersive structure of wave packets.

2.5.4 Dispersion relations of the ladder system

We suppose^{2.9} that for our 1-dimensional (discretized, finite) ladder system, the couple of operators $\{\hat{H}, \hat{T}\}$ form a *complete set of compatible observables*. In other words, we assume that it exists a *complete* basis $\{|\mathcal{E}, k\rangle\}$ of the Hilbert space, whose vectors are also common eigenstates \hat{H} and \hat{T} , namely

$$\hat{H}|\mathcal{E}, k\rangle = \mathcal{E}|\mathcal{E}, k\rangle, \quad \hat{T}|\mathcal{E}, k\rangle = e^{ik}|\mathcal{E}, k\rangle. \quad (2.69)$$

The fact that the operators \hat{H} and \hat{T} are simultaneously diagonalizable is guaranteed by the commutation relation $[\hat{H}, \hat{T}] = 0$. The assumption of completeness of $\{|\mathcal{E}, k\rangle\}$ instead ensures that each eigenvector and eigenvalue is non-degenerate.

In this section we show and comment the dispersion relation diagrams in the plane (k, \mathcal{E}) for the ladder system introduced at the beginning of this chapter. We consider a ladder of L plaquettes and lattice spacing $a = 1$, varying the electric field relative interaction strength g .

To obtain the dispersion relation diagrams, we numerically simultaneously diagonalize both the operators \hat{H} (with eigenvalues \mathcal{E}) and \hat{T} (with eigenvalues e^{ik}) for different values of g . From the eigenvectors e^{ik} of the translation operator \hat{T} we compute the momentum k . Thus, we select all the couples (k, \mathcal{E}) and we represent them in a plane. The most efficient

^{2.9} This supposition is confirmed later by direct numerical computations of the eigenvalues of \hat{H} and \hat{T} .

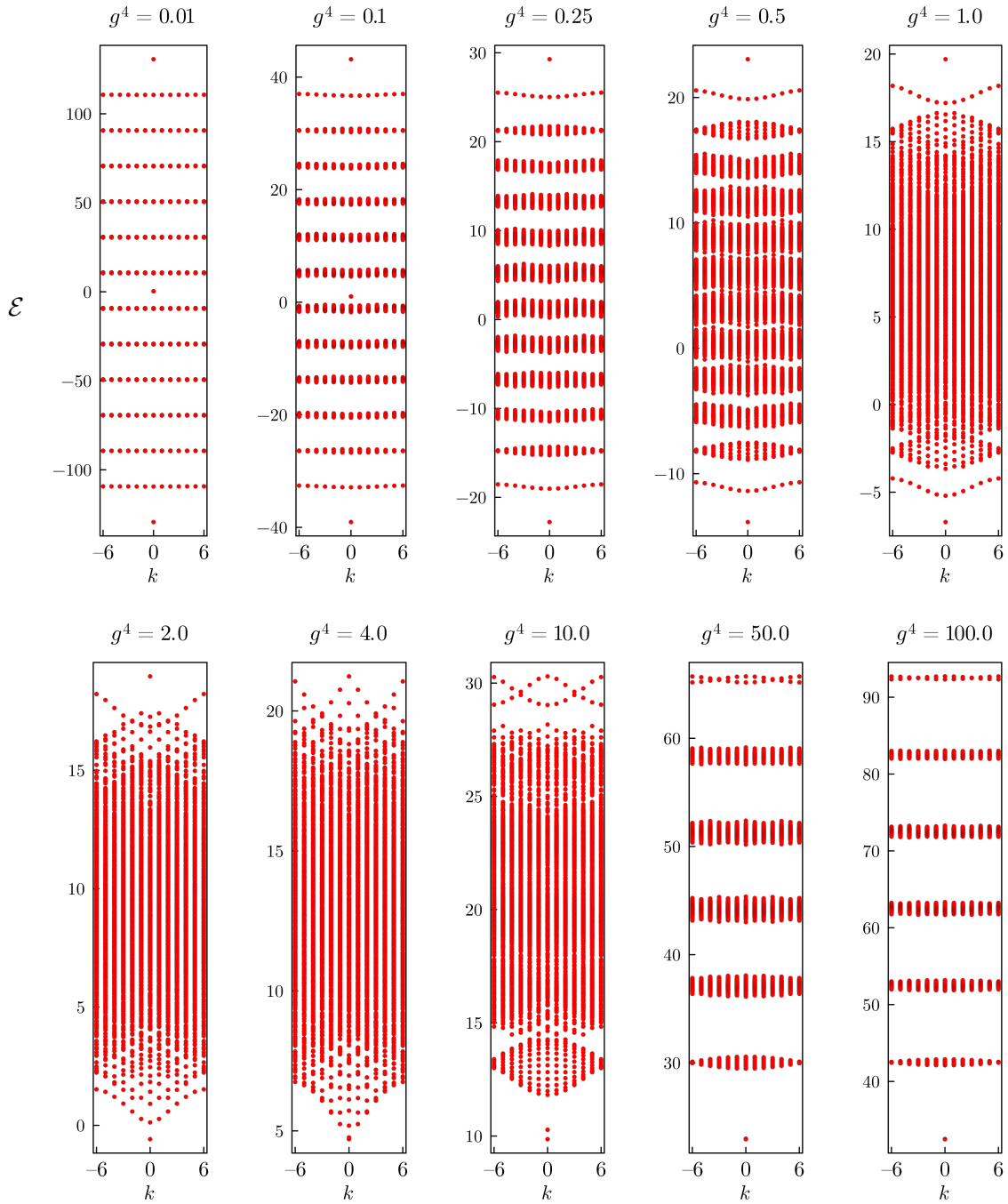


Figure 2.9. Energy-momentum dispersion relation diagrams for a ladder system with spin representation $(\frac{1}{2}, 1)$ and $L=13$.

way to simultaneously diagonalize these operators will be discussed in the next chapter, where more technical details about numerical computations are reported.

Lowest spin representation $(\frac{1}{2}, 1)$ Fig. 2.9 shows the dispersion relation graphs of a $L=13$ ladder system for different electric field strength (from $g^4=0.01$ to $g^4=100$) in the spin representation $(\frac{1}{2}, 1)$.

First, we notice that the ground state $|\Omega\rangle$ is non-degenerate for $g \rightarrow 0$, and degenerate

(with degeneration 2) for $g \rightarrow \infty$. The energies \mathcal{E} assumes also negative values, but this is not an issue because we always consider differences $\mathcal{E} - \mathcal{E}_\Omega = \Delta\mathcal{E} \geq 0$ between the energy \mathcal{E} of a state and the ground state energy \mathcal{E}_Ω , which are always non-negative. For $g^4 < 4$ we also notice a non-degenerate state with maximum energy \mathcal{E}_{\max} . This has a symmetric structure with respect the ground state, and the band below this maximum-energy state represents the dispersion relation of a *hole* created from the eigenstate of energy \mathcal{E}_{\max} . Anyway, we are always interested to the first lower energy band which should represent the single-photon states created from the vacuum.

We comment all the different regimes varying the coupling g :

- **$g \rightarrow 0$.** For very low values of the coupling all the energy bands are flat. This means that the quasi-particle representing photons does not propagate for $g \rightarrow 0$, because the group velocity of these particles in this regime is $\beta = 0$. The same holds for all the above many-particle bands.
- **$g \lesssim 1.0$.** As g increases, the bandwidth $\Delta\mathcal{E}_1$ of the single-particle dispersion relation grows and the ratio $\Delta_0/\Delta\mathcal{E}_1$ reduces, where Δ_0 is the energy gap^{2.10} of the system. Since $\Delta_0 > 0$, in this regime we are describing a (slow) propagating *massive photon*. Furthermore, in this regime the first energy band is isolated and with a cosine-shape (2.68), thus the tight binding condition is satisfied. Hence, with these conditions the photonic wave-packets are protected by the tight-binding, but photons are still slow because they are massive.
- **$g^4 \simeq 2.0$** all the many-body energy bands mix together and they are no more distinct. The first quasi-particle energy band remains visible but not isolated, and the tight binding condition no more holds. The photon mass decreases.
- **$g^4 = 4.0$,** the gap Δ_0 vanishes. This is the critical point in which a *quantum phase transition* occurs, from the deconfined to a confined phase. The photon becomes massless and it propagates at the speed of light for enough small values of momenta. This is the regime in which the quasi-particle more resembles real photons. This is the most distant regime from the tight binding condition, so the particle dynamics is in general non-local and dispersive. However, as we will see in section 2.6, the system is equivalent to the Ising model, which has many conserved quantities which protect the wave-packets from dispersion.
- **$g^4 > 4.0$.** In this regime, the photon returns to be massive, but the first single-particle energy band is no more isolated as in the deconfined phase case. Two

^{2.10.} The gap $\Delta_0 \equiv \mathcal{E}_1 - \mathcal{E}_\Omega$ is defined as the energy difference between the ground-state and the first excited state.

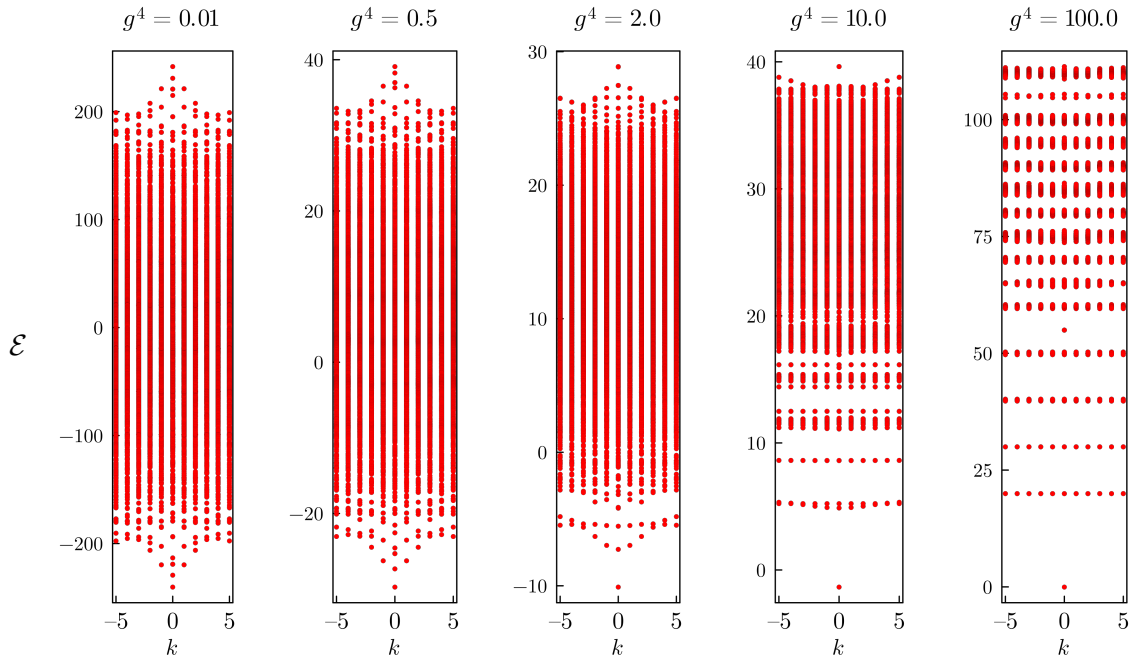


Figure 2.10. Energy-momentum dispersion relation diagrams for a ladder system with spin representation $(1, 1)$ and $L = 11$.

interesting distinct symmetric over-imposed energy bands appear in the hole region.

- $g \rightarrow \infty$. All the energy bands returns to be flat, no photon propagation is allowed. This fact is actually valid for all the spin representations and it is coherent with the Hamiltonian structure: without the magnetic (hopping) term in the Hamiltonian, no propagation of quasi-particles is allowed.

The analysis in the lowest spin representation has been done in detail because it will be the representation chosen for the numerical simulations of the next chapters.

The spin representations $(1, 1)$, $(1, 2)$ Even if we will not use them for real-time numerical simulation, we now analyze the dispersion relations in the case of higher spin representations.

We first set $s_x = 1$. As described in section 2.2.1, in this case we have just two non-trivial cases for s_y , which are $s_y = 1$ and $s_y = 2$:

- **Case $(1, 1)$.** If we set $(s_x, s_y) = (1, 1)$ and $L = 11$ the dispersion relation for different values of g is that of Fig. 2.10. Differently from the $(\frac{1}{2}, 1)$ case, there are no flat energy-bands for $g \rightarrow 0$. Even for very small couplings, the first single-particle band is not isolated (for $s_y < 2s_x$ the longitudinal polarization sectors are “broken” as discussed in section 2.3.3). For $g^4 \simeq 2.0$, a single-particle band appears, but another (flat, non propagating) band with the same energy is over-imposed to it. This

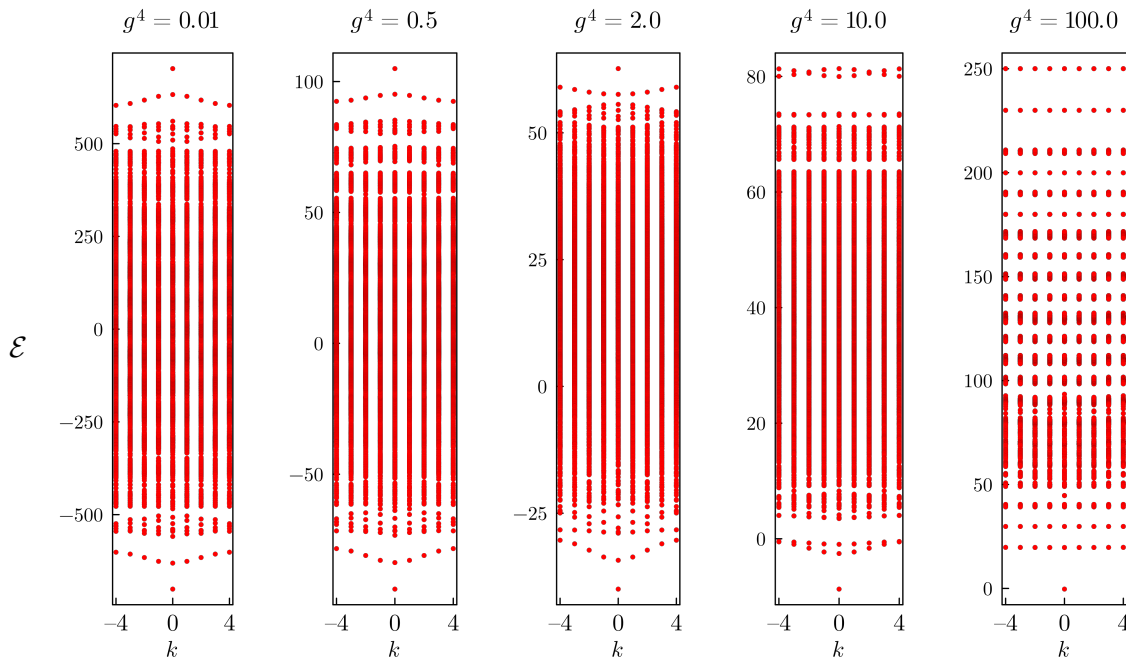


Figure 2.11. Energy-momentum dispersion relation diagrams for a ladder system with spin representation $(1, 2)$ and $L = 9$.

is probably a longitudinal polarization mode, allowed by the Lorentz symmetry breaking of the lattice. For $g \rightarrow 0$, the energy bands become flat, as expected.

- **Case $(1, 2)$.** If we set $(s_x, s_y) = (1, 1)$ and $L = 9$ the dispersion relation for different values of g is that of Fig. 2.11. Also in this case, there are no flat energy-bands for $g \rightarrow 0$. However, for $g \rightarrow 0$ a single definite energy band is recovered in this spin representation (all the longitudinal polarization sectors are un-broken). However, we notice that for any value of the coupling g the system has a non-vanishing gap $\Delta_0 > 0$. This means that the photon remains massive for any value of the coupling in this spin representation.

The case $s_x = 3/2$ and higher spin representations For spin representations equal or higher than $s_x = 3/2$ the computational cost for diagonalization becomes large. Hence, only systems with $L \leq 7$ can be simulated. The fact that the single-band structure is recovered

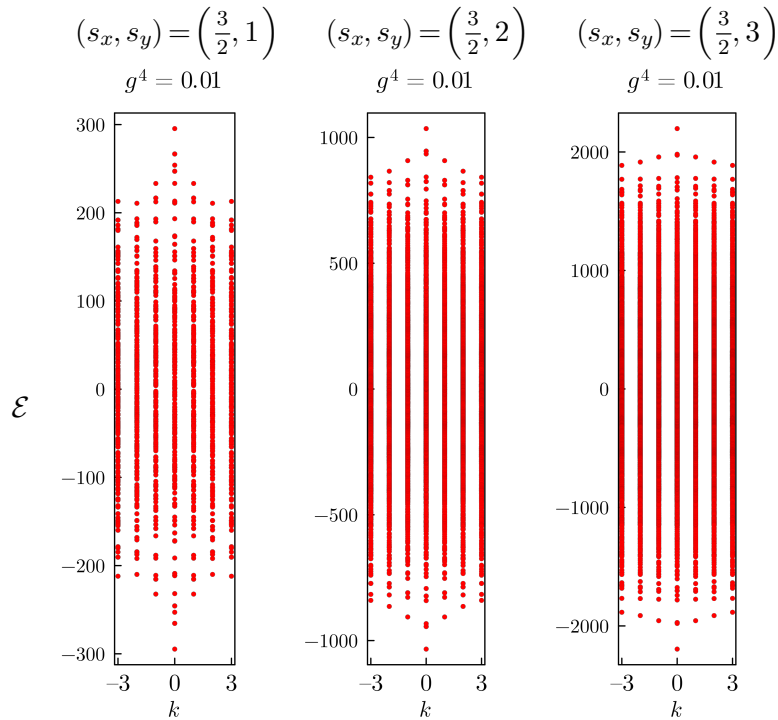


Figure 2.12. Energy-momentum dispersion relation diagrams for a ladder system with $g^4 = 0.01$ and $L = 7$ and different higher spin representations. In particular, here we consider spin representations with $s_x = 3/2$, and different s_y . Notice that, as s_x gets closer to $s_y = 2s_x$, the single-particle band becomes distinct.

when $s_y \simeq 2s_x$ seems to be valid also for higher spin representations. Figure 2.12 shows the cases for $g^4 = 0.1$ and $s_y = 1, 2, 3$. For $s_y = 1$, there is no single-particle energy band and (the polarization sectors structure of the Hilbert space is completely broken). For $s_y = 2$ a single-particle band is more visible and for $s_y = 3$ is completely recovered. We conjecture that this kind of behavior is valid also for higher spin representation.

Another comment is about the gap Δ_0 of the system. For higher spin representations, it seems that there are no more gapless phases as in the $(\frac{1}{2}, 1)$ case. This constitutes an indication that the propagating photon is probably a massive particle in the continuous counterpart of the model (the QED₂ with infinitesimal width).

It is interesting to notice that, at least in terms of dispersion relation, the quasi-particles of the most simplified model with $(\frac{1}{2}, 1)$ spin representation at the critical point ($g = \sqrt{2}$) are actually more similar to the real (3 + 1)-QED photons with respect the quasi-particles of the ladder system with higher spin representations.

2.6 Mapping $(\frac{1}{2}, 1)$ ladder to 1D Ising transverse field

A *mapping* between two quantum systems is an exact one-by-one correspondence between the Hilbert spaces and Hamiltonians of two different quantum systems. A mapping is typically employed when trying to analyze or understand one quantum system in terms of

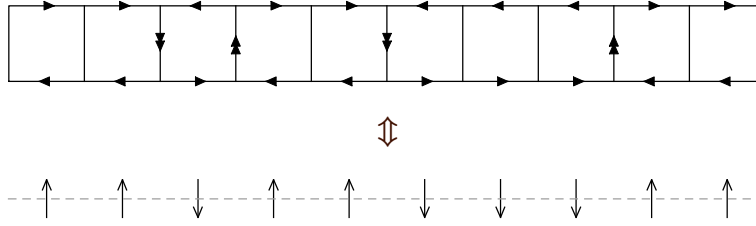


Figure 2.13. We establish a 1-by-1 correspondence between the all states of the QED in the ladder system we presented in this chapter and the 1-dimensional Ising model with a transverse field. The correspondence is showed also for the Hamiltonian of the system, which guarantees that also the dynamics is exactly the same.

another system that is already well-studied or better understood. Sometimes a mapping is referred as a *duality* between two quantum systems.

One common scenario where quantum state mapping is employed is indeed in quantum simulations. By mapping a quantum system of interest to a simpler or more controllable system, one can gain insights into the behavior and properties of the original system (e.g. phase transitions, non-perturbative processes, and so on).

In this section, we want to show an exact mapping between the zero polarization sector of the $(1 + \epsilon) + 1$ ladder QED with no fermions in the QLM formulation with spin representation $\left(\frac{1}{2}, 1\right)$ and the 1-dimensional anti-ferromagnetic Ising model with a transverse field (Fig. 2.13). We will use periodic boundary conditions for convenience, but we could use also open boundary conditions if needed.

2.6.1 The Ising Model with a transverse field

The 1-dimensional (quantum) *Ising Model with a transverse field* is a simplified quantum mechanical model used to describe the behavior of a system composed of interacting spins. Spins can represent the orientation of magnetic moments in a physical material or abstract quantities in other systems. The Hamiltonian of the system is the following:

$$\hat{H} = -J \sum_j \hat{\sigma}_j^z \hat{\sigma}_{j+1}^z - \mu \sum_j \hat{\sigma}_j^x, \quad (2.70)$$

where J is the interaction strength between the spins, μ is the strength of the magnetic field (along the x -axis) and $\hat{\sigma}_i^\alpha$ is the Pauli spin operator (the Pauli 2×2 matrices) for the site j of the Ising chain along the direction $\alpha = x, y, z$. The first term of the Hamiltonian (2.70) represents the interaction energy between neighboring spins, while the second term corresponds to a transverse magnetic field acting on each spin: the interplay between these terms leads to non-trivial quantum effects.

Defining the relative magnetic field strength

$$\lambda \equiv \frac{\mu}{J} \quad (2.71)$$

in the Ising model, there are two phases: a ferromagnetic degenerate “ordered” phase ($\mu < 1$) with z -aligned spins, and a non-degenerate paramagnetic “disordered” phase ($\mu > 1$) with x -aligned spins (in the direction of the field, but classically the spin are disordered). The quantum phase transition occurs at the critical point $\mu = 1$ and it is characterized by abrupt changes in properties like magnetization and correlation length.

2.6.2 Mapping between Hilbert spaces

In section 2.3.1, we actually already implicitly performed mapping between the two Hilbert spaces. Anyway, we do it again specifically for this system in a more intuitive way.

In the assumption of the Gauss’ Law, we saw that we can characterize every spin configuration only considering the top (T) and bottom (B) spins (the semi-plaquette configurations). In particular, there are 4 semi-plaquettes in the $s_x = 1/2$ representation:

$$P_1 = \begin{array}{|c|} \hline \rightarrow \\ \hline \rightarrow \\ \hline \end{array}, \quad P_2 = \begin{array}{|c|} \hline \rightarrow \\ \hline \leftarrow \\ \hline \end{array}, \quad P_3 = \begin{array}{|c|} \hline \leftarrow \\ \hline \rightarrow \\ \hline \end{array}, \quad P_4 = \begin{array}{|c|} \hline \leftarrow \\ \hline \leftarrow \\ \hline \end{array}. \quad (2.72)$$

Given a sequence of these semi-plaquettes, a unique configuration of plaquettes is determined. But now we notice that, given this representation and the Gauss’ Law, we have the following rules, which are a particular case of the general rule (2.17):

- P_1 can only follow P_1 , while P_4 can only follow P_4 ;
- P_2 and P_3 can only follow P_2 or P_3 .

Hence, there are in total $2^L + 2$ combinations, as we already knew from previous sections:

$$\underbrace{\dots P_3 P_2 P_3 P_3 P_2 \dots}_{2^n \text{ configurations}}, \quad \underbrace{\dots P_1 P_1 P_1 P_1 \dots}_{1 \text{ configuration}}, \quad \underbrace{\dots P_4 P_4 P_4 P_4 \dots}_{1 \text{ configuration}} \quad (2.73)$$

However, the configurations $\dots P_1 P_1 P_1 P_1 \dots$ and $\dots P_4 P_4 P_4 P_4 \dots$ are trivial, because they span a 1-dimensional invariant subspace under the action of \hat{H} and \hat{T} , so it can be considered as a separate (polarization) sector of the Hilbert space.

If we consider only all the other elements of the basis, we have exactly 2^L configurations, which is the dimension of the Hilbert space of the Ising model. The mapping is between local state of each site: to map the two Hilbert spaces, we (conventionally) identify the local states of the ladder P_2, P_3 with the eigenstates of $\hat{\sigma}_z$ Ising model $|\uparrow\rangle$ and $|\downarrow\rangle$, which are the local states of the Ising system:

$$P_2 = \begin{array}{|c|} \hline \rightarrow \\ \hline \leftarrow \\ \hline \end{array} \leftrightarrow |\uparrow\rangle, \quad P_3 = \begin{array}{|c|} \hline \leftarrow \\ \hline \rightarrow \\ \hline \end{array} \leftrightarrow |\downarrow\rangle. \quad (2.74)$$

In other words, we identify the top spin $\hat{S}_{\text{T},j}^z$ of the plaquette with the $\hat{\sigma}_j^z$ spin of the correspondent Ising chain site, formally:

$$\hat{S}_{\text{T},j}^z \leftrightarrow \frac{\hat{\sigma}_j^z}{2} = \frac{1}{2} \begin{pmatrix} 1 & 0 \\ 0 & -1 \end{pmatrix}. \quad (2.75)$$

Doing this, we have found an isomorphism (a one-by-one correspondence) between the zero polarization sector of the Hilbert space of the ladder with L plaquettes and the total Hilbert space of the Ising model with L spin- $\frac{1}{2}$ sites:

$$\mathcal{H}_{\text{Ladder}}^{s_{\parallel}=0}(L) \simeq \mathcal{H}_{\text{Ising}}(L). \quad (2.76)$$

As stated before, the mapping between Hilbert spaces is not enough: we need also to prove that this mapping preserves the Hamiltonian (i.e. each couple of corresponding eigenstates of the Hamiltonian have the same energy value).

2.6.3 Electric term \hat{H}_E mapped to the Ising interaction term

In this section we prove that the electric term of the Hamiltonian of the ladder system is mapped in the interaction term of the Ising model. We recall that the electric Hamiltonian term reads (using periodic boundary conditions):

$$\hat{H}^E = \frac{g^2}{2a} \sum_{l=1}^{3L} (\hat{S}_l^z)^2, \quad (2.77)$$

where l runs over all the links of the lattice and $N = 3L$ is the total number of links.

We first decompose the sum of the \hat{S}_l^z squared into summations for top, vertical and bottom links:

$$\sum_{l=1}^{3L} = \sum_{\text{top } l=1}^L + \sum_{\text{vertical } l=1}^L + \sum_{\text{bottom } l=1}^L. \quad (2.78)$$

Using the Gauss' Law, we can write the vertical links as a function of the top horizontal ones:

$$\begin{array}{c} \hat{S}_{\text{T},j}^z \quad \hat{S}_{\text{T},j+1}^z \\ \longrightarrow \quad \longrightarrow \\ \uparrow \hat{S}_{\text{R},j}^z \end{array} \implies \hat{S}_{\text{T},j}^z + \hat{S}_{\text{R},j}^z = \hat{S}_{\text{T},j+1}^z. \quad (2.79)$$

Hence, we can express the summation over the vertical links as

$$\sum_{\text{vertical } l=1}^L (\hat{S}_l^z)^2 = \sum_{j=1}^L (\hat{S}_{\text{T},j+1}^z - \hat{S}_{\text{T},j}^z)^2 = \sum_{j=1}^L (\hat{S}_{\text{T},j+1}^z)^2 + (\hat{S}_{\text{T},j}^z)^2 - 2\hat{S}_{\text{T},j+1}^z \hat{S}_{\text{T},j}^z. \quad (2.80)$$

where j is now a plaquette index. Now, since we choose the $\left(\frac{1}{2}, 1\right)$ representation, we have $(\hat{S}_{\text{T},j}^z)^2 = 1/4$, and using the identification (2.75) we obtain

$$\sum_{\text{vertical } l=1}^L (\hat{S}_l^z)^2 \leftrightarrow \sum_j \frac{1}{4} + \frac{1}{4} - 2 \frac{\hat{\sigma}_{j+1}^z \hat{\sigma}_j^z}{2} = \frac{L}{2} - \frac{1}{2} \sum_j \hat{\sigma}_j^z \hat{\sigma}_{j+1}^z. \quad (2.81)$$

Since we are selecting the zero longitudinal polarization states, from (2.74) it follows that for every plaquette the top and bottom spins are opposite: $\hat{S}_B^z = -\hat{S}_T^z$. Hence, we can write

$$\sum_{\text{top } l=1}^L (\hat{S}_l^z)^2 + \sum_{\text{bottom } l=1}^L (\hat{S}_l^z)^2 = 2 \sum_{\text{top } l=1}^L (\hat{S}_l^z)^2 = 2 \sum_{j=1}^L \frac{1}{4} = \frac{L}{2}. \quad (2.82)$$

Putting all the previous results together, we obtain the following mapping for the electric field term:

$$\hat{H}_E = \frac{g^2}{2a} \sum_l (\hat{S}_l^z)^2 \leftrightarrow \frac{g^2 L}{2a} - \frac{g^2}{4a} \sum_j \hat{\sigma}_j^z \hat{\sigma}_{j+1}^z. \quad (2.83)$$

Aside from a constant term (we keep L , a and g fixed during the system evolution), we see that the electric term is perfectly mapped on the antiferromagnetic^{2.11} Ising interaction term with the following identification between constants:

$$J \leftrightarrow \frac{g^2}{4a}. \quad (2.84)$$

2.6.4 Magnetic term \hat{H}_B mapped to the transverse field term

Now we show an analogous mapping for the magnetic term, which reads

$$\hat{H}^B = \frac{1}{2ag^2} \sum_{j=1}^L \hat{U}_j + \text{H.c.}, \quad \text{with } \hat{U}_j \equiv \hat{S}_{j,B}^+ \hat{S}_{j,R}^+ \hat{S}_{j,T}^- \hat{S}_{j,L}^-. \quad (2.85)$$

To show that the two Hamiltonians are equivalent with respect the previous mapping, it is sufficient to show that the action of each local operator on the local states is the same for the two systems (up to overall constants which can be reabsorbed in the pre-factors). In particular, we will show that the operators \hat{U} and \hat{U}^\dagger acts as the operators $\hat{\sigma}^+$, $\hat{\sigma}^-$ of the Ising model. More precisely the following mapping holds:

$$\hat{U}_j \leftrightarrow 2\hat{\sigma}_j^- = 2 \begin{pmatrix} 0 & 0 \\ 1 & 0 \end{pmatrix}, \quad \hat{U}_j^\dagger \leftrightarrow 2\hat{\sigma}_j^+ = 2 \begin{pmatrix} 0 & 1 \\ 0 & 0 \end{pmatrix}. \quad (2.86)$$

With this identification, the term inside the summation of (2.85) can be mapped as

$$\hat{U}_j + \hat{U}_j^\dagger \leftrightarrow 2\hat{\sigma}_j^x = 2 \begin{pmatrix} 0 & 1 \\ 1 & 0 \end{pmatrix}, \quad (2.87)$$

and this brings to the mapping of the magnetic term to the transverse field term of the Ising model:

$$\hat{H}_B = -\frac{1}{2ag^2} \sum_j \hat{U}_j + \hat{U}_j^\dagger \leftrightarrow -\frac{1}{ag^2} \sum_j \hat{\sigma}_j^x, \quad (2.88)$$

with the following identification of the magnetic field strength constant with respect the lattice constants:

$$\mu \leftrightarrow \frac{1}{ag^2}. \quad (2.89)$$

^{2.11}. It is anti-ferromagnetic because $g^2/4a$ is a positive quantity, as J in the anti-ferromagnetic case.

To prove (2.86), it is sufficient to show the identification between \hat{U} and $\hat{\sigma}^-$ (the other is between the adjoint operators \hat{U}^\dagger and $\hat{\sigma}^+$). Analyzing the action that the operator \hat{U}_j has over the plaquette basis at position j we have:

$$\hat{U} \begin{array}{c} \xrightarrow{s_T^z} \\ \left[\begin{array}{c} \xrightarrow{s_L^z} \\ \xrightarrow{s_B^z} \end{array} \right] \xrightarrow{s_R^z} \end{array} = \begin{cases} \Pi \times \begin{array}{c} \xrightarrow{s_T^z - 1} \\ \left[\begin{array}{c} \xrightarrow{s_L^z - 1} \\ \xrightarrow{s_B^z + 1} \end{array} \right] \xrightarrow{s_R^z + 1} \end{array} & \text{if } \hat{S}^\pm \text{ do not annihilate} \\ & \text{any spin state} \\ 0 & \text{otherwise} \end{cases} \quad (2.90)$$

where Π is the product of the four spin ladder operator pre-factors obtained from the action of \hat{S}^\pm over the four links:

$$\Pi = \sqrt{s_x(s_x + 1) - s_B^z(s_B^z + 1)} \sqrt{s_y(s_y + 1) - s_R^z(s_R^z + 1)} \\ \times \sqrt{s_x(s_x + 1) - s_B^z(s_B^z - 1)} \sqrt{s_y(s_y + 1) - s_R^z(s_R^z - 1)}. \quad (2.91)$$

However, for the particular case of the spin representation $(s_x, s_y) = \left(\frac{1}{2}, 1\right)$ it is straightforward to see that if one computes explicitly (2.91) for any of the possible s^z values, then the value of Π can be only either 0 or 2:

$$\Pi \in \{0, 2\}. \quad (2.92)$$

But if $\Pi = 0$ this means that \hat{S}^\pm is annihilating the state, so $\Pi = 2$. Thus, we can resume the action of the operator \hat{U} over the semi-plaquette basis as

$$\hat{U} \begin{array}{c} \xrightarrow{\quad} \\ \left[\begin{array}{c} \xrightarrow{\quad} \\ \xrightarrow{\quad} \end{array} \right] = 2 \times \begin{array}{c} \xrightarrow{\quad} \\ \left[\begin{array}{c} \xrightarrow{\quad} \\ \xrightarrow{\quad} \end{array} \right] , \quad \hat{U} \begin{array}{c} \xrightarrow{\quad} \\ \left[\begin{array}{c} \xrightarrow{\quad} \\ \xrightarrow{\quad} \end{array} \right] = 0 \end{array} \quad (2.93)$$

which is exactly the same action of the operator $\hat{\sigma}^-$ over the local basis of the Ising model:

$$\hat{\sigma}^- |\uparrow\rangle = |\downarrow\rangle, \quad \hat{\sigma}^- |\downarrow\rangle = |0\rangle. \quad (2.94)$$

2.6.5 Phases and critical point

A summary of the mapping between Hamiltonians shown in the previous sections is the following:

$$\hat{H}_{\text{ladder}} = \underbrace{\frac{g^2}{2a} \sum_l (\hat{S}_l^z)^2}_{\text{electric term}} - \underbrace{\frac{1}{2ag^2} \sum_{\square} (\hat{S}_B^+ \hat{S}_R^+ \hat{S}_T^- \hat{S}_L^- + \text{H.c.})}_{\text{magnetic term}} \\ \Downarrow \qquad \qquad \qquad \Downarrow \qquad \qquad \qquad \Downarrow \quad (2.95) \\ \hat{H}_{\text{Ising}} = - \underbrace{J \sum_i \hat{\sigma}_i^z \hat{\sigma}_{i+1}^z}_{\text{spin interaction}} - \underbrace{\mu \sum_i \hat{\sigma}_i^x}_{\text{transverse field}}$$

The phases of the Ising model are well known, and so are the phases of the ladder lattice system in the spin representation $(\frac{1}{2}, 1)$. In particular, it is known that the phase transition of the Ising model occurs at

$$\lambda \equiv \frac{\mu}{J} = 1 \leftrightarrow g^4 = 4. \quad (2.96)$$

Hence, knowing the properties of the Ising model, we obtain the following phase diagram of the ladder system:

- For $g < \sqrt{2}$ the system is in the *disordered phase*, the ground-state is non-degenerate, the theory is non-confining, and the (massive) quasiparticles are free to move in the lattice;
- For $g > \sqrt{2}$ the system is in the *ordered phase*, the ground-state has a double degeneration, the theory is confining and the quasiparticle cannot propagate freely;
- At $g = \sqrt{2}$, the system undergoes a quantum *phase transition*: the system is at the *critical point*, i.e. in the gapless phase with massless quasiparticles.

The phases above are coherent with what observed computing numerically the dispersion relation of the system (Fig. 2.9 in section 2.5.4). This identification of the phases of the ladder system with the language of Ising model can be very useful, and it will simplify the treatment of this lattice model in the following chapters.

2.6.6 Hints about mapping for higher spin representations

It is worth asking if there exists a natural generalization of this mapping for higher spin representations. The answer is yes, but with some limitations.

First, for higher spin representations there are, in general, more than one nontrivial polarization sectors of the Hilbert space. We saw in section 2.3.3 that using $(n, 2n)$ representation with $n \in \mathbb{N}$ there are $4n + 1$ polarization sectors, where two of them are 1-dimensional trivial sectors. In this particular representation, for any of these polarization sectors, one can find an Hilbert space mapping analogous to (2.74), where in this case the local dimension can be more than 2 (e.g. Ising model with generic spin- s qudits).

However, the problems arise in the Hamiltonian mapping:

- in the electric field term, we cannot set $(\hat{S}_{T,j}^z)^2 = 1/4$, and this brings to non-trivial terms as global summations of spin operators, that cannot be mapped to an Ising model;
- in the magnetic field term, the interaction between the plaquettes in this case are non-local (not 1-plaquette operator); in other words, the condition (2.92) is not satisfied for higher spin representations. This brings to 3-plaquette operators which cannot be mapped in the transverse field term of the Ising model.

For these reasons, each polarization sector has an independent non-trivial phase diagram, and its behavior varying g needs numerical approaches to be understood completely.

It has been shown recently [48], that other models of the pure QED on ladder geometries such the \mathbb{Z}_n lattice gauge theories, are exactly mappable to the so-called *quantum clock model*, which is a generalization of the quantum Ising model.

Chapter 3

Creation of the photonic wave-packets

In chapter 2 we determined many properties of the QLM formulation of the lattice QED on ladder geometries.

In this chapter we provide a model-independent algorithm to create 1-dimensional wave-packets of single quasiparticle states. In particular, to give a concrete numerical example, we will apply this algorithm to the ladder system using the $\left(\frac{1}{2}, 1\right)$ spin representation, which will be our reference toy model from now on.

This approach is classified as *model-independent* because it can, at least in principle, be applied to any 1-dimensional system for which few weak assumptions holds. Indeed, we do not require strong assumptions aside to know the matrix form of the Hamiltonian \hat{H} , which must be invariant under the action of the translation operator \hat{T} .

In particular, the steps of the algorithm are the following:

1. simultaneously diagonalize \hat{H} and \hat{T} , selecting the first Bloch states of the first energy band $|k\rangle$;
2. construct a maximally localized state $|W_j\rangle$ around a plaquette site j , from linear combinations of the $|k\rangle$ multiplied by phases $e^{i\theta_k}$. This step is analogous to the problem of localization of the *Wannier orbital functions* of crystal systems;
3. construct an *excitation operator* \hat{W}_j such that $\hat{W}_j|\Omega\rangle = |W_j\rangle$, i.e. it creates the maximally localized state $|W_j\rangle$ from the vacuum $|\Omega\rangle$. In particular, we want \hat{W}_j to be in a very peculiar form: it must be a linear combinations of compositions of the gauge invariant *plaquette operators* $\hat{U}_j, \hat{U}_j^\dagger$;
4. considering linear combinations of \hat{W}_j to construct a generic wave-packet operator $\hat{\Psi}$ such that $\hat{\Psi}|\Omega\rangle = |\Psi\rangle$, where $|\Psi\rangle$ is the single-particle wave-packet state. In particular, since the \hat{W}_j are written in terms of $\hat{U}_j, \hat{U}_j^\dagger$, also $\hat{\Psi}$ is: this fact is crucial to represent $\hat{\Psi}$ as a Matrix Product Operator (MPO), exploiting the Tensor Network formalism (see chapter 4).

Using the \hat{W}_j , one can create a single-particle wave-packet state of any energy density profile. For instance, one can create a Gaussian wave-packet with a definite momenta k . Furthermore, the fact of having a wave-packet operator $\hat{\Psi}$ instead of a wave-packet state $|\Psi\rangle$ allows to create multi-particle states of spatially separated wave-packets from the vacuum: indeed, if the support of the wave-packet is small enough, it is possible to apply different $\hat{\Psi}$ to the vacuum $|\Omega\rangle$ at different positions to create interesting initial states like a *scattering state*.

3.1 The first energy band states

In this section we analyze the first energy band of the ladder system and we give some properties of these Bloch states. In particular, we concentrate on the $(\frac{1}{2}, 1)$ spin representation for different values of the relative electric field strength coupling g .

3.1.1 First energy band estimation for $(\frac{1}{2}, 1)$ with $g \rightarrow 0$

In the limit $g \rightarrow 0$, we can compute analytically the eigenenergies and the eigenstates of the system in the lowest spin representation. We notice that for very low values of the coupling, only the magnetic term \hat{H}_B survives in the Hamiltonian (2.52):

$$\lim_{g \rightarrow 0} \hat{H} = \hat{H}_B = \sum_j \hat{H}_j^B = -\frac{1}{2ag^2} \sum_j (\hat{U}_j + \hat{U}_j^\dagger). \quad (3.1)$$

Exploiting the mapping with the Ising model described in section 2.6, from the ladder-Ising mapping of states

$$|\begin{array}{|c|} \hline \rightarrow \\ \hline \leftarrow \\ \hline \end{array}\rangle \leftrightarrow |\uparrow\rangle, \quad |\begin{array}{|c|} \hline \leftarrow \\ \hline \rightarrow \\ \hline \end{array}\rangle \leftrightarrow |\downarrow\rangle, \quad (3.2)$$

we had the following mapping between operators

$$\hat{U}_j + \hat{U}_j^\dagger \leftrightarrow 2\hat{\sigma}_j^x. \quad (3.3)$$

Hence, the operators $\hat{U}_j + \hat{U}_j^\dagger$ are *local*, i.e. they acts on a single plaquette (operators of neighboring plaquettes are independent in this particular spin representation). Using a common notation with Ising we define the states

$$|+\rangle \equiv \frac{|\begin{array}{|c|} \hline \rightarrow \\ \hline \leftarrow \\ \hline \end{array}\rangle + |\begin{array}{|c|} \hline \leftarrow \\ \hline \rightarrow \\ \hline \end{array}\rangle}{\sqrt{2}}, \quad |-\rangle \equiv \frac{|\begin{array}{|c|} \hline \rightarrow \\ \hline \leftarrow \\ \hline \end{array}\rangle - |\begin{array}{|c|} \hline \leftarrow \\ \hline \rightarrow \\ \hline \end{array}\rangle}{\sqrt{2}}. \quad (3.4)$$

From the Ising model in the regime with infinite transverse field (the disordered phase, all the spins aligned to the magnetic field), we get that the ground-state of the system is a separable state which can be written as

$$|\Omega\rangle = |+\rangle \otimes |+\rangle \otimes \dots \otimes |+\rangle. \quad (3.5)$$

Thus, the energy of the ground-state is

$$\mathcal{E}_0(g \rightarrow 0) \equiv \langle \Omega | \hat{H} | \Omega \rangle = -\frac{1}{2ag^2} \sum_{j=1}^L \langle + | 2\hat{\sigma}_j^x | + \rangle = -\frac{L}{ag^2}. \quad (3.6)$$

which is a coherent result with the first dispersion relation graph of Fig. 2.9.

Now, we define the *localized state* in a plaquette of site j as

$$|j\rangle \equiv |+\rangle \otimes \dots \otimes |+\rangle \otimes \underbrace{|-\rangle}_{j^{\text{th}} \text{ site}} \otimes |+\rangle \dots \otimes |+\rangle. \quad (3.7)$$

The states $|j\rangle$ are indeed eigenstates of the Hamiltonian with energy:

$$\mathcal{E}_1(g \rightarrow 0) \equiv \langle j | \hat{H} | j \rangle = -\frac{1}{2ag^2} \left(\langle - | 2\hat{\sigma}_j^x | - \rangle + \sum_{j=1}^{L-1} \langle + | 2\hat{\sigma}_j^x | + \rangle \right) = -\frac{L-2}{ag^2}. \quad (3.8)$$

However, $|j\rangle$ are not eigenstates of the translation operator \hat{T} because obviously

$$\hat{T}|j\rangle = |j+1\rangle. \quad (3.9)$$

We notice that instead the states defined as

$$|k\rangle \equiv \sum_j e^{ikj} |j\rangle \quad (3.10)$$

are both eigenstates of \hat{H} and \hat{T} . Hence, the states (3.10) are exactly the Bloch states of the first energy band, i.e. the single quasiparticle states, in the limit $g \rightarrow 0$.

The energy difference between the first band and the ground-state in this limit is

$$\mathcal{E}_1(g \rightarrow 0) - \mathcal{E}_0(g \rightarrow 0) = -\frac{L-2}{ag^2} + \frac{L}{ag^2} = \frac{2}{ag^2}. \quad (3.11)$$

Since the first energy band is *flat* (no propagation of quasiparticles), the quantity (3.11) corresponds also to the energy gap Δ_0 of the system. We notice that for $g \rightarrow 0$ this gap is also the energy separation between two any adjacent many-body energy bands, namely

$$\Delta_0 = \mathcal{E}_n - \mathcal{E}_{n-1}. \quad (3.12)$$

3.1.2 Perturbative correction of the first energy band

The unperturbed ($g \rightarrow 0$) and the perturbation Hamiltonian are:

$$\hat{H}_0 = -\frac{1}{2ag^2} \sum_j \hat{U}_j + \hat{U}_j^\dagger, \quad \hat{V} = \frac{g^2}{2a} \sum_j \hat{E}_j. \quad (3.13)$$

The local plaquette states which are diagonal in the electric field, while the states $|\pm\rangle$ are *diagonal* in the *magnetic* basis, because of the Ising mapping:

$$(\hat{U} + \hat{U}^\dagger)|+\rangle = |+\rangle, \quad (\hat{U} + \hat{U}^\dagger)|-\rangle = -|-\rangle. \quad (3.14)$$

This means that the unperturbed ground-state is (using the notation of perturbation theory)

$$|\mathcal{E}_0^{(0)}\rangle = |+\rangle \otimes |+\rangle \otimes \dots \otimes |+\rangle. \quad (3.15)$$

Since \hat{V} is mapped to the hopping of $\hat{\sigma}_j^z \hat{\sigma}_{j+1}^z$ in Ising, we notice that the perturbative correction of the ground-state is at *second order* because it is vanishing at first order:

$$\langle \mathcal{E}_0^{(0)} | \hat{V} | \mathcal{E}_0^{(0)} \rangle = 0. \quad (3.16)$$

Using perturbation theory, we want to show that the perturbative correction of the dispersion relation for the first band is the tight binding cosine.

We want to compute the energy correction of the first excitation band, whose perturbation correction is at *first order*. Let's consider the following (degenerate, real space) *unperturbed first-excited* states (actually they constitutes the flat band of the localized Wannier functions for $g \rightarrow 0$):

$$|j\rangle = |+\rangle \otimes \dots \otimes |+\rangle \otimes \underbrace{|-\rangle}_{j\text{-th}} \otimes |+\rangle \dots \otimes |+\rangle. \quad (3.17)$$

The effective Hamiltonian at first order for the states $|j\rangle$ is

$$\hat{H}^{(1)} = \hat{P} \hat{V} \hat{P}. \quad (3.18)$$

Restricting to the L -dimensional subspace of the states $|j\rangle$ (so that the operators now are $L \times L$ matrices) and considering the Ising mapping we have:

$$\hat{P}_{ij} = \delta_{ij}, \quad \hat{V}_{ij} = -\frac{g^2}{4a} \sum_l \langle i | \hat{\sigma}_l^z \hat{\sigma}_{l+1}^z | j \rangle = -\frac{g^2}{4a} (\delta_{i,j-1} + \delta_{i,j+1}) \quad (3.19)$$

Here, we notice that $\delta_{i,j-1}$ and $\delta_{i,j+1}$ are the lower and upper diagonal matrix filled with 1, so they are the translation operator restricted to the subspace of $|j\rangle$. Hence, we can write \hat{V} in this subspace as

$$\hat{V} = -\frac{g^2}{4a} (\hat{T}^\dagger + \hat{T}). \quad (3.20)$$

Since $|k\rangle$ are eigenstates of \hat{T} with eigenvalues e^{iak} , we can compute the first order correction as a function of the momentum as

$$\mathcal{E}_1^{(1)} = \langle k | \hat{H}^{(1)} | k \rangle = -\frac{g^2}{4a} \langle k | (\hat{T}^\dagger + \hat{T}) | k \rangle = -\frac{g^2}{2a} \frac{e^{iak} + e^{-iak}}{2} = -\frac{g^2}{2a} \cos(ka). \quad (3.21)$$

3.1.3 Simultaneous diagonalization of \hat{H} and \hat{T}

If $g \neq 0$, then the simultaneous diagonalization of \hat{H} and \hat{T} is non-trivial, and numerical methods are needed to find the Bloch states.

From the spectral theorem, diagonalizing \hat{H} and \hat{T} simultaneously can be achieved only if the two operators commute. Indeed we need to require that $[\hat{H}, \hat{T}] = 0$, which is equivalent to the condition of *translational invariance* of the Hamiltonian (which is true for our theory).

There are many different methods that can be employed to simultaneously diagonalize two commuting operators. A standard method provides a block-diagonal structure for both \hat{H} and \hat{T} , where each block corresponds to a set of degenerate eigenvectors.

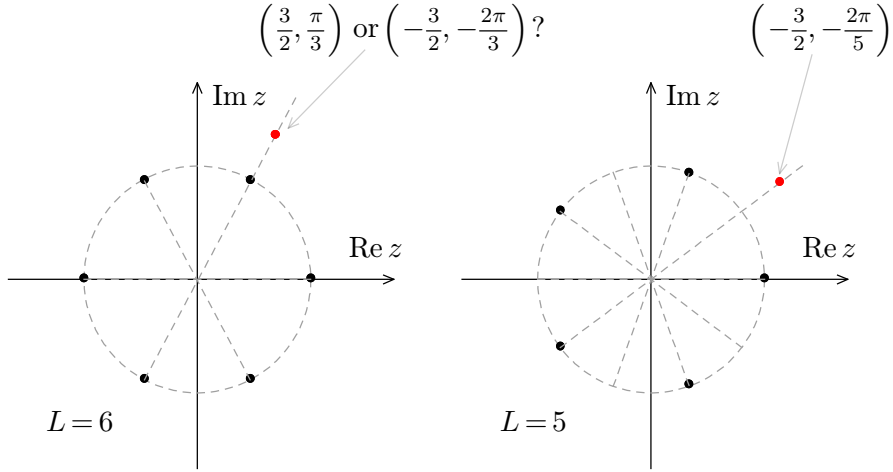


Figure 3.1. For an even number of plaquettes (left) there is an ambiguity of the energy \mathcal{E} (the real factor) and momentum k (the complex phase) if a point on the complex plane is given. This does not happen for an odd number of plaquettes (right).

However, the method used here to diagonalize the operators with a common basis is very general and it is one of the simplest to traduce into code. It consists in *diagonalizing the matrix product $\hat{H}\hat{T}$* . This method works for the following statement:

$$\begin{cases} \hat{H}|\mathcal{E}, k\rangle = \mathcal{E}|\mathcal{E}, k\rangle \\ \hat{T}|\mathcal{E}, k\rangle = e^{ik}|\mathcal{E}, k\rangle \end{cases} \iff \hat{H}\hat{T}|\mathcal{E}, k\rangle = \mathcal{E}e^{ik}|\mathcal{E}, k\rangle. \quad (3.22)$$

If $|\mathcal{E}, k\rangle$ is an eigenvector of both \hat{H} and \hat{T} , with eigenvalues \mathcal{E} and e^{ik} respectively, then it is also an eigenvector of $\hat{H}\hat{T}$ with eigenvalue $\mathcal{E}e^{ik}$. Hence, all the common eigenvectors are also eigenvectors of the matrix product. But since (\hat{H}, \hat{T}) is a complete set of commuting observables, then the number of common non-degenerate eigenvectors $|\mathcal{E}, k\rangle$ must be the dimension of \hat{H} (and \hat{T}). Since the maximum number of non-degenerate eigenvectors of $\hat{H}\hat{T}$ is the dimension of $\hat{H}\hat{T}$, which is the dimension of \hat{H} , it follows immediately that all and only the eigenvalues of $\hat{H}\hat{T}$ are the common eigenvectors of the two matrices separately.

As a result, if $|z\rangle$ and z are the eigenstates and eigenvalues of $\hat{H}\hat{T}$ respectively, we can find the energy and the momentum of the eigenstates simply taking the modulus and the argument of z :

$$\hat{H}\hat{T}|z\rangle = z|z\rangle, \quad \mathcal{E} = |z|, \quad k = \arg z. \quad (3.23)$$

Here there is just a problem when L is *even*: indeed, in this case there is an ambiguity to \mathcal{E} and k due to the fact that the points $\mathcal{E}e^{ik}$ and $-\mathcal{E}e^{i(k+\pi)}$ are identified as the same in the complex plane; this means that the couple of eigenvalues (\mathcal{E}, k) , is not distinguishable from the couple $(-\mathcal{E}, k + \pi)$ using the method of the matrix product.

However, due to the range of the possible values the Bloch wave-vector k can assume, this is not an issue if the number L of sites of the system is *odd* (see Fig. 3.1). This is the main reason why we will mostly consider the cases of L *odd*.

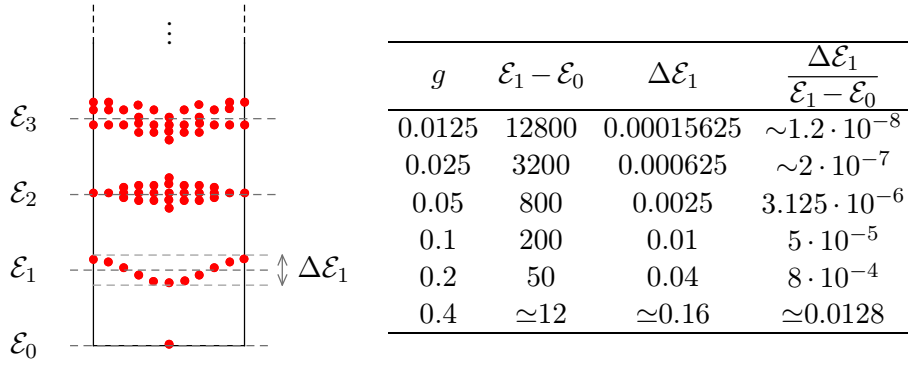


Table 3.1. Numerical estimation of the first energy band separation $\mathcal{E}_1 - \mathcal{E}_0$ and of the first energy bandwidth $\Delta\mathcal{E}_1$. We can clearly see that (3.26) is the first order expansion of this dependence.

3.1.4 Energy estimations of the first band for low g

Exploiting the exact diagonalization technique described in section 3.1.3, we can compute exactly all the eigenenergies of the system for $g \neq 0$. However, we are particularly interested in the thermodynamic and continuum limit of the theory ($L \rightarrow \infty$, $a \rightarrow 0$).

For lower spacetime dimensions than $3 + 1$, a dimensional analysis suggest that $g \rightarrow 0$ for $a \rightarrow 0$, without considering quantum corrections^{3.1}. Hence, the case of low coupling $g \sim 0$ is the nearest to the continuum for this quasi 1-dimensional ladder system.

Since the perturbative expansion parameter is g^4 , as discussed at the end of section 1.2.2, from perturbation theory we expect small multiplicative corrections of the form $(1 + \mathcal{O}(g^4))$ to the energy estimations (3.6) and (3.11) of the case $g \rightarrow 0$:

$$\mathcal{E}_0 = -\frac{L}{ag^2} \cdot (1 + \mathcal{O}(g^4)), \quad \mathcal{E}_n - \mathcal{E}_{n+1} = \frac{2}{ag^2} \cdot (1 + \mathcal{O}(g^4)). \quad (3.24)$$

Table 3.1 shows some numerical estimations of $\mathcal{E}_1 - \mathcal{E}_0$ for finite but low couplings ($g \neq 0$).

Furthermore, in this regime, another important fact happens: the first band is no more flat, and it acquires the typical cosine shape of the nearest neighbor tight binding dispersion relation (see section 2.5.3):

$$\mathcal{E}(k) = \mathcal{E}_1 - \frac{\Delta\mathcal{E}_1}{2} \cos(ak). \quad (3.25)$$

In particular, numerically one can check (see Tab. 3.1) that the bandwidth $\Delta\mathcal{E}_1$ of this cosine has the following asymptotic behavior for small values of g :

$$\Delta\mathcal{E}_1 = \frac{g^2}{a} \cdot (1 + \mathcal{O}(g^4)), \quad (3.26)$$

which is consistent with the fact that $\Delta\mathcal{E}_1 \rightarrow 0$ (flat band) for $g \rightarrow 0$.

^{3.1} In general, due to the running of the coupling, the dependence of g with respect a can be modified.

Using these estimations, we can also determine which are the values of g for which the tight binding condition holds:

$$\frac{\Delta\mathcal{E}_n}{\mathcal{E}_n - \mathcal{E}_{n+1}} \lesssim \frac{1}{2} \quad \rightarrow \quad g \lesssim 1. \quad (3.27)$$

For higher values of g , the first band is no more isolated. An interesting regime is the critical point at $g = \sqrt{2}$, where the quasiparticles representing 1-dimensional photons become massless.

3.1.5 Symmetry properties of the Bloch vectors

The study of the symmetry properties of the Bloch vectors can be useful to reduce the computational complexity of some operations.

For a symmetry operator which commutes with both \hat{H} and \hat{T} (e.g. the flip operator \hat{F}), the Bloch vectors $|\mathcal{E}, k\rangle$ are also eigenstates of that symmetry operator.

The y -axis reflection operator \hat{R}_j with respect a site j requires its own discussion, since its commutation relation (2.49) with \hat{T} is non-trivial (see section 2.4.2). Since the reflection operator \hat{R}_j commutes with \hat{H} we have that^{3.2} $\hat{R}|\mathcal{E}, k\rangle$ is an eigenstate of \hat{H} with eigenvalue \mathcal{E} :

$$\hat{H}\hat{R}|\mathcal{E}, k\rangle = \hat{R}\hat{H}|\mathcal{E}, k\rangle = \mathcal{E}\hat{R}|\mathcal{E}, k\rangle. \quad (3.28)$$

From the commutation relation (2.49) it follows instead that $\hat{R}|\mathcal{E}, k\rangle$ is an eigenstate of \hat{T} with wave-vector $-k$:

$$\hat{T}\hat{R}|\mathcal{E}, k\rangle = \hat{R}\hat{T}^\dagger|\mathcal{E}, k\rangle = e^{-ik}\hat{R}|\mathcal{E}, k\rangle. \quad (3.29)$$

Hence, applying the reflection operator \hat{R} to an eigenstate $|\mathcal{E}, k\rangle$ we obtain the associated eigenstate with same energy and opposite momentum:

$$\hat{R}|\mathcal{E}, k\rangle = r_{\mathcal{E}, k}|\mathcal{E}, -k\rangle, \quad r_{\mathcal{E}, k} \in \mathbb{C}, \quad (3.30)$$

where $r_{\mathcal{E}, k}$ is a generic complex coefficient whose properties are determined in the following. The value of the r_k coefficients are simply computable as^{3.3}

$$\langle -k|\hat{R}|k\rangle = \langle -k|r_k|-k\rangle = r_k. \quad (3.31)$$

To determine some properties of the r_k coefficients, we first notice from the normalization of the eigenstates that r_k has modulus one:

$$|r_k|^2 = |r_k|^2 \langle -k|-k\rangle = \langle k|\hat{R}^\dagger\hat{R}|k\rangle = \langle k|\mathbb{I}|k\rangle = 1, \quad (3.32)$$

3.2. From now on we will omit the j index, considering a fixed site j .

3.3. For the next steps, we will omit the \mathcal{E} index because it is not relevant for computations.

and so r_k can be written as a complex phase:

$$r_k = e^{i\varphi_k}, \quad \varphi_k \in \mathbb{R}. \quad (3.33)$$

Hence, rewriting (3.30) using (3.33) we obtain

$$\hat{R}|k\rangle = e^{i\varphi_k}|-k\rangle. \quad (3.34)$$

Now, applying \hat{R} to both sides of the previous equation and using the property $\hat{R}^2 = \mathbb{I}$ we obtain

$$|k\rangle = e^{i\varphi_k} e^{i\varphi_{-k}}|k\rangle \quad (3.35)$$

from which we have that $e^{i\varphi_k} e^{i\varphi_{-k}} = 1$, which brings to the condition on the phases

$$\varphi_{-k} = -\varphi_k + 2n\pi, \quad n \in \mathbb{N}, \quad (3.36)$$

For the particular case $k=0$ it holds $\varphi_0 = n\pi$ with $n \in \mathbb{N}$, and this means that for the states of vanishing momenta we obtain

$$r_0 = e^{i\varphi_0} = e^{i\pi n} = \pm 1. \quad (3.37)$$

Thus, these states are also eigenstates of the reflection operator, and its eigenvalue $r_0 = \pm 1$ is defined as the *parity* of the $k=0$ Bloch functions:

$$\hat{R}|k=0\rangle = r_0|k=0\rangle, \quad r_0 = \pm 1. \quad (3.38)$$

3.2 Maximally localized Wannier States

The Bloch functions are not localized in real space, and their extended structure can make them useless in some situations.

The *Wannier functions* [53] are a set of wave-functions usually employed in solid-state physics to describe the electronic states of a crystal. They are named after the physicist Gregory Wannier, who introduced them in 1937. These functions offer an alternative representation of the electronic band structure, but they can be used in principle in the context of any many-body system.

The Wannier functions are constructed to be *maximally localized* in real space [45, 46]. This means that they have a spatial extent limited to a few sites of the lattice and are well-localized around a specific site. Being linear combinations of Bloch functions, the Wannier functions represents a basis of the same Hilbert space spanned by the original Bloch functions.

These kind of functions are needed in our context as building blocks to construct the single particle wave-packet: in analogy with the Dirac delta function, with linear combinations of enough localized states we can construct any single-particle state.

3.2.1 Symmetrization of the Bloch states

A fundamental step for the localization of the Wannier functions is the so called symmetrization of the Bloch states. This allows to simplify the minimization process, writing a simpler spread functional (see section 3.2.3). In particular, we want to redefine the Bloch states with a different global phase:

$$|k\rangle_s = \alpha_k |k\rangle, \quad |\alpha_k|^2 = 1, \quad (3.39)$$

in such a way that all the $|k\rangle_s$ for $k \neq 0$ are symmetric/antisymmetric under the action of the reflection operator:

$$\hat{R}|k\rangle_s = r_0 |-k\rangle_s. \quad (3.40)$$

Using the definition (3.39) of $|k\rangle_s$, the condition (3.40) becomes

$$\hat{R}\alpha_k |k\rangle = r_0 \alpha_{-k} |-k\rangle, \quad (3.41)$$

and applying \hat{R} to the state $|k\rangle$ in the left-hand side of (3.41) we obtain

$$\alpha_k r_k |-k\rangle = r_0 \alpha_{-k} |-k\rangle. \quad (3.42)$$

Hence, we obtain the following condition

$$\alpha_k = \frac{r_0}{r_k} \alpha_{-k}, \quad (3.43)$$

The condition (3.43) indeed a sufficient for (3.40) because imposing it indeed we have

$$\hat{R}|k\rangle_s = \alpha_k \hat{R}|k\rangle = \alpha_k r_k |-k\rangle = \frac{r_0}{r_k} \alpha_{-k} r_k |-k\rangle = r_0 \alpha_{-k} |-k\rangle = r_0 |-k\rangle_s.$$

For instance, to satisfy (3.43) we can set

$$\alpha_k = \begin{cases} 1 & k \leq 0 \\ r_0/r_k & k > 0 \end{cases},$$

and so we define the *(anti)symmetrized Bloch states*

$$|k\rangle_s = \begin{cases} |k\rangle & k \leq 0 \\ \frac{r_0}{r_k} |k\rangle & k > 0 \end{cases}.$$

3.2.2 Wannier Functions: definition and properties

Let $\{\theta_k\}$ be L real phases, which we will denote as a vector with real entries $\boldsymbol{\theta} \in \mathbb{R}^L$. We know that a generic one-particle state can be taken as a linear combination of the Bloch states $|k\rangle$ of the first excitation band. Imposing the coefficients to be phases $e^{i\theta_k}$, we call such a linear combination a Wannier function or *Wannier state*

$$|W_{\boldsymbol{\theta}}\rangle = \frac{1}{\sqrt{L}} \sum_k e^{i\theta_k} |k\rangle. \quad (3.44)$$

It is simple to show that the sets of states

$$|W_{\boldsymbol{\theta}}\rangle, \hat{T}|W_{\boldsymbol{\theta}}\rangle, \hat{T}^2|W_{\boldsymbol{\theta}}\rangle, \dots, \hat{T}^{L-1}|W_{\boldsymbol{\theta}}\rangle \quad (3.45)$$

forms an alternative orthonormal basis with respect that of the Bloch states. Indeed, the set of Wannier states $\hat{T}^j|W_\theta\rangle$ are *orthonormal*:

$$\begin{aligned}
\langle W_\theta|\hat{T}^{-j}\hat{T}^{j'}|W_\theta\rangle &= \frac{1}{\sqrt{L}} \sum_k e^{-i\theta_k} \langle k|e^{-ikj} \frac{1}{\sqrt{L}} \sum_{k'} e^{i\theta_{k'}} e^{ik'j'} |k'\rangle \\
&= \frac{1}{L} \sum_{k,k'} e^{-i\theta_k} e^{i\theta_{k'}} e^{-ikj} e^{ik'j'} \langle k|k'\rangle \\
&= \frac{1}{L} \sum_{k,k'} e^{-i(\theta_{k'}-\theta_k)} e^{-ikj} e^{ik'j'} \delta_{k,k'} \\
&= \frac{1}{L} \sum_k e^{-i(\theta_k-\theta_k)} e^{ik(j'-j)} \\
&= \frac{1}{L} \sum_k e^{ik(j'-j)} \\
&= \delta_{jj'}.
\end{aligned}$$

In particular, one can vary the values of the phases until $|W_\theta\rangle$ has some interesting properties, as the maximal localization around a site [45, 46].

Notice that, as we did in the previous section, we changed the phase of $|k\rangle$ such that

$$\hat{R}|k\rangle = r_0|-k\rangle, \quad r_0 = \pm 1. \quad (3.46)$$

Now, if we impose the Wannier function to be (anti)symmetric

$$\hat{R}|W_\theta\rangle = r_0|W_\theta\rangle, \quad (3.47)$$

expanding the Wannier function with (3.44) and make \hat{R} acting to the Bloch vectors the previous equation becomes

$$\frac{r_0}{\sqrt{L}} \sum_k e^{i\theta_{-k}} |k\rangle = \frac{r_0}{\sqrt{L}} \sum_k e^{i\theta_k} |k\rangle, \quad (3.48)$$

where in the first summation we have changed the index as $k \rightarrow -k$. Hence, we obtain that a sufficient condition for (3.47) is

$$\theta_k = \theta_{-k}. \quad (3.49)$$

So we can halve (apart from $k = 0$) the number of degrees of freedom if we consider *(anti)symmetrized* Wannier functions.

3.2.3 The energy spread functional

In the previous chapter, we denoted with \hat{H}_j the local Hamiltonian associated to the j -th plaquette. Given a generic state $|\phi\rangle$, we define the *local energy functional* as the expectation value of the local Hamiltonian computed in the state $|\phi\rangle$, subtracting that of the ground-state:

$$\mathcal{E}_j[\phi] \equiv \langle \phi|\hat{H}_j|\phi\rangle - \langle \Omega|\hat{H}_j|\Omega\rangle. \quad (3.50)$$

Since the ground-state is a $k = 0$ state, it is translationally invariant, or $\hat{T}|\Omega\rangle = |\Omega\rangle$, from which it immediately follows that

$$\langle \Omega|\hat{H}_j|\Omega\rangle = \langle \Omega|\hat{H}_{j'}|\Omega\rangle \quad \forall j', \quad (3.51)$$

and so the energy per plaquette of the ground state is equally distributed:

$$\langle \Omega | \hat{H}_j | \Omega \rangle = \frac{\langle \Omega | \hat{H} | \Omega \rangle}{L} = \frac{\mathcal{E}_0}{L}. \quad (3.52)$$

We now define the *spread energy functional* of a state $|\phi\rangle$ as

$$\sigma^2[\phi] \equiv \frac{\sum_j \chi_j^2 \mathcal{E}_j[\phi]}{\sum_j \mathcal{E}_j[\phi]} - \left(\frac{\sum_j \chi_j \mathcal{E}_j[\phi]}{\sum_j \mathcal{E}_j[\phi]} \right)^2, \quad (3.53)$$

where the index j refers to the position with respect the central plaquette, and χ_j is a kernel function which represents the *distance* from the position j_c , e.g. the central plaquette. The function χ_j must satisfy the following properties:

- it must be *monotonic* in j ;
- it must be *odd* with respect the inversion of the central plaquette position:

$$\chi_{j_c-j} = -\chi_j. \quad (3.54)$$

For instance, as a choice for the function χ we can take

$$\chi_j = j - j_c \quad \text{or} \quad \chi_j = \sin\left(\frac{\pi}{L}(j - j_c)\right), \quad (3.55)$$

where in this case the plaquette index ranges as $j = 0, \dots, L$, and we defined the central plaquette position as

$$j_c \equiv \frac{L+1}{2}. \quad (3.56)$$

The reflection operator with respect the central plaquette j_c acts on the local Hamiltonian, by definition, as

$$\hat{R}_{j_c} \hat{H}_j \hat{R}_{j_c} = \hat{H}_{j_c-j} \quad (\hat{R} = \hat{R}^\dagger). \quad (3.57)$$

If the Wannier function is symmetrized as (3.47) then we have

$$\langle W_\theta | \hat{H}_{j_c-j} | W_\theta \rangle = \langle W_\theta | \hat{R}_{j_c} \hat{H}_j \hat{R}_{j_c} | W_\theta \rangle = \underbrace{r_0^2}_{=1} \langle W_\theta | \hat{H}_j | W_\theta \rangle, \quad (3.58)$$

and from this follows that the second term of the right-hand side of (3.53) is always identically vanishing:

$$\begin{aligned} \sum_{j=1}^L \chi_j \mathcal{E}_j[W_\theta] &= \sum_{j=1}^L \chi_j \left[\langle W_\theta | \hat{H}_j | W_\theta \rangle - \underbrace{\langle \Omega | \hat{H}_j | \Omega \rangle}_{\mathcal{E}_0/L} \right] \\ &= \sum_{j=1}^L \chi_j \langle W_\theta | \hat{H}_j | W_\theta \rangle - \underbrace{\frac{\mathcal{E}_0}{L} \sum_{j=1}^L \chi_j}_{=0} \\ &= \sum_{j>j_c} \chi_j \langle W_\theta | \hat{H}_j | W_\theta \rangle + \sum_{j<j_c} \chi_j \langle W_\theta | \hat{H}_j | W_\theta \rangle \\ &= 0. \end{aligned}$$

The denominator of the first term of (3.53) is instead a constant term:

$$\begin{aligned}
\sum_{j=1}^L \mathcal{E}_j[W(\boldsymbol{\theta})] &= \sum_{j=1}^L \left[\langle W_{\boldsymbol{\theta}} | \hat{H}_j | W_{\boldsymbol{\theta}} \rangle - \frac{\mathcal{E}_{\Omega}}{L} \right] \\
&= -\mathcal{E}_{\Omega} + \sum_{j=1}^L \langle W_{\boldsymbol{\theta}} | \hat{H}_j | W_{\boldsymbol{\theta}} \rangle \\
&= -\mathcal{E}_{\Omega} + \sum_{j=1}^L \frac{1}{\sqrt{L}} \sum_k e^{-i\theta_k} \langle k | \hat{H}_j \frac{1}{\sqrt{L}} \sum_{k'} e^{i\theta_{k'}} | k' \rangle \\
&= -\mathcal{E}_{\Omega} + \frac{1}{L} \sum_{k,k'} e^{-i\theta_k} e^{i\theta_{k'}} \langle k | \sum_{j=1}^L \hat{H}_j | k' \rangle \\
&= -\mathcal{E}_{\Omega} + \frac{1}{L} \sum_{k,k'} e^{i(\theta_{k'} - \theta_k)} \mathcal{E}_k \delta_{kk'} \\
&= -\mathcal{E}_{\Omega} + \frac{1}{L} \sum_k \mathcal{E}_k \\
&= \mathcal{E}_{\Delta},
\end{aligned}$$

where we defined \mathcal{E}_{Δ} as the difference between the average of the energies of the first band and the ground-state energy:

$$\mathcal{E}_{\Delta} \equiv \left(\frac{1}{L} \sum_k \mathcal{E}_k \right) - \mathcal{E}_{\Omega}. \quad (3.59)$$

Hence, we can write the functional (3.53) in the simpler form

$$\sigma^2[\phi] \equiv \frac{1}{\mathcal{E}_{\Delta}} \sum_{j=1}^L \chi_j^2 \mathcal{E}_j[\phi]. \quad (3.60)$$

Applying the functional (3.60) to the Wannier state (3.44) we obtain

$$\sigma^2[W_{\boldsymbol{\theta}}] = \frac{1}{\mathcal{E}_{\Delta}} \sum_{j=1}^L \chi_j^2 \langle W_{\boldsymbol{\theta}} | \hat{H}_j | W_{\boldsymbol{\theta}} \rangle - \frac{1}{\mathcal{E}_{\Delta}} \sum_{j=1}^L \chi_j^2 \langle \Omega | \hat{H}_j | \Omega \rangle, \quad (3.61)$$

where the second term of the right-hand side of the previous equation, due to (3.52), is a constant shift of the functional:

$$\frac{1}{\mathcal{E}_{\Delta}} \sum_{j=1}^L \chi_j^2 \langle \Omega | \hat{H}_j | \Omega \rangle = \frac{\mathcal{E}_{\Omega}}{L \mathcal{E}_{\Delta}} \sum_{j=1}^L \chi_j^2. \quad (3.62)$$

Hence, to find the minimum of (3.61) we can just minimize the following functional

$$f(\boldsymbol{\theta}) = \sum_{j=1}^L \chi_j^2 \langle W_{\boldsymbol{\theta}} | \hat{H}_j | W_{\boldsymbol{\theta}} \rangle. \quad (3.63)$$

3.2.4 Minimizing the functional $f(\boldsymbol{\theta})$

We can expand (3.63) using the definition (3.44) of the Wannier states:

$$\begin{aligned}
f(\boldsymbol{\theta}) &\equiv \sum_{j=1}^L \chi_j^2 \langle W_{\boldsymbol{\theta}} | \hat{H}_j | W_{\boldsymbol{\theta}} \rangle \\
&= \sum_{j=1}^L \chi_j^2 \frac{1}{\sqrt{L}} \sum_k e^{-i\theta_k} \langle k | \left(\frac{1}{L} \sum_j j^2 \hat{H}_j \right) \frac{1}{\sqrt{L}} \sum_{k'} e^{i\theta_{k'}} | k' \rangle \\
&= \sum_{k,k'} e^{-i\theta_k} e^{i\theta_{k'}} \frac{1}{L} \sum_{j=1}^L \chi_j^2 \langle k | \hat{H}_j | k' \rangle.
\end{aligned}$$

Now, defining the following matrix elements

$$\Lambda_{kk'} \equiv \frac{1}{L} \sum_{j=1}^L \chi_j^2 \langle k | \hat{H}_j | k' \rangle, \quad (3.64)$$

which are fixed^{3,4} complex parameters, we can write the functional f in a simpler way:

$$f(\boldsymbol{\theta}) = \sum_{k,k'} \Lambda_{kk'} e^{i(\theta_{k'} - \theta_k)}. \quad (3.65)$$

This functional is defined over the space of the real phases parameters θ_k , so it is defined on an L -dimensional flat torus \mathbb{T}^L . We notice that f is an eigenfunction of the Laplace operator ∇^2 defined in the domain \mathbb{T}^L , with eigenvalue $\lambda = 2$:

$$\begin{aligned}
\nabla^2 f &= - \sum_h \partial_h \partial_h f(\boldsymbol{\theta}) \\
&= - \sum_{h,k,k'} \Lambda_{kk'} \partial_h \partial_h (e^{-i\theta_k} e^{i\theta_{k'}}) \\
&= \sum_{h,k,k'} \Lambda_{kk'} (\delta_{hk} \delta_{hk} - \delta_{hk} \delta_{hk'} - \delta_{hk'} \delta_{hk} + \delta_{hk'} \delta_{hk'}) e^{-i\theta_k} e^{i\theta_{k'}} \\
&= \sum_{k,k'} \Lambda_{kk'} (2 + \delta_{kk'} - \delta_{k'k}) e^{-i\theta_k} e^{i\theta_{k'}} \\
&= 2 \sum_{k,k'} \Lambda_{kk'} e^{-i\theta_k} e^{i\theta_{k'}} \\
&= 2f
\end{aligned}$$

This means that the function f has a simple structure: in a flat space (like in the L -torus), the eigenfunctions of the Laplacian can be written as products of sinusoidal functions using separation of variables. Numerically, we notice that every minimizing algorithm for f (e.g. steepest descent, Nelder-Mead and so on) never fails for this function in this space (for any value of the initial $\boldsymbol{\theta}$). This is an indication that the structure of f probably consists in just two nodal sets and just one value of the local minima (the Wannier in a site j) and one value of the local maxima (the Wannier in the opposite site of the system, which is the most distant from j with periodic boundary conditions).

^{3,4} In the context of this minimization problem, we always fix L , a and g .

3.2.5 Optimize the computation of $\Lambda_{kk'}$

Calculating numerically the coefficients (3.64) can be computationally challenging if done in that form. In this section we see a way to optimize the computation of these coefficients.

Since $\hat{T}^n|k\rangle = e^{ikn}|k\rangle$, we can exploit the translational symmetry of the local Hamiltonians:

$$\hat{H}_j = \hat{T}^j \hat{H}_0 \hat{T}^{j\dagger}$$

where \hat{H}_0 is the local Hamiltonian of the first plaquette. Hence, we can recast the Λ matrix as

$$\begin{aligned} \Lambda_{kk'} &= \frac{1}{L} \sum_{j=1}^L \chi_j^2 \langle k | \hat{H}_j | k' \rangle \\ &= \frac{1}{L} \sum_{j=1}^L \chi_j^2 \langle k | \hat{T}^j \hat{H}_0 \hat{T}^{j\dagger} | k' \rangle \\ &= \langle k | \hat{H}_0 | k' \rangle \frac{1}{L} \sum_{j=1}^L \chi_j^2 e^{ikj} e^{-ik'j} \\ &= \langle k | \hat{H}_0 | k' \rangle \tilde{\chi}_{k-k'}^2. \end{aligned}$$

Thus, we can compute the matrix elements of just one plaquette Hamiltonian \hat{H}_0 (which is way simpler than for the whole \hat{H}), and $\tilde{\chi}^2$ is the *inverse discrete Fourier transform* of the square distance function χ^2 :

$$\tilde{\chi}_k^2 \equiv \frac{1}{L} \sum_{j=1}^L e^{ikj} \chi_j^2.$$

3.2.6 Maximally localized Wannier states for $(\frac{1}{2}, 1)$ with $g \rightarrow 0$

As usual, we start from $(\frac{1}{2}, 1)$ spin representation in the limit case $g \rightarrow 0$, which is the unique system for which the maximally localized states can be obtained analytically. Indeed in this case we do not even need to minimize the spread functional of section 3.2.3.

In section 3.1.1 we already found the ground-state in this particular regime, using a reference to the Ising mapping of section 2.6:

$$|\Omega\rangle = |+\rangle \otimes |+\rangle \otimes \dots \otimes |+\rangle. \quad (3.66)$$

Actually, we already found the maximally localized state on a generic site j , which is obtained flipping the x -spin at site j with respect the vacuum.

$$|j\rangle = |+\rangle \otimes \dots \otimes |+\rangle \otimes \underbrace{|-\rangle}_{j^{\text{th}} \text{ site}} \otimes |+\rangle \otimes \dots \otimes |+\rangle. \quad (3.67)$$

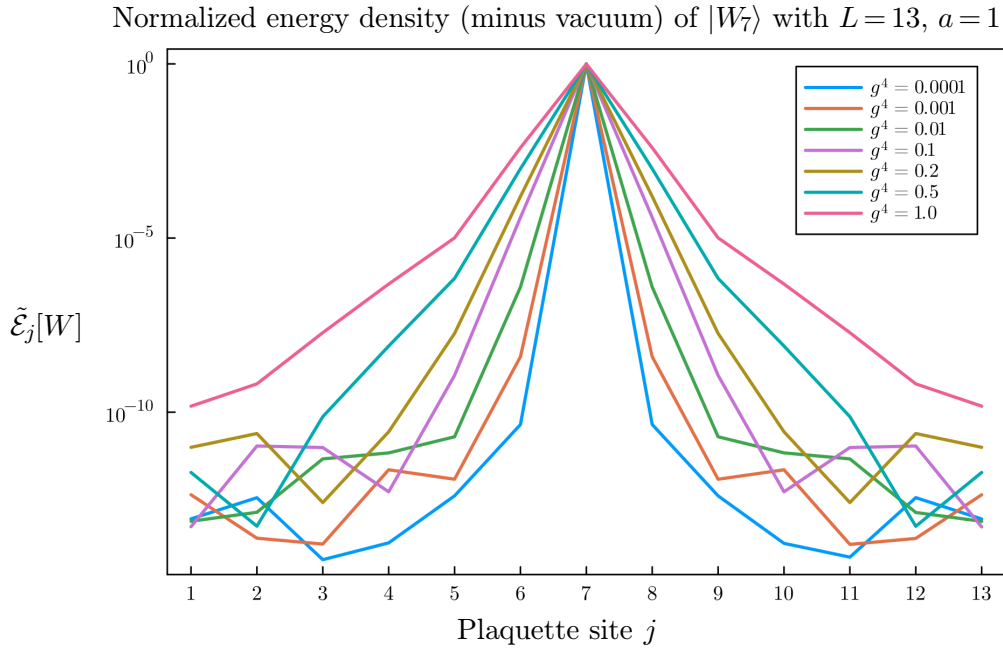


Figure 3.2. Normalized local energy density of the maximally localized Wannier states as a function of the plaquette site j .

These states are maximally localized by definition (they are different with respect the vacuum just from a single site j), but as we showed in section 3.1.1 they are also single-particle states (they belongs to the first energy band). Thus, they are exactly the maximally localized Wannier states we are looking for:

$$|W_j\rangle = |j\rangle. \quad (3.68)$$

3.2.7 Numerical results for $(\frac{1}{2}, 1)$ with finite g

For $g \neq 0$ we need to minimize the spread functional (3.53) defined in section 3.2.3 to find the maximally localized states.

We consider the case of $(\frac{1}{2}, 1)$ spin representation, and we minimize the spread functional $\sigma^2[W_\theta]$ for different values of g inside the range $[0, 1]$. After the minimization of σ^2 , we can represent the maximally localized Wannier state $|W\rangle$ plotting the *normalized energy density* after having subtracted the vacuum energy density:

$$\tilde{\mathcal{E}}_j[\phi] \equiv \frac{\langle W | \hat{H}_j | W \rangle - \langle \Omega | \hat{H}_j | \Omega \rangle}{\langle W | \hat{H} | W \rangle - \langle \Omega | \hat{H} | \Omega \rangle}. \quad (3.69)$$

Fig. 3.2 shows the energy density distribution of $|W\rangle$ after the spread functional minimization for different values of the coupling g . We can clearly see that the spread of $|W\rangle$ increases with g . This fact is confirmed by the plot of Fig. 3.3, where the minimum spread functional^{3.5} σ in function of the coupling g is displayed, for different values of the system

^{3.5} Be careful that in this case σ is represented, not σ^2 .

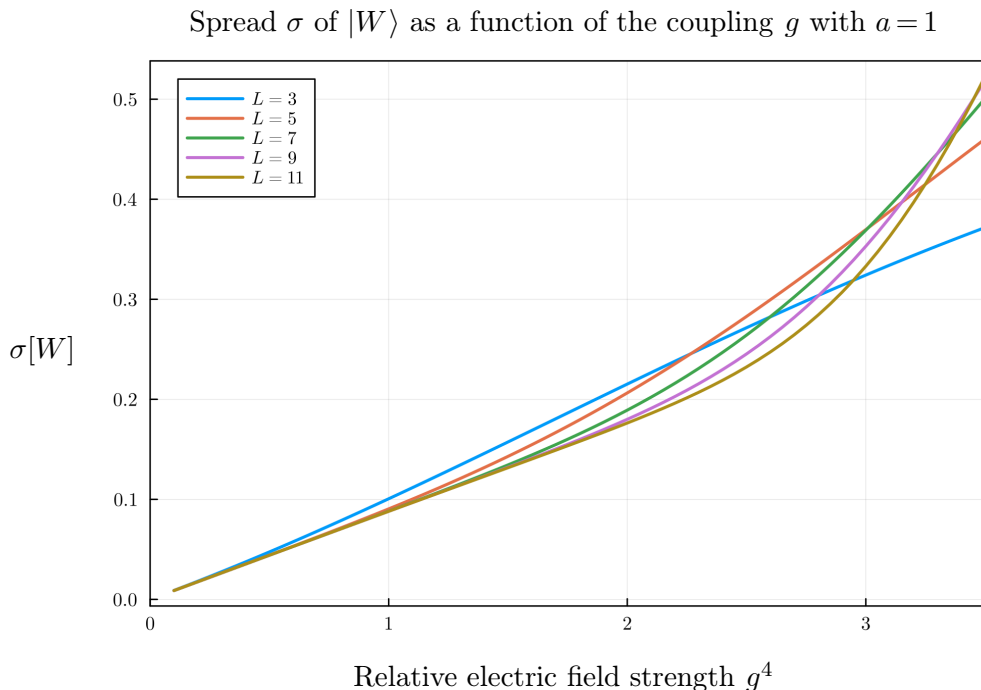


Figure 3.3. The energy spread $\sigma[W]$ of the maximally localized Wannier function after minimization as a function of g for different values of the system size L .

size L . In particular, numerically we find that the asymptotic behavior of σ is linear for small g :

$$\sigma[W] = (0.0883\dots) \cdot g^4 + \mathcal{O}(g^8). \quad (3.70)$$

The coefficient before the g^4 term in (3.70) can be probably obtained with a highly non-trivial calculation in perturbation theory. The formula (3.70) is consistent with the fact that $\sigma \rightarrow 0$ for $g \rightarrow 0$, i.e. the Wannier state is localized in a single plaquette for $g \rightarrow 0$, as we found in section 3.2.6.

3.3 Constructing the excitation operator \hat{W}

The goal of this section is to describe a way to construct an operator that we will call a *localized excitation operator* \hat{W}_j of a plaquette site j of the lattice.

The reasons why we need a localized *operator* and not a localized *state*, is the fact that with an operator one can also create multi-particle states applying it multiple time to the vacuum state. Of course this cannot be achieved using only the Wannier states $|W_j\rangle$, from which one can only create only single-particle states.

The crucial aspect that we want to show in this section is that the behavior of this operator \hat{W} converge quite quickly as the system size L increases, and thus already at intermediate system sizes (like $L = 13$) these operators can be applied to a vacuum of a system with very large L (as we will do with Tensor Networks in section 4).

Due to the translational properties of the vacuum $|\Omega\rangle$ and of the Wannier states $|W_j\rangle$, one can find just a localized excitation operator for a specific plaquette (like the central one), and then find all the others just applying the translation operator \hat{T} .

3.3.1 Presentation of the problem

Let $|W_j\rangle$ be a maximally localized Wannier state. Let \hat{U}_j the gauge-invariant single-plaquette operator of the j -th plaquette of the ladder, so from now on we will use the following notation:

$$\hat{U}_j \equiv \hat{U}_{\square,j} = \hat{S}_{B,j}^+ \hat{S}_{R,j}^+ \hat{S}_{T,j}^- \hat{S}_{L,j}^-. \quad (3.71)$$

We now want to find an operator \hat{W}_j , with the following properties:

1. \hat{W}_j produces the Wannier function $|W_j\rangle$, maximally localized around the site j , when applied to the vacuum:

$$\hat{W}_j |\Omega\rangle = |W_j\rangle; \quad (3.72)$$

2. \hat{W}_j can be written as a *linear combination of compositions of gauge-invariant single plaquette operators* \hat{U}_j and \hat{U}_j^\dagger of the ladder for different plaquette sites. For instance

$$\hat{W}_j = c_1 \hat{U}_1 + c_2 \hat{U}_1^\dagger + c_3 \hat{U}_1 \hat{U}_2^\dagger + c_4 \hat{U}_2 \hat{U}_1^\dagger \hat{U}_5 + c_5 \hat{U}_6^\dagger \hat{U}_2^\dagger \hat{U}_4 + \dots \quad (3.73)$$

where $c_k \in \mathbb{C}$ are complex coefficients to determine analytically or numerically.

If we require only the condition (1.), the problem would be trivial because for instance the operator $|W\rangle\langle\Omega|$ already satisfies that condition. Instead, finding \hat{W} with both the conditions is non-trivial in general.

We will give some arguments in favor of the *existence* of \hat{W}_j in the following sections. About *uniqueness*, since in a generic system the space of operators is larger than the space of states, in general the number of all the possible (independent) compositions of plaquette operators \hat{U}, \hat{U}^\dagger are way higher than the dimension of the system, and the problem is under-constrained. In other words, the operator which satisfies (1.) and (2.) is not unique without other constraints. To solve this problem one should always choose the *simplest* solution, i.e. the one which contains less information. One possible way is to exploit *symmetries* when possible.

3.3.2 The operator in the case $(\frac{1}{2}, 1)$ and $g \rightarrow 0$

As usual, we first find the operator \hat{W}_j in the $(\frac{1}{2}, 1)$ spin representation in the limit case $g \rightarrow 0$. From the previous sections we already know the exact form of the vacuum (3.5) and of the maximally localized Wannier state (3.67) in this case.

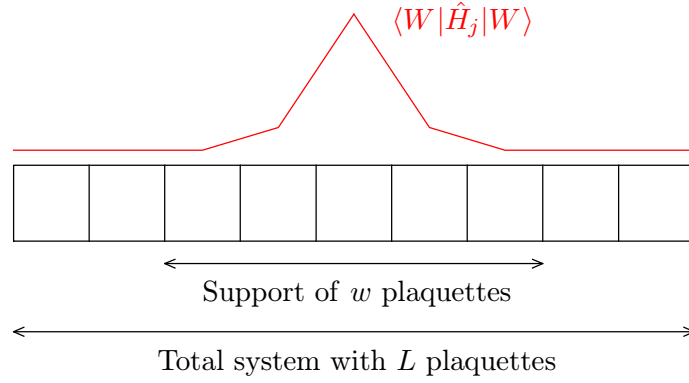


Figure 3.4. We suppose that the energy density of the Wannier state $|W\rangle$ is localized on a support of w plaquettes. Outside of this region, the state is approximately the vacuum $|\Omega\rangle$.

Using the Ising model mapping in this regime, we know that an operator that applied to the Ising vacuum $|0\rangle$ (with $\lambda \rightarrow \infty$) returns the maximally localized state $|j\rangle$ is the Pauli matrix $\hat{\sigma}_j^z$ (which flips the spin along the x -axis):

$$\hat{\sigma}_j^z (|+\rangle \otimes \dots \otimes |+\rangle_j \otimes \dots \otimes |+\rangle) = |+\rangle \otimes \dots \otimes |-\rangle_j \otimes \dots \otimes |+\rangle. \quad (3.74)$$

Hence we can write:

$$|j\rangle = \hat{\sigma}_j^z |0\rangle. \quad (3.75)$$

So $\hat{\sigma}_j^z$ is an example of excitation operator we are looking for exploiting the Ising formalism.

The next step is to write this operator as a linear combination of compositions of plaquette operators $\hat{U}_j, \hat{U}_j^\dagger$. But from the Ising mapping we know that

$$\hat{U} \leftrightarrow 2\hat{\sigma}^-, \quad \hat{U}^\dagger \leftrightarrow 2\hat{\sigma}^+, \quad (3.76)$$

and since we know that the following identity between Pauli matrices holds

$$\hat{\sigma}_j^z = -\mathbb{I} + 2\hat{\sigma}_j^+ \hat{\sigma}_j^-, \quad (3.77)$$

we have found the excitation operator in terms of plaquette operators as:

$$\hat{W}_j = -\mathbb{I} + \frac{1}{2} \hat{U}_j^\dagger \hat{U}_j. \quad (3.78)$$

Indeed, both \mathbb{I} and $\hat{U}_j^\dagger \hat{U}_j$ are valid compositions of \hat{U}_j and \hat{U}_j^\dagger .

3.3.3 A general numerical method

We now present a general method to find \hat{W} , actually valid, at least in principle, for any lattice gauge theory with a ladder geometry. We first suppose to know exactly $|W\rangle$ (any localized Wannier state) and that its *support* extends to a certain number of plaquettes. The support of the Wannier state can be defined as the region of the system for which the energy density is different from that of the vacuum (Fig. 3.4).

We first reformulate the problem in a more rigorous way. Let $\{\hat{A}_\alpha\}$ be a set of gauge-invariant operators obtained from compositions of the operators \hat{U}_j and \hat{U}_j^\dagger in the support of the Wannier state. For instance, if the Wannier state has support only in the three sites $j = 2, 3, 4$ around $j_c = 3$, an example of possible choice of $\{\hat{A}_\alpha\}$ can be the following:

$$\hat{A}_1 = \mathbb{I}, \quad \hat{A}_2 = \hat{U}_3, \quad \hat{A}_3 = \hat{U}_3^\dagger, \quad \hat{A}_4 = \hat{U}_2 \hat{U}_4^\dagger, \quad \hat{A}_5 = \hat{U}_2^\dagger \hat{U}_4. \quad (3.79)$$

We ask which is the best choice of $\{\hat{A}_\alpha\}$ and of the complex coefficients $c_\alpha \in \mathbb{C}$ such that

$$\hat{W} = \sum_{\alpha} c_{\alpha} \hat{A}_{\alpha}. \quad \hat{W} |\Omega\rangle = |W\rangle. \quad (3.80)$$

Now, let $\{|A_\alpha\rangle\}$ be the set of states created from the vacuum by the operators \hat{A}_α :

$$|A_\alpha\rangle \equiv \hat{A}_\alpha |\Omega\rangle.$$

The best choice of $\{\hat{A}_\alpha\}$ is the one such that $\{|A_\alpha\rangle\}$ spans a subspace of the Hilbert space of the theory where the state $|W\rangle$ is contained. Indeed, if this happens, we are sure that there exists c_α such that (3.80) holds, and so we are sure about the existence of the operator \hat{W} which satisfies the conditions (1.) and (2.) listed at the beginning of the section. Actually, the choice of $\{\hat{A}_\alpha\}$ is not trivial and it depends on the specific lattice theory. If the Wannier has a certain support in the 1-dimensional lattice, then $\{\hat{A}_\alpha\}$ should be operators which acts only in that support.

The best choice of the coefficients c_α , that we will denote with a vector of complex entries $\mathbf{c} = (c_1, c_2, c_3, \dots)$ is the one that *minimizes the (squared) norm of the difference* between the operator applied to the vacuum and the Wannier state. In other words, we have to solve the minimization problem for the functional:

$$f(\mathbf{c}) \equiv \|\hat{W} |\Omega\rangle - |W\rangle\|^2.$$

We first rewrite this functional using (3.80):

$$\begin{aligned} f(\mathbf{c}) &= \left\| \sum_{\alpha} c_{\alpha} \hat{A}_{\alpha} |\Omega\rangle - |W\rangle \right\|^2 \\ &= \left\| \sum_{\alpha} c_{\alpha} |A_{\alpha}\rangle - |W\rangle \right\|^2 \\ &= \left(\sum_{\alpha} \langle A_{\alpha} | c_{\alpha}^* - \langle \phi | \right) \left(\sum_{\beta} c_{\beta} |A_{\beta}\rangle - |W\rangle \right) \\ &= \sum_{\alpha, \beta} c_{\alpha}^* c_{\beta} \langle A_{\alpha} | A_{\beta} \rangle - \sum_{\alpha} c_{\alpha} \langle W | A_{\alpha} \rangle - \sum_{\alpha} c_{\alpha}^* \langle A_{\alpha} | W \rangle + \langle W | W \rangle. \end{aligned}$$

The gradient of the functional f with respect the complex parameters c_α can be computed with respect c_α or c_α^* as to independent components (one will be the adjoint problem of the other). Let's take the derivative of f with respect c_α^* :

$$\frac{\partial}{\partial c_\alpha^*} f(\mathbf{c}) = \sum_{\beta} c_{\beta} \langle A_{\alpha} | A_{\beta} \rangle - \langle A_{\alpha} | W \rangle = 0. \quad (3.81)$$

Defining

$$\mathcal{A}_{\alpha\beta} \equiv \langle A_\alpha | A_\beta \rangle, \quad b_\alpha \equiv \langle A_\alpha | W \rangle, \quad (3.82)$$

where $\mathcal{A}_{\alpha\beta}$ is the *Hessian matrix* of f and b_α is the vector of known terms: the problem is then reduced to a linear system

$$\sum_{\alpha} \mathcal{A}_{\alpha\beta} c_\alpha = b_\beta. \quad (3.83)$$

Hence, in order to find the coefficients c_α we need to find the inverse matrix \mathcal{A}^{-1} .

After the minimization, one can use the functional (3.53) as an estimation of the interpolation error: the more the norm of the difference is low, the more the two states are near and $\hat{W}|\Omega\rangle$ approximates the Wannier correctly.

Alternatively, defining the *fidelity* (for normalized states) between two states $|\phi_1\rangle, |\phi_2\rangle$ as

$$F(|\phi_1\rangle, |\phi_2\rangle) \equiv |\langle \phi_1 | \phi_2 \rangle|^2, \quad (3.84)$$

one can use the so-called *infidelity* $1 - F(|W\rangle, \hat{W}|\Omega\rangle)$ as an alternative metric to measure the interpolation error after the minimization.

3.3.4 Application to $(\frac{1}{2}, 1)$ with $g \rightarrow 0$

In the spin representation $(\frac{1}{2}, 1)$ with $g = 0$, the Wannier function has a single plaquette as support. Here we confirm this fact applying the method of the previous section giving also an example.

Suppose now we want to find the excitation operator using the two local operators

$$\hat{A}_1 = \mathbb{I}, \quad \hat{A}_2 = \hat{U}_j^\dagger \hat{U}_j \leftrightarrow 4\hat{\sigma}_j^+ \hat{\sigma}_j^-. \quad (3.85)$$

Using the formalism of the previous paragraph we obtain

$$|A_1\rangle = \mathbb{I}|\Omega\rangle = |\Omega\rangle \leftrightarrow |0\rangle, \quad |A_2\rangle = \hat{U}_j^\dagger \hat{U}_j |\Omega\rangle \leftrightarrow 4\hat{\sigma}_j^+ \hat{\sigma}_j^- |0\rangle. \quad (3.86)$$

The vectors $|A_1\rangle$ and $|A_2\rangle$ are linearly independent and they span the whole two-dimensional Hilbert space, so the set $\{\hat{A}_1, \hat{A}_2\}$ is a good choice to solve the problem. From (3.82) we can compute the Hessian matrix \mathcal{A} and the known terms vector \mathbf{b} which read

$$\mathcal{A} = \begin{pmatrix} 1 & 2 \\ 2 & 8 \end{pmatrix}, \quad \mathbf{b} = \begin{pmatrix} 0 \\ 2 \end{pmatrix}. \quad (3.87)$$

Thus, we compute the coefficients vector $\mathbf{c} = \mathcal{A}^{-1} \mathbf{b}$, from which we obtain

$$c_1 = -1, \quad c_2 = \frac{1}{2}. \quad (3.88)$$

This finally gives the excitation operator

$$\hat{W}_j = -\mathbb{I} + \frac{1}{2} \hat{U}_j \hat{U}_j^\dagger \leftrightarrow -\mathbb{I} + 2\hat{\sigma}_j^+ \hat{\sigma}_j^- = \hat{\sigma}_j^z, \quad (3.89)$$

which is exactly the same result we found intuitively in section 3.3.2.

3.3.5 Numerical results for $(\frac{1}{2}, 1)$, small g and $L = 3$

Since the perturbation parameter of the Hamiltonian is g^4 , if the coupling g is non-vanishing but small enough (for instance $g = 0.1$) we expect that to the excitation operator (3.89) it would add a perturbation terms proportional to powers of g^4 :

$$\hat{W}_j(g \sim 0) = -\mathbb{I} + \frac{1}{2}\hat{U}_j\hat{U}_j^\dagger + \mathcal{O}(g^4). \quad (3.90)$$

In this section we try to find explicitly the first terms of this perturbative expansion for a lattice of three plaquettes ($L = 3$) and for a Wannier state $|W_2\rangle$ localized in the central plaquette $j = 2$, using the method of section 3.3.3.

Let's consider the case $L = 3$ in representation $(\frac{1}{2}, 1)$. We first we want to choose a minimal set of 3-plaquette operators \hat{A}_α which applied to the vacuum span a subspace where the Wannier is contained.

We notice that many compositions of \hat{U}, \hat{U}^\dagger are not independent from each other. To understand this dependence, we have to consider the commutation rules between these operators. From the mapping (3.76) the the following commutation relations holds:

$$\{\hat{U}_j, \hat{U}_j^\dagger\} = 4\mathbb{I}, \quad [\hat{U}_i, \hat{U}_j] = [\hat{U}_i^\dagger, \hat{U}_j^\dagger] = [\hat{U}_i, \hat{U}_j^\dagger] = 0 \quad \forall i \neq j. \quad (3.91)$$

From these commutation relations it follows that four independent plaquette operators are the following (which we represent with a visual notation):

$$\mathbb{I} = \square \quad \hat{U} = \square \curvearrowright \quad \hat{U}^\dagger = \curvearrowleft \square \quad \hat{U}^\dagger\hat{U} = \bigcirc. \quad (3.92)$$

Now, since the Wannier state $|W_2\rangle$ is symmetric with respect the central plaquette $j = 2$, the operator \hat{W}_2 must be symmetric as well. This helps us to make a choice for the minimal set $\{\hat{A}_\alpha\}$. Up to commutation relations (3.91) all the possible symmetric compositions for three plaquette sites $j = 1, 2, 3$ are:

$$\begin{aligned} \hat{A}_1 = \mathbb{I} &= \square \square \square & \hat{A}_5 = \hat{U}_2^\dagger\hat{U}_2 &= \square \bigcirc \square \\ \hat{A}_2 = \hat{U}_1^\dagger\hat{U}_3 &= \curvearrowleft \square \curvearrowright & \hat{A}_6 = \hat{U}_1^\dagger\hat{U}_2^\dagger\hat{U}_2\hat{U}_3 &= \curvearrowleft \bigcirc \curvearrowright \\ \hat{A}_3 = \hat{U}_1\hat{U}_3^\dagger &= \curvearrowright \square \curvearrowleft & \hat{A}_7 = \hat{U}_1\hat{U}_2^\dagger\hat{U}_2\hat{U}_3^\dagger &= \curvearrowright \bigcirc \curvearrowleft \\ \hat{A}_4 = \hat{U}_1^\dagger\hat{U}_1\hat{U}_3^\dagger\hat{U}_3 &= \bigcirc \square \bigcirc & \hat{A}_8 = \hat{U}_1^\dagger\hat{U}_1\hat{U}_2^\dagger\hat{U}_2\hat{U}_3^\dagger\hat{U}_3 &= \bigcirc \bigcirc \bigcirc \end{aligned} \quad (3.93)$$

These are 8 independent operators which once applied to the vacuum spans all the non-trivial polarization sector, which has dimension $2^L = 2^3 = 8$. One can numerically solve the linear system (3.83), and finding an inverse matrix \mathcal{A}^{-1} obtaining the coefficients for the operators (3.93), which gives the following pattern (checked numerically setting $g = 0.1$):

$$\begin{aligned} \hat{W}_2 &= -\mathbb{I} + \frac{1}{2}\hat{U}_2^\dagger\hat{U}_2 && \text{(single-plaquette terms)} \\ &+ \left(\frac{2}{25}\mathbb{I} - \frac{1}{32}\hat{U}_1^\dagger\hat{U}_3 - \frac{1}{32}\hat{U}_1\hat{U}_3^\dagger - \frac{1}{64}\hat{U}_1^\dagger\hat{U}_1\hat{U}_3^\dagger\hat{U}_3 \right) \cdot g^4 && \text{(1st order 3-plaquette terms)} \\ &+ \left(\frac{1}{512}\hat{U}_1^\dagger\hat{U}_2^\dagger\hat{U}_2\hat{U}_3 + \frac{1}{512}\hat{U}_1\hat{U}_2^\dagger\hat{U}_2\hat{U}_3^\dagger \right) \cdot g^8 && \text{(2nd order 3-plaquette terms)} \end{aligned}$$

$$+ \mathcal{O}(g^{12}).$$

For $g=0.1$, after minimization of the functional, the norm of the difference between the two states and the infidelity are of the order

$$\|\hat{W}_2|\Omega\rangle - |W_2\rangle\| \sim 10^{-6}, \quad 1 - F(\hat{W}_2|\Omega\rangle, |W_2\rangle) \sim 10^{-12}.$$

3.3.6 Increasing the Wannier support up to $L = 13$

The operations of the previous paragraph can be generalized for $L > 3$, constructing all the independent symmetric gauge invariant operators \hat{A} from \hat{U}, \hat{U}^\dagger . However, since listing all the symmetric configuration becomes difficult for higher values of L , we show here that a “brute force” computation approach also works. Indeed, the symmetries we exploited in the previous section cannot be anymore available for higher spin representations or for other models. Conversely, for any model, we can always consider a large number of \hat{A}_α operators independently of the symmetries, and choosing a set of linear independent states $|A_\alpha\rangle$ in such a way that the linear algebra problem to find \hat{W} is at least always solvable.

As an example, we remain in the $(\frac{1}{2}, 1)$ representation case and find a proper set of the operators \hat{K}_α for a generic system size L . Let's suppose that we want to approximate the Wannier state with a subsystem of w plaquettes (Fig. 3.4). In this particular spin representation, the dimension of the Hilbert space of this subsystem where the Wannier is contained is 2^w (aside from the two trivial sectors). It is possible to show numerically that a set $\{\hat{A}_\alpha\}$ of exactly 2^w operators which applied to the vacuum $|\Omega\rangle$ span all the 2^w -dimensional Hilbert space is the following:

$$\begin{aligned}
\hat{A}_1 &= \mathbb{I} &= & \square \square \square \square \dots \\
\hat{A}_2 &= \hat{U}_1 &= & \begin{array}{|c|} \hline \curvearrowright \\ \hline \end{array} \square \square \square \dots \\
\hat{A}_3 &= \hat{U}_2 &= & \square \begin{array}{|c|} \hline \curvearrowright \\ \hline \end{array} \square \square \dots \\
\hat{A}_4 &= \hat{U}_1 \hat{U}_2 &= & \begin{array}{|c|} \hline \curvearrowright \\ \hline \end{array} \begin{array}{|c|} \hline \curvearrowright \\ \hline \end{array} \square \square \dots \\
\hat{A}_5 &= \hat{U}_3 &= & \square \square \begin{array}{|c|} \hline \curvearrowright \\ \hline \end{array} \square \dots \\
\hat{A}_6 &= \hat{U}_1 \hat{U}_3 &= & \begin{array}{|c|} \hline \curvearrowright \\ \hline \end{array} \square \begin{array}{|c|} \hline \curvearrowright \\ \hline \end{array} \square \dots \\
\hat{A}_7 &= \hat{U}_2 \hat{U}_3 &= & \square \begin{array}{|c|} \hline \curvearrowright \\ \hline \end{array} \begin{array}{|c|} \hline \curvearrowright \\ \hline \end{array} \square \dots \\
\hat{A}_8 &= \hat{U}_1 \hat{U}_2 \hat{U}_3 &= & \begin{array}{|c|} \hline \curvearrowright \\ \hline \end{array} \begin{array}{|c|} \hline \curvearrowright \\ \hline \end{array} \begin{array}{|c|} \hline \curvearrowright \\ \hline \end{array} \square \dots \\
&\vdots && \vdots \\
\hat{A}_{2^w} &= \hat{U}_1 \dots \hat{U}_{2^w} &= & \begin{array}{|c|} \hline \curvearrowright \\ \hline \end{array} \begin{array}{|c|} \hline \curvearrowright \\ \hline \end{array} \begin{array}{|c|} \hline \curvearrowright \\ \hline \end{array} \begin{array}{|c|} \hline \curvearrowright \\ \hline \end{array} \dots
\end{aligned} \tag{3.94}$$

which is very simple to compute numerically and does not require any particular symmetry argument. In particular, if $w = L$, we can interpolate any state of the Hilbert space of the system using the algorithm showed in section 3.3.3.

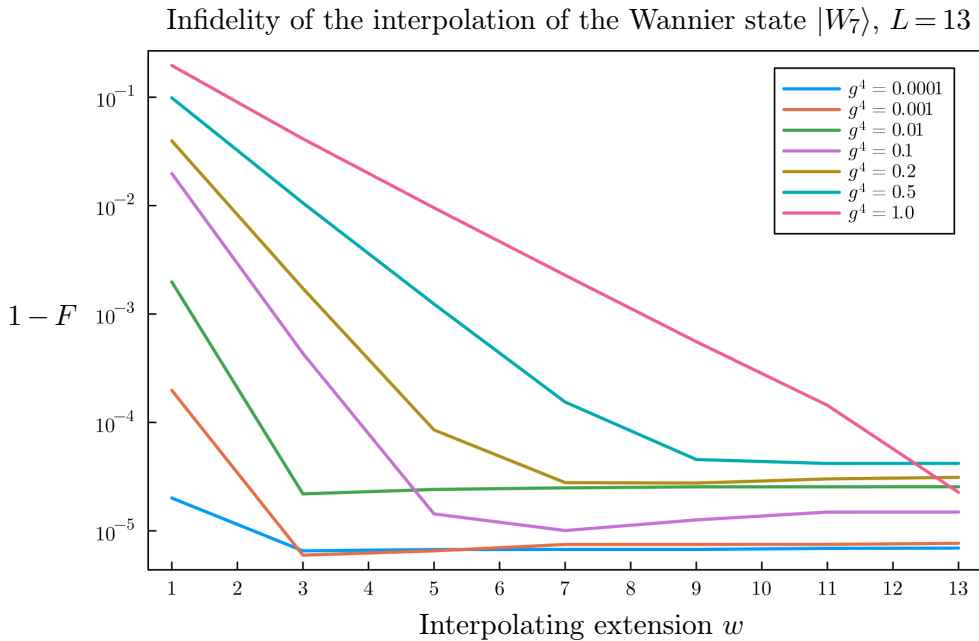


Figure 3.5. Infidelity between the interpolating state $\hat{W}|\Omega\rangle$ and the Wannier state $|W\rangle$ using a w -plaquette support centered in a system with $L = 13$ plaquettes in the lowest spin representation $(\frac{1}{2}, 1)$. Here the infidelity assumes the meaning of interpolation error of the algorithm.

Figure 3.5 shows the interpolation error (infidelity $1 - F$) of the maximally localized Wannier states in the central plaquette for a system with $L = 13$ size using this approach. As operator basis $\{\hat{A}_\alpha\}$, the set (3.94) has been chosen. In this plot, the infidelity is computed for different values of the coupling, changing the number w of plaquette size of the interpolating subsystem.

We notice a crucial fact: after a certain value of w , that we will denote with w^* , the infidelity is minimal and it remains constant for higher values of w (there is a sort of plateau). This means that using the numerical precision at disposal, w^* is the smallest number of plaquettes for which the Wannier state is *maximally interpolated* by the set of operators $\{\hat{A}_\alpha\}$. Thus, w^* defines exactly the *support* of the Wannier state $|W\rangle$. Regions outside that support are approximately equal to the ground state.

Another crucial fact observed is that all the coefficients c_α associated to the operators (3.94) converges quickly to a finite value when L increases and it stabilizes at $w > w^*$. This is what have been observed numerically in this spin representation, but since the generalization of this approach is straightforward to other models, this result represents a strong indication that systems with intermediate sizes are enough to produce localized states which will work also if applied to the vacuum in the thermodynamic limit $L \rightarrow \infty$ (see chapter 4 about DMRG with tensor networks).

3.3.7 Higher spin representations and other lattice models

This method, at least in principle, can be applied to any lattice system, because it only uses the plaquette gauge invariant operators $\hat{U}_j, \hat{U}_j^\dagger$, which are always defined for any lattice gauge theory.

However, the existence and uniqueness of this way to write the operator \hat{W} , which depends on the choice of the operator basis $\{\hat{A}_\alpha\}$, are not trivial aspects for a generic theory. The main problem for higher spin representations, for which we will not do concrete numerical examples in this thesis, is that the commutation relation (3.91) do not hold anymore, and so listing all the possible \hat{A}_α becomes difficult. However, since the space of gauge invariant operators has a dimension which is way higher than the space of gauge invariant states, we conjecture, without giving a proof, that it is always possible to choose a set $\{\hat{A}_\alpha\}$ such that the set of states $\{|A_\alpha\rangle\}$ span the whole Hilbert space of the system.

We lastly claim that the procedure described in section 3.3.3 could fit also to lattice systems with higher space dimensionality, supposing having yet at disposal a state $|W\rangle$ that we want to interpolate, which is enough localized inside a finite support.

3.4 The wave-packet creation operator $\hat{\Psi}$

In this section we discuss how to create a single-particle wave-packet state $|\Psi\rangle$ and a single-particle wave-packet creation operator $\hat{\Psi}$ respectively from the Wannier states $|W\rangle$ and the Wannier local excitation operator \hat{W} . In particular, we require $\hat{\Psi}$ to have the property of creating $|\Psi\rangle$ from the ground state:

$$\hat{\Psi}|\Omega\rangle = |\Psi\rangle. \quad (3.95)$$

3.4.1 Wave-packet state $|\Psi\rangle$ from the Wannier states $|W_j\rangle$

Since the set of Wannier states $\{|W_j\rangle\}$ constitutes a basis of the subspace of single-particle states, we can construct any single particle state $|\Psi\rangle$ from a linear combination of $|W_j\rangle$. But if we consider the maximally localized $|W_j\rangle$, we have the ability to choose any spatial distribution of energy density of a state, i.e. to construct a single-particle state with any localized shape.

More precisely, let's consider the state

$$|\Psi\rangle = \sum_j \Psi_j |W_j\rangle. \quad (3.96)$$

where $\Psi_j \in \mathbb{C}$ are complex coefficients assigned to the sites of the lattice. From the normalization condition of the state, we have to require that

$$\sum_j |\Psi_j|^2 = \langle\Psi|\Psi\rangle = 1. \quad (3.97)$$

To understand the meaning of the coefficients Ψ_j , let's assume that $|W_j\rangle$ is well space-localized, namely that the energy density is localized only on the site j , and for all the other sites the system is very similar to the vacuum. Assuming this condition it is possible to show that the normalized energy density (3.69) is obtained as the modulus square of the coefficients Ψ_j :

$$\tilde{\mathcal{E}}_j[\Psi] = |\Psi_j|^2. \quad (3.98)$$

This means that, for enough spatial localized Wannier states, the function Ψ_j is the lattice *wave-function* of a single-particle state.

If we want to control the momentum localization we can define the wave-function in the reciprocal (momentum) space, and then define the coefficients Ψ_j as a Fourier transform Ψ_k . The domain of Ψ_k is the so-called *first Brillouin zone*. If the lattice is finite ($L < \infty$) the Brillouin zone will be discrete, and this discretization becomes finer and finer as L increase. For $L \rightarrow \infty$ the Brillouin zone is the continuous interval $[-\pi/a, \pi/a]$. Thus, we define the wave-function in the real space as

$$\begin{aligned}\Psi_j &= \frac{1}{\mathcal{N}} \sum_k \Psi_k e^{ikj} && \text{for a finite lattice with } L \text{ sites;} \\ \Psi_j &= \frac{1}{\mathcal{N}} \int dk \Psi(k) e^{ikj} && \text{for a lattice with } L \rightarrow \infty \text{ sites,}\end{aligned}\tag{3.99}$$

where \mathcal{N} is a proper normalization factor defined in such a way that (3.97) holds, while k ranges over the first Brillouin zone.

3.4.2 The Gaussian wave-packet

As an example, let's consider a very large lattice with $L \rightarrow \infty$ (using numerical tools like the Tensor Network framework, described in chapter 4) and a wave-function which is Gaussian in the reciprocal space:

$$\Psi(k) \sim e^{-(k-k_0)^2/2\tilde{\sigma}^2},\tag{3.100}$$

where k_0 and $\tilde{\sigma}$ are respectively the average and the dispersion of the momentum distribution. If $\tilde{\sigma}$ is small enough with respect the Brillouin zone length, namely

$$\tilde{\sigma} \ll \frac{1}{a},\tag{3.101}$$

then $\Psi(k)$ is very peaked and the wave-function has a definite momentum k_0 . In this case, $\Psi(k) \approx 0$ for values of k distant from k_0 , and we can approximate the integral in (3.99) with an integral over \mathbb{R} :

$$\Psi_j = \int_{-k/a}^{k/a} dk \Psi(k) \approx \int_{-\infty}^{+\infty} dk \Psi(k).\tag{3.102}$$

Using this approximation, the Fourier transform of (3.100) is a “rotating” (with a frequency k_0) *Gaussian wave-packet*

$$\Psi_j \sim e^{-(j-j_0)^2/2\sigma} e^{ij k_0} \quad \text{with} \quad \sigma = \frac{1}{\tilde{\sigma}}.\tag{3.103}$$

Thus, we can define the gaussian wave-packet centered in j with spatial dispersion σ and momentum k using Wannier functions as

$$|\Psi(j, \sigma, k)\rangle \equiv \frac{1}{\mathcal{N}} \sum_{j'} e^{-(j'-j)^2/2\sigma} e^{ij'k} |W_{j'}\rangle.\tag{3.104}$$

From (3.103) we notice, as expected from the indetermination principle, that the momentum localization $\tilde{\sigma}$ and the spatial localization σ are inversely proportional. In particular, the condition (3.101) becomes the fact that the Gaussian width in the real space must be way larger than the lattice spacing

$$\sigma \gg a. \quad (3.105)$$

If this condition cannot be satisfied (e.g. the lattice is not large enough), then the approximation (3.102) does not hold anymore and the coefficients Ψ_j should be computed numerically in the finite Brillouin zone.

3.4.3 Wave-packet operator $\hat{\Psi}$ from the excitation operators \hat{W}_j

Once defined a single particle wave-packet state, we want to compute a wave-packet operator $\hat{\Psi}$ which can be used to construct wave-packets from the vacuum state. Requiring (3.95) we can write

$$\hat{\Psi}|\Omega\rangle = |\Psi\rangle = \sum_j \Psi_j |W_j\rangle = \sum_j \Psi_j \hat{W}_j |\Omega\rangle. \quad (3.106)$$

Thus, from this condition we require the operator $\hat{\Psi}$ to have the following form:

$$\hat{\Psi} \equiv \sum_j \Psi_j \hat{W}_j, \quad \text{with} \quad \hat{W}_j = \sum_{\alpha} c_{\alpha} \hat{A}_{\alpha}. \quad (3.107)$$

Since \hat{A}_{α} is written as a linear combination of compositions of \hat{U} and \hat{U}^{\dagger} operators, indeed also the wave-packet operator $\hat{\Psi}$ will have this property. This is a crucial remark because it allows $\hat{\Psi}$ to be written as a Matrix Product Operator (see chapter 4).

Thus, from the analysis of the previous section, we can for instance define a *Gaussian wave-packet operator*

$$\hat{\Psi}(j, \sigma, k) \equiv \frac{1}{\mathcal{N}} \sum_{j'} e^{-(j'-j)^2/2\sigma} e^{ijk} \hat{W}_{j'}. \quad (3.108)$$

Actually, numerically we don't need to explicitly compute the normalization factor \mathcal{N} , because we can properly normalize states after the application of an operator.

The operator $\hat{\Psi}(j, \sigma, k)$ produces a single-particle state if applied once to the vacuum $|\Omega\rangle$. However, we can apply it on different regions of the lattice, producing multi-particle states. For instance, if we want to prepare a typical initial *scattering state* of two Gaussian wave-packets localized in two distant initial positions j_1 and j_2 , with spatial localization $\sigma \ll |j_1 - j_2|$ for both and with same but opposite momentum k , we can construct the state as

$$|\text{initial scattering state}\rangle = \hat{\Psi}(j_1, \sigma, k) \hat{\Psi}(j_2, \sigma, -k) |\Omega\rangle. \quad (3.109)$$

Of course, a multi-particle state as (3.109) must be properly normalized *after* the application of the two wave-packet operators.

Chapter 4

Tensor Network Methods

Tensor Networks (TNs) [31] represent a versatile and powerful framework within the field of quantum physics and machine learning that has received large attention in recent years, particularly in the field of simulation techniques for many-body quantum lattice systems [54]. At their core, TNs are a mathematical representation of high-dimensional tensors that enable an efficient manipulation and analysis of complex data structures. TNs have been extensively applied in various quantum many-body systems, mainly in condensed matter physics, but also in quantum chemistry [55], offering efficient descriptions of ground states and excited states of quantum systems. The utilities of TNs goes beyond quantum physics, with remarkable applications in machine learning tasks like tensor-based deep learning architectures [56].

TNs offer several advantages over Monte Carlo methods in tackling the *numerical sign problem* [11]. TNs naturally handle one-dimensional systems, but offer also scalable algorithms for higher-dimensional systems, making them versatile and applicable to a wide range of physical systems. In particular, TN methods have proven to be a valuable and promising approach for tackling the complex and computationally demanding problems arising in Lattice Gauge Theories.

In this section, after an introduction to the Tensor Network notation, we list the most important tools which are used in this fields, such as the Matrix Product States (MPS) and Operators (MPO), and the related algorithms.

4.1 The Tensor Network notation

The *Tensor Network notation* is a compact and graphical representation used to depict the structure of TNs. It simplifies the visualization and understanding of complex TN diagrams. The TN notation represents a tensor structure as a *graph*, typically follows the following rules:

1. **nodes**: each *node* in the diagram represents a *tensor*. The shape of the node sometimes indicates the dimensionality of the corresponding tensor: a circle for a single-index tensor (a vector) and a square for a multi-indices tensor (a matrix or a tensor);

2. **lines and indices:** the *lines* connecting the nodes represent the *indices* of the tensors; these lines are also called *legs* or *bonds*; each line corresponds to a specific index of the tensor, and the *number of lines* connected to a node corresponds to the *rank* of the tensor; each index has a *dimension* d (e.g. the side length of a matrix); the *names* of the indices are denoted by *labels* on the lines, usually lowercase letters like i, j, k , etc. In this way we can represent vectors, matrices and tensors in the following visual notation:

$$v_i = \begin{array}{c} \textcircled{v} \\ | \\ i \end{array}, \quad M_{ij} = \begin{array}{c} j \\ | \\ \boxed{M} \\ | \\ i \end{array}, \quad T_{ijk} = \begin{array}{c} j \\ | \\ k - \boxed{T} \\ | \\ i \end{array}, \quad A_{ijkl} = \begin{array}{c} j \\ | \\ k - \boxed{A} - l \\ | \\ i \end{array} \quad (4.1)$$

3. **contractions:** two indices that are connected by a line are *contracted*, meaning that they are *summed over*. The contracted indices are *muted indices* and they do not need to be labeled in the TN notation. With this convention, all the common operations as the matrix-vector product, matrix-matrix product, scalar product and vector product can be represented as follows (using Einstein convention):

$$M_{ij}v_j = \begin{array}{c} \textcircled{v} \\ | \\ \boxed{M} \\ | \\ i \end{array}, \quad A_{ij}B_{jk} = \begin{array}{c} \textcircled{v} \\ | \\ \boxed{M} \\ | \\ i \end{array}, \quad a_i b_i = \begin{array}{c} \textcircled{a} \\ | \\ \textcircled{b} \end{array}, \quad \epsilon_{ijk} a_i b_j = \begin{array}{c} \textcircled{a} - \boxed{\epsilon} - \textcircled{b} \\ | \\ k \end{array}; \quad (4.2)$$

4. **External indices:** Indices that are not connected to any other tensor are *named* indices and they are *external* indices. They represent the *input* or *output* of a TN.

By the use of this notation, every complex contraction with multiple index tensors, for which the whole structure would be difficult to understand, as well as other tensor operations, e.g. the matrix trace, can be represented, for instance:

$$A_{iklm}B_{jmn}C_{npr}u_k v_l w_p q_r = \begin{array}{c} \textcircled{v} \\ | \\ \textcircled{u} - \boxed{A} - \boxed{B} - \boxed{C} \\ | \quad | \quad | \\ i \quad j \quad \textcircled{q} \end{array}, \quad \text{Tr}(ABCD) = \begin{array}{cc} \boxed{A} & - & \boxed{B} \\ | & & | \\ \boxed{D} & - & \boxed{C} \end{array}. \quad (4.3)$$

It is always possible to *compute the contraction* between two indices, obtaining a new tensor or a scalar quantity:

$$M_{ij}v_j = \begin{array}{c} \textcircled{v} \\ | \\ \boxed{M} \\ | \\ i \end{array} = \begin{array}{c} \boxed{A} \\ | \\ i \end{array} = A_i, \quad a_i b_i = \begin{array}{c} \textcircled{a} \\ | \\ \textcircled{b} \end{array} = c \in \mathbb{R}. \quad (4.4)$$

4.1.1 Notation for quantum systems

With this notation, we can represent a generic many-body wave-function of a quantum system.

Consider a quantum local system with a d -dimensional Hilbert space \mathcal{H} (e.g. a d -level system), and local computational basis $\{|\alpha\rangle\}$. We can consider a many-body system composed of L subsystems, with a d^L -dimensional Hilbert space $\mathcal{H}_L = \mathcal{H}^{\otimes L}$ and computational basis $\{|\alpha_1 \dots \alpha_L\rangle\}$. Indeed a generic many-body vector state $|\Psi\rangle$ of \mathcal{H} can be written as

$$|\Psi\rangle = \sum_{\alpha_1 \dots \alpha_L} \Psi_{\alpha_1 \dots \alpha_L} |\alpha_1 \dots \alpha_L\rangle, \quad (4.5)$$

where $\Psi_{\alpha_1 \dots \alpha_L}$ is the *many-body wave-function* which is a matrix with d^L complex entries, which can be represented using tensor network notation as

$$\Psi_{\alpha_1 \alpha_2 \dots \alpha_L} = \begin{array}{c} \boxed{\Psi} \\ | \quad | \quad | \quad | \quad \dots \quad | \\ \alpha_1 \quad \alpha_2 \quad \alpha_3 \quad \dots \quad \alpha_L \end{array}. \quad (4.6)$$

For a quantum many-body *operator* \hat{A} acting on the many-body Hilbert space \mathcal{H} , the notation is analogous. Indeed a generic many body in the computational basis reads

$$\hat{A} = \sum_{\alpha_1 \dots \alpha_L} A_{\alpha_1 \dots \alpha_L}^{\beta_1 \dots \beta_L} |\alpha_1 \dots \alpha_L\rangle \langle \beta_1 \dots \beta_L|, \quad (4.7)$$

from which we can represent a many-body operator in a tensor network notation as:

$$A_{\alpha_1 \alpha_2 \dots \alpha_L}^{\beta_1 \beta_2 \dots \beta_L} = \begin{array}{c} \beta_1 \quad \beta_2 \quad \beta_3 \quad \dots \quad \beta_L \\ | \quad | \quad | \quad | \quad \dots \quad | \\ \boxed{A} \\ | \quad | \quad | \quad | \quad \dots \quad | \\ \alpha_1 \quad \alpha_2 \quad \alpha_3 \quad \dots \quad \alpha_L \end{array}. \quad (4.8)$$

4.2 Matrix Product States and Operators

4.2.1 Matrix Product States

The Matrix Product States (MPS) Ansatz is a specific TN architecture used to represent in a very efficient way particular quantum states in *one-dimensional* quantum many-body systems.

In an MPS, a quantum state^{4.1} (4.6) is represented as a TN consisting of a *chain of tensors*, where each tensor^{4.2} describes the local properties of an individual quantum system:

$$\psi_{j, \alpha_j}^{\sigma \sigma'} = \sigma \text{---} \textcircled{\psi_j} \text{---} \sigma', \quad (4.9)$$

\downarrow
 α_j

^{4.1.} We will often apply this *abuse of notation*, interchanging wave-functions with quantum states.

^{4.2.} Notice that in this context, the local tensors (4.9) of an MPS are usually denoted with a circle like vectors. This because the physical index α is just one (like a vector), even if the actual tensor has three indices.

where α is a *physical* many body index of the local quantum state of (4.6), while σ and σ' are (non physical) *virtual* or *bond* indices. The key idea behind MPS is that the entanglement structure of many-body quantum states can be efficiently captured by connecting these tensors through their virtual indices. Thus the many-body wave-function (4.6) internal information can be encoded and compressed as follows:

$$\Psi_{\alpha_1\alpha_2\dots\alpha_L} \xrightarrow{\simeq} \Psi_{\alpha_1\alpha_2\dots\alpha_L}^{\text{MPS}} = \begin{array}{c} \psi_1 \text{---} \psi_2 \text{---} \psi_3 \text{---} \dots \text{---} \text{---} \text{---} \psi_L \\ | \quad | \quad | \quad \dots \quad | \quad | \quad | \\ \alpha_1 \quad \alpha_2 \quad \alpha_3 \quad \dots \quad \alpha_L \end{array} . \quad (4.10)$$

The dimension of the virtual indices is called the *bond dimension* χ , and it is a controllable computational parameter. The larger χ is, the larger is the *entanglement* the tensor network can encode, but of course the larger also the computational complexity of the matrix operations involved.

Thus, one can represent a generic quantum many-body state (4.8) as follows

$$|\Psi_{\text{MPS}}\rangle = \sum_{\alpha_1\dots\alpha_L} \Psi_{\alpha_1\alpha_2\dots\alpha_L}^{\text{MPS}} |\alpha_1\dots\alpha_L\rangle. \quad (4.11)$$

Obtaining an MPS (4.10) from a many-body wave-function (4.8) is possible using *Singular Value Decomposition* (SVD), a fundamental matrix factorization technique in linear algebra. Given a $n \times m$ matrix M , the SVD factorizes it into three separate matrices:

$$i \text{---} \boxed{M} \text{---} j = M_{ij} = U_{ik} \Sigma_{kl} V_{lj} = i \text{---} \boxed{U} \text{---} \boxed{\Sigma} \text{---} \boxed{V} \text{---} j, \quad (4.12)$$

where U and V are $n \times k$ and $k \times m$ *unitary matrices* respectively, and Σ is a $k \times k$ *diagonal* matrix containing the so-called *singular values* (generalized eigenvalues) of M in descending order. Smaller singular values can be neglected (set to zero), reducing the bond dimension of the matrices (of the internal indices).

Thus, the dimension of $\Psi_{\alpha_1\alpha_2\dots\alpha_L}^{\text{MPS}}$ can be reduced from $\mathcal{O}(d^L)$ to $\mathcal{O}(L\chi^2d)$ with SVD, i.e. the amount of information to store scales linearly with the system size using an MPS, which allows for an *exponential* compression information storage. The latter fact is true only if the bond dimension χ is fixed. The fact that (4.10) can faithfully represent (4.6) with χ fixed large enough is guaranteed by the *Area Law for the entanglement entropy* for 1-dimensional systems [32].

4.2.2 Matrix Product Operators

A Matrix Product Operator (MPO) is the analogous TN structure to represent 1-dimensional quantum many-body *operators*, as MPS represents 1-dimensional quantum many-body states. An MPO is constructed similarly to an MPS, where each site in the chain


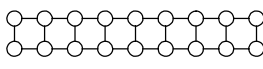
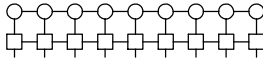
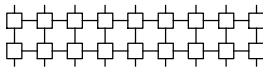
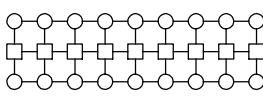
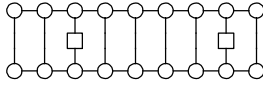
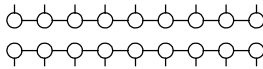
| | | |
|---|---|---|
| Separable (“Mean Field”) states | $ \psi_1\rangle \otimes \dots \otimes \psi_L\rangle =$ |  |
| Scalar products between states | $\langle \Psi \Phi \rangle =$ |  |
| Operators acting on states | $\hat{A} \Phi\rangle =$ |  |
| Operator products | $\hat{A}\hat{B} =$ |  |
| Expectation values | $\langle \Psi \hat{A} \Psi \rangle =$ |  |
| Correlators of local operators $\hat{\sigma}_j$ | $\langle \Psi \hat{\sigma}_i \hat{\sigma}_j \Psi \rangle =$ |  |
| Density matrices of pure states | $ \Psi\rangle\langle\Psi =$ |  |

Table 4.1. A comprehensive overview of the most relevant operations involving MPS and MPOs, which allows the manipulation of quantum many-body systems.

corresponds to a tensor. In particular, each tensor describes a local operator acting on each site:

$$A_{j,\alpha_j\beta_j}^{\sigma\sigma'} = \sigma \begin{array}{c} \beta_j \\ | \\ \boxed{A_j} \\ | \\ \alpha_j \end{array} \sigma', \quad (4.13)$$

Using SVD from a generic many-body operator one can obtain the following MPO tensor network structure

$$A_{\alpha_1 \dots \alpha_L}^{\beta_1 \dots \beta_L} \xrightarrow{\text{SVD}} (A_{\text{MPO}})_{\alpha_1 \alpha_2 \dots \alpha_L}^{\beta_1 \dots \beta_L} = \begin{array}{c} \beta_1 \quad \beta_2 \quad \beta_3 \quad \dots \quad \beta_L \\ | \quad | \quad | \quad \dots \quad | \\ \boxed{A_1} - \boxed{A_2} - \boxed{A_3} - \dots - \boxed{} - \boxed{} - \boxed{A_L} \\ | \quad | \quad | \quad \dots \quad | \\ \alpha_1 \quad \alpha_2 \quad \alpha_3 \quad \dots \quad \alpha_L \end{array}. \quad (4.14)$$

in such a way one can represent many-body state compressing information from $\mathcal{O}(d^{2L})$ to $\mathcal{O}(L\chi^2 d^2)$, representing many-body operators with the so-called MPO Ansatz:

$$\hat{A}_{\text{MPO}} = \sum_{\alpha_1 \dots \alpha_L} A_{\alpha_1 \dots \alpha_L}^{\beta_1 \dots \beta_L} |\alpha_1 \dots \alpha_L\rangle \langle \beta_1 \dots \beta_L|. \quad (4.15)$$

Using MPS and MPO one can perform most of the *crucial* operations to analyze quantum systems, such as scalar products between MPS states and computing expectation values of MPO operators (Tab. 4.1).

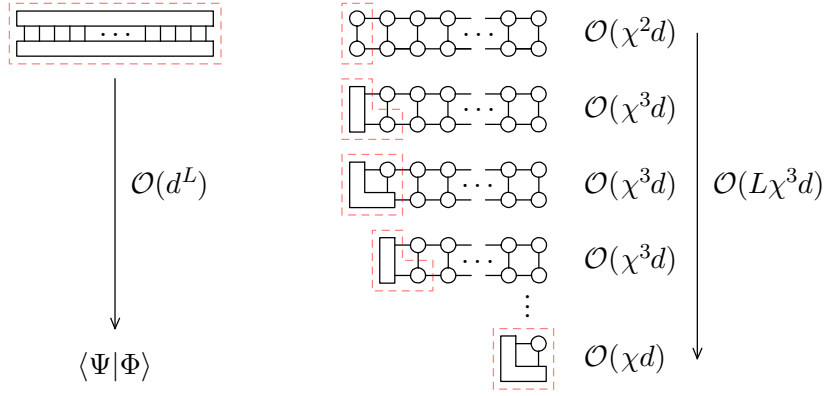


Figure 4.1. Here the significant advantage of computing scalar products between MPS (right) compared to the scalar product between non-decomposed quantum states (left) is shown. The scalar product calculations for complete quantum states scales as $\mathcal{O}(d^L)$, and becomes computationally impractical for large quantum systems.

It is possible to show [57] that there is a way to *contract* these TN structures in such a way to obtain an *exponential* advantage to compute quantities such as scalar products and expectation values (Fig 4.1). More precisely, the contractions of these TN structures scales *linearly* with the system size L , while the same contractions of the whole many-body matrices scales *exponentially* with L . This fact represents the main advantage of TNs and the power of MPS and MPO structures.

4.2.3 The Matrix picture

In order to write explicitly the entries of the local tensors of an MPS and MPO, we can use the so-called *matrix picture* for local tensors.

In particular, for an MPS with bond dimension χ , we write a local tensor $\psi_\alpha^{\sigma\sigma'}$ as a $\chi \times \chi$ matrix, with σ, σ' as the indices of this matrix, and α as the index of the vectors, which are the entries of this matrix. The final result is a matrix of vectors:

$$\psi_\alpha^{\sigma\sigma'} = \sigma \text{---} \begin{array}{c} \circ \\ \psi \\ \circ \end{array} \text{---} \sigma' = \begin{pmatrix} \psi_\alpha^{11} & \dots & \psi_\alpha^{1\chi} \\ \vdots & \ddots & \vdots \\ \psi_\alpha^{\chi 1} & \dots & \psi_\alpha^{\chi\chi} \end{pmatrix}. \quad (4.16)$$

For a *translationally invariant state*, (e.g. the ground-state of the 1-dimensional Lattice QED on a ladder) apart from the initial and final tensors of the chain ψ_i and ψ_f , all the bulk tensors ψ_b are the same, so that an MPS reads

$$\Psi_{\text{MPS}} = \begin{array}{c} \circ \text{---} \circ \text{---} \circ \text{---} \circ \text{---} \circ \text{---} \circ \text{---} \circ \text{---} \circ \text{---} \circ \\ \psi_i \underbrace{\psi_b \psi_b \dots \psi_b}_{L-2} \psi_b \psi_f. \end{array} \quad (4.17)$$

where all these tensors are contracted with a *matrix product*, where the product between entries is the tensor product \otimes . To clarify the previous notation, we give some examples.

Let's suppose that we want to represent the following many-body state

$$|\Psi\rangle = |00\dots 0\rangle + |11\dots 1\rangle \quad (4.18)$$

as an MPS, where the computational local basis is $\{|0\rangle, |1\rangle\}$. Following the previous conventions, if we define

$$\psi_i = \begin{array}{c} \circ \\ | \\ \text{---} \end{array} = (|0\rangle \ |1\rangle), \quad \psi_b = \begin{array}{c} \text{---} \\ | \\ \circ \end{array} = \begin{pmatrix} |0\rangle & 0 \\ 0 & |1\rangle \end{pmatrix}, \quad \psi_f = \begin{array}{c} \text{---} \\ | \\ \circ \end{array} = \begin{pmatrix} |0\rangle \\ |1\rangle \end{pmatrix} \quad (4.19)$$

we notice that, for instance, contracting three tensors as previously described, we obtain an MPS of three sites, and if we contract these three tensors we obtain exactly the many-body state we want to represent:

$$\psi_i \psi_b \psi_b \psi_b \psi_f = |000\rangle + |111\rangle. \quad (4.20)$$

It is simple to show that same holds for n sites, reconstructing the state (4.18). In this case, the tensor ψ_b is a 2×2 matrix in the virtual index, so we need a bond dimension $\chi = 2$ to represent the state (4.18).

A more complex example is the following:

$$|\Psi\rangle = |000000\dots\rangle + |101010\dots\rangle \quad (4.21)$$

One can check that this state can be represented as an MPS using the following local tensors:

$$\psi_b = \begin{array}{c} \text{---} \\ | \\ \circ \end{array} = \begin{pmatrix} |0\rangle & 0 & 0 \\ 0 & 0 & |0\rangle \\ 0 & |1\rangle & 0 \end{pmatrix}, \quad (4.22)$$

$$\psi_i = \begin{array}{c} \circ \\ | \\ \text{---} \end{array} = (|0\rangle \ |1\rangle \ 0), \quad \psi_f = \begin{array}{c} \text{---} \\ | \\ \circ \end{array} = \begin{pmatrix} |0\rangle \\ |0\rangle \\ |1\rangle \end{pmatrix}. \quad (4.23)$$

The same notation can be used for MPOs. Indeed each local tensor can be represented as a matrix of operators (a matrix of matrices):

$$A_{\alpha\beta}^{\sigma\sigma'} = \begin{array}{c} \beta_j \\ | \\ \square \\ | \\ \alpha \end{array} \begin{array}{c} \sigma \\ \text{---} \end{array} \begin{array}{c} \text{---} \\ \sigma' \end{array} = \begin{pmatrix} A_{\alpha\beta}^{11} & \cdots & A_{\alpha\beta}^{1\chi} \\ \vdots & \ddots & \vdots \\ A_{\alpha\beta}^{\chi 1} & \cdots & A_{\alpha\beta}^{\chi\chi} \end{pmatrix}. \quad (4.24)$$

Hence, we can represent an MPO analogously to

$$A_{\text{MPO}} = \begin{array}{c} \square \square \square \square \square \square \square \square \square \\ | \quad | \quad | \quad | \quad | \quad | \quad | \quad | \quad | \\ \text{---} \end{array} = A_i \underbrace{A_b A_b \dots A_b A_b}_{L-2} A_f \quad (4.25)$$

where the matrix product implements \otimes as product between entries.

For instance, if we have the following operator

$$\hat{A} = \hat{\sigma}^x \otimes \dots \otimes \hat{\sigma}^x + \hat{\sigma}^y \otimes \dots \otimes \hat{\sigma}^y + \hat{\sigma}^z \otimes \dots \otimes \hat{\sigma}^z \quad (4.26)$$

we can use as local tensors the following Ansatz:

$$A_b = \begin{array}{c} \square \\ \vdash \end{array} = \begin{pmatrix} \hat{\sigma}^x & 0 & 0 \\ 0 & \hat{\sigma}^y & 0 \\ 0 & 0 & \hat{\sigma}^z \end{pmatrix}, \quad (4.27)$$

$$A_i = \begin{array}{c} \square \\ \vdash \end{array} = (\hat{\sigma}^x \ \hat{\sigma}^y \ \hat{\sigma}^z), \quad A_f = \begin{array}{c} \square \\ \vdash \end{array} = \begin{pmatrix} \hat{\sigma}^x \\ \hat{\sigma}^y \\ \hat{\sigma}^z \end{pmatrix}. \quad (4.28)$$

However, how can we, in general, guess an MPO Ansatz of the form (4.27) from a given definition of the operator \hat{A} ? If the definition of \hat{A} is sum of compositions of local operators, an efficient method is the *Automata picture*.

4.2.4 The Automata picture

An *automaton* (plural: *automata*) refers to a mathematical model of computation that operates on an input according to a predefined set of *rules*. Automata can be represented as abstract machines or graphs, where each state represents a configuration, and transitions between states correspond to the application of rules.

In the context of TNs, automata can be used to efficiently represent and manipulate MPS and MPOs formed by sum of compositions of local operators [58]. Indeed, constructing MPS and MPO from the automata picture is more intuitive rather than from the matrix picture.

We can set the following graphical rule to construct an automaton which represents an MPS:

- **automata states:** each *node* of the automaton graph is a *state*; the total number of states in an automaton corresponds to the *bond dimension* of the local operators of an MPS; each state is labelled with an integer number $1, 2, 3, \dots$, which represents a value of the virtual indices σ, σ' of the MPS;
- **input transitions:** each node can have an *input* transition, which is represented as an arrow from nothing to a node; to this kind of arrow is associated an *initial local state*, which an entry of the matrix ψ_i of (4.17);
- **output transitions:** each node can have an *output* transition, which is represented as an arrow from a node to nothing; to this kind of arrow is associated a *final local state*, which an entry of the matrix ψ_f of (4.17);
- **transitions between two states:** a transition between two states is represented with an arrow from a state σ to another state σ' ; a transition increases the position of the chain of states, and to each transition is associated a local state, which is the entry $\psi_\alpha^{\sigma\sigma'}$ of the local tensor in an MPS; a transition can also be from a state to itself.

The same rules are valid with MPOs, using operators instead of states for each transition. To clarify these rules, we analyze some examples.

Suppose to have three local states $|1\rangle, |2\rangle, |3\rangle$, and suppose we want to represent the sum of the three states $|\dots 111 \dots\rangle, |\dots 222 \dots\rangle, |\dots 333 \dots\rangle$ of an (infinite) chain as an MPS.

Indeed in this case, we need three states 1, 2, 3 and each of them are linked to itself with a transition as follows:

$$|\dots 111\dots\rangle + |\dots 222\dots\rangle + |\dots 333\dots\rangle \rightarrow \begin{array}{ccc} \boxed{1} & \boxed{2} & \boxed{3} \\ \text{loop}_{|1\rangle} & \text{loop}_{|2\rangle} & \text{loop}_{|3\rangle} \end{array} \rightarrow \begin{pmatrix} |1\rangle & 0 & 0 \\ 0 & |2\rangle & 0 \\ 0 & 0 & |3\rangle \end{pmatrix}. \quad (4.29)$$

This for an *infinite* chain. If we want to stop the chain we need to insert input and output transitions:

$$\begin{aligned} |11\dots 1\rangle + |22\dots 2\rangle + |33\dots 3\rangle &\rightarrow \begin{array}{ccc} |1\rangle \rightarrow \boxed{1} \rightarrow |1\rangle & |2\rangle \rightarrow \boxed{2} \rightarrow |2\rangle & |3\rangle \rightarrow \boxed{3} \rightarrow |3\rangle \\ \text{loop}_{|1\rangle} & \text{loop}_{|2\rangle} & \text{loop}_{|3\rangle} \end{array} \\ &\rightarrow (|1\rangle \ |2\rangle \ |3\rangle) \begin{pmatrix} |1\rangle & 0 & 0 \\ 0 & |2\rangle & 0 \\ 0 & 0 & |3\rangle \end{pmatrix}^{L-2} \begin{pmatrix} |1\rangle \\ |2\rangle \\ |3\rangle \end{pmatrix}. \end{aligned} \quad (4.30)$$

The two cases (4.29) and (4.30) would have probably been constructed using only the matrix picture discussed in the previous section, so in the following we discuss more involving examples.

As said, the automata procedure is very efficient for Hamiltonians defined in terms of local operators. The automaton of the *Ising model with transverse field* Hamiltonian can be represented using an automaton of only three states, hence, with an MPS with bond dimension $\chi = 3$:

$$\hat{H} = \sum_j \hat{\sigma}_j^z \hat{\sigma}_{j+1}^z + \lambda \hat{\sigma}_j^x \rightarrow \begin{array}{ccc} & \lambda \hat{\sigma}^x & \\ \text{loop}_{\mathbb{I}} \uparrow & \boxed{1} \xrightarrow{\hat{\sigma}^z} \boxed{2} \xrightarrow{\hat{\sigma}^z} \boxed{3} & \downarrow \text{loop}_{\mathbb{I}} \\ & & \end{array} \rightarrow \begin{pmatrix} \mathbb{I} & \hat{\sigma}^z & \lambda \hat{\sigma}^x \\ 0 & 0 & \hat{\sigma}^z \\ 0 & 0 & \mathbb{I} \end{pmatrix}. \quad (4.31)$$

Another interesting example of complex Hamiltonian which can be represented with a bond dimension $\chi = 3$ MPO is the two-body Hamiltonian with an *exponentially decreasing interaction* strength as a function of the distance:

$$\hat{H} = \sum_r \sum_j \lambda^{-r} \hat{X}_j \hat{X}_{j+r} \rightarrow \begin{array}{ccc} & \hat{X} & \\ \text{loop}_{\mathbb{I}} \uparrow & \boxed{1} \xrightarrow{\hat{X}} \boxed{2} \xrightarrow{\hat{X}} \boxed{3} & \downarrow \text{loop}_{\mathbb{I}} \\ & & \end{array} \rightarrow \begin{pmatrix} \mathbb{I} & \hat{X} & 0 \\ 0 & \mathbb{I}/\lambda & \hat{X} \\ 0 & 0 & \mathbb{I} \end{pmatrix}. \quad (4.32)$$

The last example we give is the Hamiltonian of the *Heisenberg Model*. For this system, an automata of 5 states, i.e. a MPS with bond dimension $\chi = 5$ local tensors is needed:

$$\begin{aligned} \hat{H} &= \sum_j J_x \hat{\sigma}_j^x \hat{\sigma}_{j+1}^x + J_y \hat{\sigma}_j^y \hat{\sigma}_{j+1}^y + J_z \hat{\sigma}_j^z \hat{\sigma}_{j+1}^z \\ &\rightarrow \begin{array}{ccccc} & & \boxed{2} & & \\ & J_x \hat{\sigma}^x & \nearrow & \hat{\sigma}^x & \\ \text{loop}_{\mathbb{I}} \uparrow & \boxed{1} & \xrightarrow{J_z \hat{\sigma}^z} & \boxed{3} & \xrightarrow{\hat{\sigma}^z} & \boxed{5} & \downarrow \text{loop}_{\mathbb{I}} \\ & & \searrow & \hat{\sigma}^z & \\ & J_z \hat{\sigma}^z & \downarrow & \hat{\sigma}^z & \end{array} \rightarrow \begin{pmatrix} \mathbb{I} & \hat{\sigma}^x & \hat{\sigma}^y & \hat{\sigma}^z & 0 \\ 0 & 0 & 0 & 0 & \hat{\sigma}^x \\ 0 & 0 & 0 & 0 & \hat{\sigma}^y \\ 0 & 0 & 0 & 0 & \hat{\sigma}^z \\ 0 & 0 & 0 & 0 & \mathbb{I} \end{pmatrix}. \end{aligned} \quad (4.33)$$

The previous examples involve only Hamiltonian, however *every many-body operator* defined in terms of sum of compositions of local states can be represented as an MPO using this procedure. Of course, the bond dimension can increase according to the complexity of the pattern of local operators in the definition of the many-body operator.

4.3 Density Matrix Renormalization Group

The *Density Matrix Renormalization Group* (DMRG) [59] is a powerful numerical technique used to study the ground-state properties of strongly correlated quantum many-body systems, and particularly suitable for one-dimensional chains or lattices. Inspired by the *Real Space Renormalization Group* ideas of Kadanoff [60] and Wilson [61], it was originally developed by Steven R. White [59] and later improved and adapted to TNs structures [62, 63]. The original implementation of DMRG uses *density matrices* to identify and isolate the most relevant quantum configurations with minimum energy.

Given a quantum Hamiltonian \hat{H} of a 1-dimensional state, the problem consists in finding the ground-state MPS with the Hamiltonian written in an MPO form, which is the following eigenvalue problem with TNs:

$$\begin{array}{cccccccc} \circ & \circ & \circ & \circ & \circ & \circ & \circ & \circ \\ | & | & | & | & | & | & | & | \\ \square & \square & \square & \square & \square & \square & \square & \square \\ | & | & | & | & | & | & | & | \\ \circ & \circ & \circ & \circ & \circ & \circ & \circ & \circ \end{array} = \mathcal{E} \begin{array}{cccccccc} \circ & \circ & \circ & \circ & \circ & \circ & \circ & \circ \\ | & | & | & | & | & | & | & | \\ \circ & \circ & \circ & \circ & \circ & \circ & \circ & \circ \end{array}. \quad (4.34)$$

The core idea behind DMRG is to optimize the representation of the quantum state *iteratively*, with a renormalizing coarse-graining procedure: initially, a small system is constructed, and then the method systematically adds sites to the chain, optimizing the state at each step using numerical techniques such as matrix diagonalization or variational methods. By iteratively increasing the system size DMRG gradually includes longer-range correlations and improves the approximation of the true quantum interacting ground-state.

However, the MPS adaptation of DMRG algorithm (MPS-DMRG) is more technical. The Hamiltonian \hat{H} must have certain simplifying properties, such as being in MPO form. In the following, we just give a brief summary of the main steps (Fig. 4.2):

- a) **setup**: the initial (random) MPS is transformed into an *orthogonal form* with a *gauging*^{4.3} procedure; the MPO form of \hat{H} is then projected into a new basis; a first pair of MPS tensors are contracted to a two-index bond tensor over their shared bond index;
- b) **optimization of first bond**: the first bond tensor is optimized using iterative algorithms such as Davidson or Lanczos [64]: the multiplication of the Hamiltonian H with the bond tensor is computed using the projected form of \hat{H} ;

4.3. In an MPS representation, the gauge freedom arises from the freedom to apply local unitary transformations to the virtual indices connecting neighboring tensors. These transformations do not change the physical state represented by the MPS. Gauging is the process of choosing a specific gauge condition to fix the gauge freedom in an MPS representation.

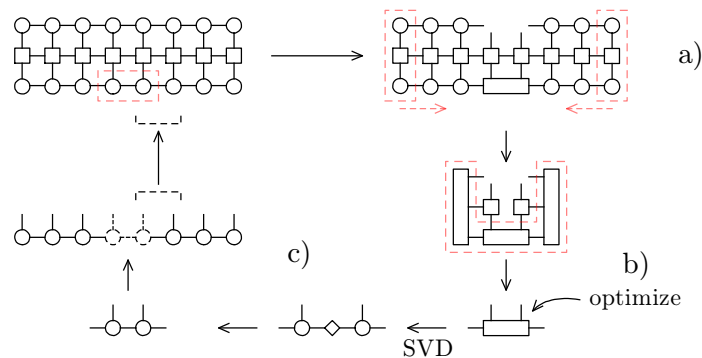


Figure 4.2. The MPS-DMRG algorithm cycle. The DMRG employs a series of iterative steps to systematically optimize and approximate the MPS representation, efficiently capturing the low-energy sectors of the quantum system Hilbert space.

- c) **adaptive restoration of MPS form:** the MPS form of the candidate eigenvector is restored using SVD of the bond tensor; the resulting MPS tensor is truncated to a desired bond dimension;
- d) **remaining steps and sweeping:** the steps a), b), c) are carried out for the MPS tensors sharing the next bond index pair, merging and improving them, and then restoring the MPS form; the optimization and adaptation steps are repeated for all the bond indices two at a time, performing a full *sweep*. The algorithm continues sweeping back and forth, optimizing the MPS tensors and adapting the bond dimensions until *convergence* is achieved.

DMRG is a sophisticated numerical algorithm, and manually implementing it from scratch can be quite involving. However, there are existing libraries and tools^{4.4} that provide DMRG functionality, allowing to use it as a pre-built function or module.

4.4 Time evolution of MPS

For *closed quantum systems*, the time evolution can be described by the Schrödinger equation. In the context of MPS, the time evolution of the state can be efficiently implemented using several algorithms which have been developed in recent years [65], some of which are:

- **t-DMRG** (Time-Evolving Density Matrix Renormalization Group) [66]: an extension of the DMRG algorithm for time evolution;
- **TEBD** (Time-Evolving Block Decimation) [67]: it approximates the time evolution operator using a sequence of local two-site unitary gates, which act on neighboring sites of the MPS tensor network;
- **TDVP** (Time-Dependent Variational Principle) [68]: it formulates the time evolution problem as a variational optimization problem; it updates the MPS tensors in a way that minimizes the distance between the time-evolved state and the original state under the time-dependent Hamiltonian.

^{4.4} For instance, the Julia package ITensor, or the Python library TenPy.

For the simulations of this thesis, we choose TEBD as a time evolution algorithm since it is enough efficient despite its simplicity of implementation. The central idea of TEBD is to approximate the time evolution operator using a *Trotter-Suzuki decomposition* [69] or some other suitable approximation. The time evolution is carried out in small time steps, and at each time step, local two-site unitary gates are applied to the MPS tensor network. The steps of the TEBD algorithm are the following:

- **preparation of the initial MPS state:** the TEBD algorithm starts with an initial MPS representation of the quantum state at time $t = 0$

$$|\Psi_0\rangle = \text{---} \circ \text{---} \circ \text{---} \circ \text{---} \circ \text{---} \circ \text{---} ; \quad (4.35)$$

- **Hamiltonian decomposition into gates:** the TEBD requires that the time-dependent Hamiltonian of the system can be decomposed into a sum of nearest-neighbor interaction terms, called two-site *gates*, each acting on neighboring sites of the MPS:

$$\hat{H} = \sum_j \hat{H}_{j,j+1} = \sum_j \left| \left| \begin{array}{c} | \\ | \\ \hline | \\ | \end{array} \right. \right| \hat{H}_{j,j+1} \left| \left| \begin{array}{c} | \\ | \\ \hline | \\ | \end{array} \right. \right| ; \quad (4.36)$$

- **exponentiation of the two-site gate:** exponentiate each of these two-site operators using a small time step τ , which gives us a two-site unitary time-evolution gate for each pair of neighboring sites:

$$\exp\left(-\frac{i}{2}\tau \hat{H}_{j,j+1}\right) = \exp\left(-\frac{i}{2}\tau \begin{array}{c} | \\ | \\ \hline | \\ | \end{array}\right) \equiv \begin{array}{c} \leftarrow \\ \leftarrow \\ \hline \leftarrow \\ \leftarrow \end{array} ; \quad (4.37)$$

- **decomposition of the time evolution operator:** the time evolution operator, which describes the system's evolution over a small time step τ , is obtained by applying the exponentiated two-site evolution gates (4.37) in a specific order; typically, a *Trotter-Suzuki decomposition* is used to approximate the time evolution operator as a product of these exponentiated gates:

$$\hat{U}(\tau) \simeq e^{-\frac{i}{2}\hat{H}_{1,2}\tau} e^{-\frac{i}{2}\hat{H}_{2,3}\tau} \dots e^{-\frac{i}{2}\hat{H}_{j,j+1}\tau} \dots e^{-\frac{i}{2}\hat{H}_{L-1,L}\tau} + \mathcal{O}(\tau^3); \quad (4.38)$$

hence, in TN notation, the time evolution operator is the application of all the two-site gates (4.37) in the order of (4.38):

$$\hat{U}(\tau) \simeq \begin{array}{c} \begin{array}{c} \leftarrow \\ \leftarrow \\ \hline \leftarrow \\ \leftarrow \end{array} \\ \leftarrow \\ \leftarrow \\ \hline \leftarrow \\ \leftarrow \\ \leftarrow \\ \leftarrow \\ \hline \leftarrow \\ \leftarrow \end{array} ; \quad (4.39)$$

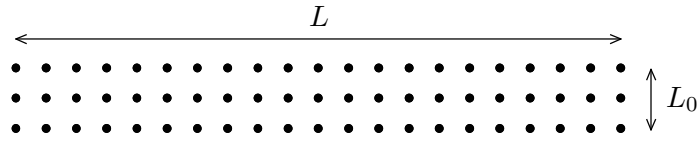


Figure 4.3. A quasi 1-dimensional lattice. The main size of the system is L , which is much larger than the width $L_0 \ll L$.

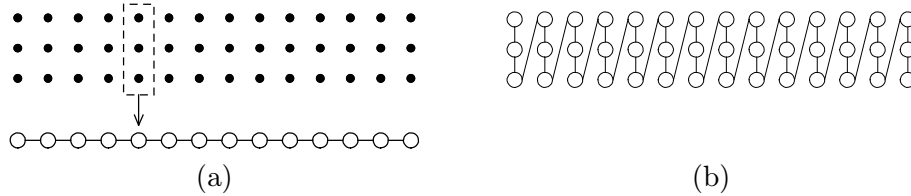


Figure 4.4. The two approaches to adapt an MPS to a quasi 1-dimensional system: a) Contraction of the smaller dimension: each column is a subsystem is mapped to a single tensor of the MPS. b) Rectification with a filling curve: in case of a strip or a tube, a “sawtooth” path can be chosen.

- **updating the state:** to evolve the MPS in time, apply the time-evolution operator to the MPS representation of the quantum state:

$$|\Psi(t + \tau)\rangle = \hat{U}(\tau)|\Psi(t)\rangle; \quad (4.40)$$

each iteration advances the quantum state in time by τ , and by repeating the steps starting from $|\Psi_0\rangle$, the time-evolved state $|\Psi(t)\rangle$ is obtained.

4.5 TNs for higher-dimensional systems

4.5.1 MPS for quasi one-dimensional systems

Quasi-one-dimensional systems refers to physical systems that possess the main degree of freedom in one-dimension, even though they may extend a bit into two or three dimensions. These systems (e.g. nanotubes, molecular chains, and so on) are of particular interest in condensed matter physics and materials science. Of course, our interest on these systems arise from the fact that the lattice system analyzed in this thesis is quasi-1-dimensional.

However, quasi-1-dimensional systems do not fit to the MPS Ansatz we already described, which allows to manipulate efficiently quantum many-body states naturally for 1-dimensional systems. Hence we need new approaches to adapt the MPS structure to a quasi-dimensional system.

We take as toy model a 2D lattice with L plaquettes along the x -axis (the main direction), and $L_0 \ll L$ plaquettes along the y axis (Fig. 4.3).

The two main approaches of adapting an MPS to this lattice are the following (Fig 4.4):

- **contraction of the smaller dimension** (Fig 4.4a): the first approach involves considering the $L \times L_0$ two-dimensional lattice as an L 1-dimensional system, grouping together all the L_0 sites of each column into a single numerical site; by doing this, the problem is transformed into a one-dimensional chain, allowing the appli-

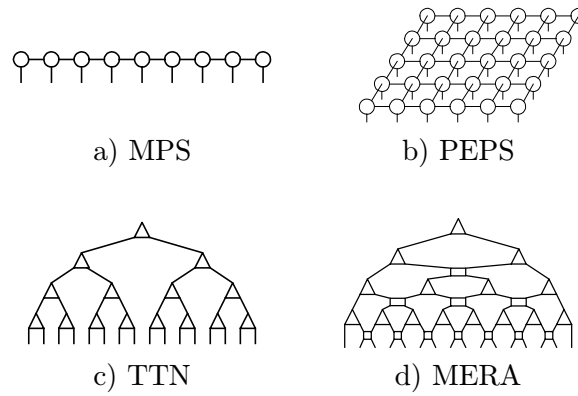


Figure 4.5. Comparison of four Tensor Network structures for quantum states representation: a) Matrix Product State b) Projected Entangled Pair State c) Tree Tensor Network and d) Multi-scale Entanglement Renormalization Ansatz. Each method offers unique ways to efficiently represent quantum states, addressing various dimensionalities and entanglement structures in quantum systems.

cation of one-dimensional algorithms; however, a limitation of this method is the exponential growth with L_0 of the local basis dimension, which restricts its application to quasi-two-dimensional systems, where L_0 becomes large;

- **rectification with a filling curve** (Fig 4.4b): the second strategy [70], involves covering the two-dimensional lattice with a one-dimensional curve (a chosen *path*) and applying one-dimensional algorithms to the resulting effective chain; this method induces a specific one-dimensional *site-ordering* in the 2D lattice, creating a mapping between the physical 2D system and the 1D chain; this mapping enables the translation of a two-dimensional model into a one-dimensional one; however, it should be noted that the original model's nearest-neighbor interactions may lead to long-range interactions, which can impact the numerical efficiency.

4.5.2 Other TN structures for higher-dimensional systems

While MPS have proven successful in capturing the entanglement structure of one-dimensional systems, higher-dimensional systems often require more sophisticated TN methods. This has led to the development of several novel TN structures also for two or higher dimensions (Fig. 4.5), some of which are listed in the following [33]:

1. **PEPS** (Projected Entangled Pair States) it is based on the idea of assigning a tensor to each lattice site, where the tensors encode the local correlations and entanglement with neighboring sites; however, due to *loops*, the contraction to compute scalar quantities remains computationally challenging;
2. **TTN** (Tree Tensor Networks): the tensors are organized in a hierarchical tree structure, capturing correlations and entanglement between distant lattice sites; this hierarchical organization provides an efficient description of ground states in systems with long-range interactions; the TTN structure is also employed for 1D system with periodic boundary conditions;

3. **MERA** (Multiscale Entanglement Renormalization Ansatz): proposed in [71], MERA is based on the idea of renormalization and coarse-graining, offering a powerful representation of quantum states by encoding short- and long-range correlations efficiently.

Chapter 5

Numerical Simulations

In this chapter, we apply the Tensor Network (TN) methods described in chapter 4 to analyze and study the Hamiltonian Lattice QED on ladder geometries described in chapter 2. In particular, we first apply MPS-DMRG to this system, which allows for the creation of the ground-state MPS of large system sizes ($L \sim 10^2$), approaching the thermodynamic limit $L \rightarrow \infty$. Secondly, we prepare initial photonic wave-packet MPS states using the MPO operator, simulating out-of-equilibrium processes like the photonic wave-packet propagation and the photon-photon scattering using time-evolution algorithms for MPS.

5.1 TN representations and ground-state search

5.1.1 Represent the system as an MPS: the local basis choice

Since the ladder is a quasi-one-dimensional geometry, in order to represent a quantum state of the ladder system as an MPS state, we need to use one of the methods described in section 4.5.1.



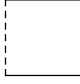
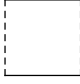
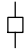
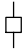
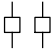
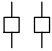
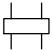
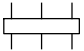
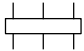
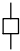
| Local basis | Rung | Super-plaquette | Semi-plaquette (any represent.) | Semi-plaquette case $\left(\frac{1}{2}, 1\right)$ |
|---|---|---|---|---|
| Local object |  |  |  |  |
| Local dimension | $\mathcal{O}(m_x^2 m_y)$ | $\mathcal{O}(m_x^2 m_y^2)$ | m_x^2 | $m_x^2 = 4$ |
| \hat{H}_j^E |  |  |  |  |
| \hat{H}_j^B |  |  |  |  |
| $\mathcal{H} = \mathcal{H}_{\text{phys}}$ | No | No | For a specific longit. polariz. sector | For a specific longit. polariz. sector |

Table 5.1. We list three possible choices of local bases to contract the smaller dimension of the ladder, representing the quasi-1D system as a 1D system. For each basis, the relative properties are listed, such as the local dimension and the form of the local Hamiltonian operators. With $m = 2s + 1$ we denote the spin multiplicity for a spin representation s . The condition $\mathcal{H} = \mathcal{H}_{\text{phys}}$ ensures that every possible configuration composed with that local basis is gauge invariant (i.e. allowed by Gauss' Law).

Contraction of the smaller ladder dimension. If we want to contract the smaller dimension, we need to choose a *local basis*. We list three of these bases for the ladder QED without matter (Tab. 5.1):

- **the rung basis:** in this basis the electric local operators are diagonal local operators; a single plaquette operator acts on two rungs, hence \hat{U}, \hat{U}^\dagger are 2-site operators;
- **the super-plaquette basis:** the electric local operators are still diagonal and local; a single plaquette operator acts also on the nearest neighboring plaquettes, hence \hat{U}, \hat{U}^\dagger are a 3-site operators;
- **the semi-plaquette basis:** this is the local basis we chose in section 2.2.2 to represent the system; in this basis \hat{U}, \hat{U}^\dagger are a 3-site operators but also \hat{E}_j^2 is non-local since to know a rung's electric field we need to know first the values of the horizontal electric fields of two neighboring plaquettes, thus:

$$\hat{E}_L = \left| \begin{array}{|c|} \hline \square \\ \hline \end{array} \right| \left| \begin{array}{|c|} \hline \square \\ \hline \end{array} \right|, \quad \hat{E}_T = \left| \begin{array}{|c|} \hline \square \\ \hline \end{array} \right|, \quad \hat{E}_B = \left| \begin{array}{|c|} \hline \square \\ \hline \end{array} \right|, \quad \hat{E}_R = \left| \begin{array}{|c|} \hline \square \\ \hline \end{array} \right| \left| \begin{array}{|c|} \hline \square \\ \hline \end{array} \right|; \quad (5.1)$$

however, the local operators in this basis becomes simpler in the $\left(\frac{1}{2}, 1\right)$ spin representation; moreover, in the lowest spin representation all the configuration spanned by the local basis are gauge invariant configurations, so the total Hilbert space \mathcal{H} is the physical Hilbert space $\mathcal{H}_{\text{phys}}$.

Rectification with a sawtooth curve. Another approach is the rectification of the system using a filling sawtooth curve (Fig. 5.1). This method results efficient for higher spin representation because the plaquette operator can be always expressed as a tensor product of local operators:

$$\hat{U} = \begin{array}{|c|} \hline \square \\ \hline \square \\ \hline \square \\ \hline \square \\ \hline \end{array} . \quad (5.2)$$

However, for the particular $\left(\frac{1}{2}, 1\right)$ spin representation case, the semi-plaquette basis is still a more advantageous choice since:

- the local dimension of the filling curve ($d \geq 2$) is the same or even higher than the one of $s_{\parallel}^z = 0$ polarization sector in the semi-plaquette basis ($d = 2$);
- for the filling curve it holds $\mathcal{H}_{\text{phys}} \subset \mathcal{H}$, while for the MPS in the semi-plaquette basis $\mathcal{H}_{\text{phys}} = \mathcal{H}$;
- the number of sites of the filling curve is $3L + 1$, which is triple with respect the one of the system in the plaquette basis, which is L .

Hence, from now on we will analyze the simplest case: we will consider the MPS representation of the system in the semi-plaquette basis, for the lowest spin representation $\left(\frac{1}{2}, 1\right)$.

5.1.2 The total and local Hamiltonian MPOs for $\left(\frac{1}{2}, 1\right)$

In order to represent the QLM Hamiltonian of the QED on ladder geometry

$$\hat{H} = \frac{g^2}{2a} \sum_j (\hat{S}_j^z)^2 + \frac{1}{2ag^2} \sum_j (\hat{U}_j + \hat{U}_j^\dagger) \quad \text{with} \quad \hat{U} \equiv \hat{S}_B^+ \hat{S}_R^+ \hat{S}_T^- \hat{S}_L^-, \quad (5.3)$$

in the lowest spin representation as an MPO we choose the semi-plaquette basis (Tab. 5.1). As we saw in section 2.6, this system is mappable into the Ising model transverse field, for which we already found an MPO representation (4.31) in section 4.2.4:

$$\hat{H} = \underbrace{\begin{array}{|c|} \hline \square \\ \hline \square \\ \hline \square \\ \hline \square \\ \hline \end{array} \dots \begin{array}{|c|} \hline \square \\ \hline \square \\ \hline \square \\ \hline \square \\ \hline \end{array}}_{L \sim 10^2 \text{ sites}} . \quad (5.4)$$

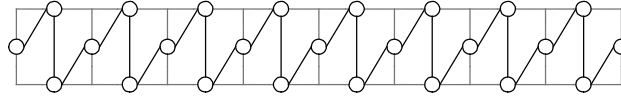


Figure 5.1. In order to adapt the ladder geometry to a linear MPS geometry, a possible approach is using a filling sawtooth curve represented here.

We notice that even in the lowest $\left(\frac{1}{2}, 1\right)$ spin representation, the *local Hamiltonian* (defined as (2.58)) representation as an MPO is a 3-sites operator:

$$\begin{aligned}
 \hat{H}_j &= \frac{g^2}{2a} \left(\frac{1}{2} \hat{E}_{L,j}^2 + \hat{E}_{T,j}^2 + \hat{E}_{B,j}^2 + \frac{1}{2} \hat{E}_{R,j}^2 \right) + \frac{1}{2ag^2} (\hat{U}_j + \hat{U}_j^\dagger) \\
 &= \left(\frac{1}{2} \begin{array}{|c|} \hline \square \square \\ \hline \end{array} + \begin{array}{|c|} \hline \square \\ \hline \end{array} + \begin{array}{|c|} \hline \square \\ \hline \end{array} + \frac{1}{2} \begin{array}{|c|} \hline \square \square \\ \hline \end{array} \right) + \begin{array}{|c|} \hline \square \\ \hline \end{array} \\
 &= \begin{array}{|c|} \hline \square \square \square \\ \hline \end{array} \xrightarrow{\text{SVD}} \begin{array}{|c|} \hline \square \square \square \\ \hline \end{array}.
 \end{aligned} \tag{5.5}$$

Thus, given a generic MPS state

$$|\Psi\rangle = \circ - \circ - \circ - \circ - \circ - \circ - \circ - \circ - \circ - \circ - \circ - \circ - \circ - \circ - \circ, \tag{5.6}$$

we can efficiently compute the local energy density of an MPS $|\Psi\rangle$ as the following contraction:

$$\mathcal{E}_j[\Psi] = \langle \Psi | \hat{H}_j | \Psi \rangle = \begin{array}{c} \circ - \circ - \circ - \circ - \circ - \circ - \circ - \circ - \circ - \circ - \circ - \circ - \circ - \circ - \circ \\ | \quad | \quad | \quad | \quad | \quad | \quad | \quad | \quad | \quad | \quad | \quad | \quad | \quad | \\ \circ - \circ - \circ - \circ - \circ - \circ - \circ - \circ - \circ - \circ - \circ - \circ - \circ - \circ - \circ \end{array} \tag{5.7}$$

5.1.3 Ground-state search with MPS-DMRG

In order to find the ground-state of the system, we can use built-in subroutines from the Tensor Network libraries of ITensor or TenPy which supports the MPS-DMRG described in section 5.1.3. The input of these functions are the following:

- an *initial* MPS, that we can choose with random entries:

$$|\text{Random MPS}\rangle = \underbrace{\circ - \circ - \circ - \circ - \circ - \circ - \circ - \cdots - \circ - \circ - \circ - \circ - \circ - \circ}_{L \sim 10^2 \text{ sites}}; \tag{5.8}$$

- the MPO form (5.4) of the *Hamiltonian* of the system, which we already discussed in the previous section;

- a total number of DMRG *sweeps* n_s that the algorithm will perform; alternatively, we can also choose a modality for which the algorithm continues sweeping until a certain threshold of convergence, i.e. the relative difference of the ground state energy after a sweep and the previous $|\mathcal{E}_n - \mathcal{E}_{n-1}|/\mathcal{E}_n$ is below a certain threshold $\eta \sim 10^{-10}$;
- the SVD cutoff $\epsilon \sim 10^{-10}$ under which the singular values are neglected and set to zero, reducing the bond dimension.

The output algorithm is the MPS representation of the ground-state (the dressed vacuum) of the system

$$|\Omega\rangle = \bigcirc - \bigcirc - \bigcirc - \bigcirc - \bigcirc - \bigcirc - \cdots - \bigcirc - \bigcirc - \bigcirc - \bigcirc - \bigcirc . \quad (5.9)$$

As a check of DMRG, one can verify that for low values of the coupling g , the expectation value of the energy of the ground-state is near to the known theoretical value:

$$\langle \Omega | \hat{H} | \Omega \rangle = \begin{array}{c} \bigcirc - \bigcirc - \bigcirc - \bigcirc - \bigcirc - \bigcirc - \cdots - \bigcirc - \bigcirc - \bigcirc - \bigcirc - \bigcirc \\ \square - \square - \square - \square - \square - \square - \cdots - \square - \square - \square - \square - \square \\ \bigcirc - \bigcirc - \bigcirc - \bigcirc - \bigcirc - \bigcirc - \cdots - \bigcirc - \bigcirc - \bigcirc - \bigcirc - \bigcirc \end{array} = -\frac{L}{ag^2} \cdot (1 + \mathcal{O}(g^4)). \quad (5.10)$$

5.2 MPO wave-packet operator construction for $(\frac{1}{2}, 1)$

In this section, we exploit the TN methods of section 4.2 to construct the MPO representation of the Wannier excitation operator (3.72) and of a generic wave-packet operator (3.106). This step is crucial because it allows us to prepare initial single-particle photonic wave-packet states, which are the initial condition of the processes that we will simulate in section 5.3.

In particular, we want to represent as an MPO the wave-packet creation operator

$$\hat{\Psi} \equiv \sum_j \Psi_j \hat{W}_j = \sum_j \sum_\alpha c_\alpha \Psi_j \hat{A}_{\alpha,j}. \quad (5.11)$$

where Ψ_j is the wave-packet wave-function profile (i.e. Gaussian function of j and momenta with rotating phase e^{ikj}), \hat{W}_j is the Wannier excitation operators of the site j , and c_α are the coefficients defined in (3.80). The operators $\hat{A}_{\alpha,j}$ are the operators which creates the Wannier \hat{W}_j , which are compositions of plaquette operators $\hat{U}_j, \hat{U}_j^\dagger$. As described in section 3.3.6, for the lowest spin representation, once chosen the number w of plaquettes of the Wannier support, the set of \hat{A}_α is the $w = 2^L$ operators.

5.2.1 Example of automata picture for $\hat{\Psi}$ with $w = 3$

Since the \hat{A}_α are compositions of k -local operators, we can exploit the automata picture described in section 4.2.4.

With a support of $w = 3$ plaquettes there are $2^3 = 8$ operators \hat{A} , hence the Wannier operator can be written as the follows:

$$\begin{aligned} \hat{W}_j^{w=3} = & c_1 \mathbb{I} + c_2 \hat{U}_{j+1} + c_3 \hat{U}_j + c_4 \hat{U}_j \hat{U}_{j+1} \\ & + c_5 \hat{U}_{j-1} + c_6 \hat{U}_{j-1} \hat{U}_{j+1} + c_7 \hat{U}_{j-1} \hat{U}_j + c_8 \hat{U}_{j-1} \hat{U}_j \hat{U}_{j+1}. \end{aligned} \quad (5.12)$$

Hence, the most general MPO wave-packet operator obtainable from (5.12) is:

$$\begin{aligned} \hat{\Psi}_{\text{MPO}}^{w=3} = & \sum_j \beta_j^{(1)} \mathbb{I}_j + \sum_j \beta_j^{(2)} \hat{U}_j + \sum_j \beta_j^{(3)} \hat{U}_j \hat{U}_{j+1} \\ & + \sum_j \beta_j^{(4)} \hat{U}_j \hat{U}_{j+2} + \sum_j \beta_j^{(5)} \hat{U}_j \hat{U}_{j+1} \hat{U}_{j+2}. \end{aligned} \quad (5.13)$$

The goal now is to find the coefficients β_j which represents a wave-packet $\hat{\Psi}(\bar{j}, \bar{p}, \sigma)$ centered in \bar{j} , with average momentum k and spatial dispersion σ :

$$\hat{\Psi}(\bar{j}, k, \sigma) = \sum_j \Psi_j \hat{W}_j^{w=3}, \quad \Psi_j \equiv e^{ikj} e^{-\frac{(j-\bar{j})^2}{2\sigma^2}}. \quad (5.14)$$

Keeping Ψ_j as generic coefficients, we substitute (5.12) inside (5.11) obtaining

$$\begin{aligned} \hat{\Psi}^{w=3}(\bar{j}, k, \sigma) = & \sum_j \Psi_j c_1 + \sum_j \Psi_j c_5 \hat{U}_{j-1} + \sum_j \Psi_j c_2 \hat{U}_{j+1} + \sum_j \Psi_j c_3 \hat{U}_j \\ & + \sum_j \Psi_j c_4 \hat{U}_j \hat{U}_{j+1} + \sum_j \Psi_j c_6 \hat{U}_{j-1} \hat{U}_{j+1} \\ & + \sum_j \Psi_j c_7 \hat{U}_{j-1} \hat{U}_j + \sum_j \Psi_j c_8 \hat{U}_{j-1} \hat{U}_j \hat{U}_{j+1}. \end{aligned} \quad (5.15)$$

Now, shifting the indices and grouping all the common terms we obtain

$$\begin{aligned} \hat{\Psi}^{w=3}(\bar{j}, k, \sigma) = & \sum_j \Psi_j c_1 + \sum_j (\Psi_{j-1} c_2 + \Psi_j c_3 + \Psi_{j+1} c_5) \hat{U}_j \\ & + \sum_j (\Psi_j c_4 + \Psi_{j+1} c_7) \hat{U}_j \hat{U}_{j+1} + \sum_j \Psi_{j+1} c_6 \hat{U}_j \hat{U}_{j+2}, \\ & + \sum_j \Psi_{j+1} c_8 \hat{U}_j \hat{U}_{j+1} \hat{U}_{j+2}, \end{aligned} \quad (5.16)$$

from which we identify the coefficients β_j as

$$\begin{aligned} \beta_j^{(1)} &= \Psi_j c_1; \\ \beta_j^{(2)} &= \Psi_{j-1} c_2 + \Psi_j c_3 + \Psi_{j+1} c_5; \\ \beta_j^{(3)} &= \Psi_j c_4 + \Psi_{j+1} c_7; \\ \beta_j^{(4)} &= \Psi_{j+1} c_6; \\ \beta_j^{(5)} &= \Psi_{j+1} c_8. \end{aligned}$$

Hence, we know all the β_j coefficients as a function of the sites of the MPO. Using an automata picture, it is straightforward to derive from (5.13) the j -th site tensor of the MPO as:

$$\hat{\Psi}_j^{\text{MPO}} = \begin{array}{c} \begin{array}{c} \beta_j^{(5)}\hat{U} \\ \downarrow \\ \begin{array}{c} \beta_j^{(4)}\hat{U} \quad \boxed{4} \xrightarrow{\mathbb{I}} \boxed{3} \xleftarrow{\hat{U}} \boxed{5} \\ \beta_j^{(3)}\hat{U} \quad \downarrow \hat{U} \\ \beta_j^{(2)}\hat{U} \quad \boxed{2} \xrightarrow{\mathbb{I}} \boxed{6} \xleftarrow{\mathbb{I}} \boxed{6} \\ \beta_j^{(1)}\hat{U} \quad \uparrow \hat{U} \\ \boxed{1} \xrightarrow{\beta_j^{(2)}\hat{U}} \boxed{2} \end{array} \\ \uparrow \mathbb{I} \end{array} \end{array} = \begin{pmatrix} \mathbb{I} & \beta_j^{(2)}\hat{U} & \beta_j^{(3)}\hat{U} & \beta_j^{(4)}\hat{U} & \beta_j^{(5)}\hat{U} & \beta_j^{(1)}\mathbb{I} \\ & 0 & & & & \mathbb{I} \\ & & 0 & & & \hat{U} \\ & & \mathbb{I} & 0 & & \\ & & \hat{U} & & 0 & \\ & & & & & 0 \end{pmatrix}. \quad (5.17)$$

Thus, the bond dimension to represent a wave-packet operator with Wannier support of $w = 3$ is $\chi = 6$ in the lowest spin representation.

5.2.2 Generalization to higher w and built-in functions methods

We can generalize the above procedure to higher values of the Wannier support w . Using the automata picture, one can show that the generalization of (5.17) for $w > 3$ is a dichotomic tree:

$$\Psi^{w=3} = \begin{array}{c} \square \\ \swarrow \quad \searrow \\ \square \quad \square \\ \swarrow \quad \searrow \\ \square \quad \square \quad \square \\ \swarrow \quad \searrow \\ \square \quad \square \quad \square \quad \square \end{array}, \quad \Psi^{w=4} = \begin{array}{c} \square \quad \square \quad \square \\ \swarrow \quad \searrow \\ \square \quad \square \\ \swarrow \quad \searrow \\ \square \quad \square \quad \square \\ \swarrow \quad \searrow \\ \square \quad \square \quad \square \quad \square \end{array}, \quad \Psi^{w=5} = \begin{array}{c} \square \quad \square \quad \square \quad \square \quad \square \\ \swarrow \quad \searrow \\ \square \quad \square \quad \square \\ \swarrow \quad \searrow \\ \square \quad \square \quad \square \quad \square \\ \swarrow \quad \searrow \\ \square \quad \square \quad \square \quad \square \quad \square \end{array}, \quad \dots \quad (5.18)$$

Here we have included also w even, but notice that only a w odd is used for a support with a centered Wannier state. Indeed, in this way the bond dimension of the MPO grows exponentially with the number of plaquettes in the support of the Wannier. More precisely:

$$\chi = 2^{w-1} + 2. \quad (5.19)$$

Since the automata description becomes difficult to implement by hand for high values of w , we also notice that some numerical frameworks like the ITensor library offer methods to generate automatically MPOs from sum of compositions of local operators. Often these methods also provide an automatic standard final compression routine of the tensors after the generation of the MPO. The compression reduces the bond dimension, which is always lower than (5.19). This results also in a variable bond dimension along the chain, depending on the local amount of entanglement stored by the operator.

5.3 Real-time simulations of the $(\frac{1}{2}, 1)$ ladder

In this section we present the methods and results of the wave-packet states preparation and the time evolution of 1-dimensional Lattice QED photon propagation and scattering processes. In particular, we apply the methods and results of the chapters 3 and 4 to

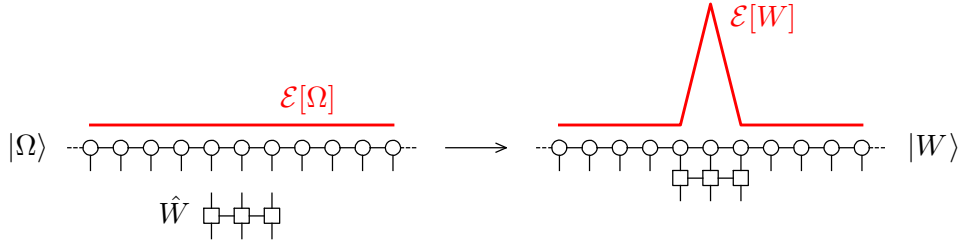


Figure 5.2. In order to prepare initial states, we apply an MPO to the vacuum obtained with DMRG. In this figure, we show schematically how a Wannier excitation operator in an MPO form is applied to the vacuum, obtaining a maximally localized state.

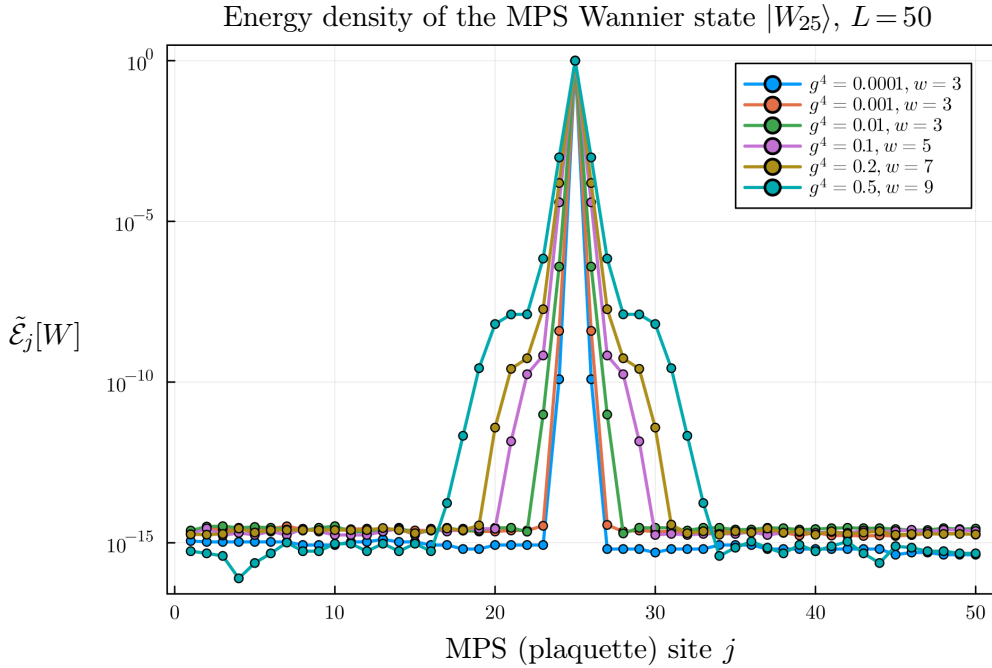


Figure 5.3. Energy density computed as (5.7) of the final MPS state obtained applying different Wannier MPO excitation operators for different g (from $g^4 = 0.0001$ to $g^4 = 0.5$) and different supports w on a 50-site ground-state MPS obtained with DMRG. The result is a Wannier MPS state $|W_{25}\rangle$ centered in 25-th site with different energy spread depending on the coupling g .

perform numerical simulations of out-of-equilibrium processes of the system described in chapter 2.

5.3.1 Preparation of the initial states

The first test is applying the Wannier excitation operator \hat{W}_j in an MPO form to the dressed vacuum obtained from DMRG (Fig. 5.2).

In order to visualize the energy distribution of the states, we compute the local energy density using the tensor contraction (5.7) for every MPS site $j = 1, \dots, L$.

Figure 5.3 shows the application of the Wannier excitation MPO for different values of the coupling and for different Wannier supports. The Wannier MPO is applied to a $L = 50$ ground-state MPS obtained with DMRG.

The energy density profiles are coherent with the results of section 3.2.7: as the coupling g increases, the energy spread of the Wannier increases accordingly to Fig. 3.3.

Another important remark is about the sizes of the system: indeed, the Wannier excitation operator was localized in an intermediate system size, up to $L = 13$, with periodic boundary conditions. Instead, the ground-state computed with DMRG represents a vacuum with open boundary conditions, approaching the thermodynamic limit. This means that finite system size effects at the boundaries can emerge when the MPO is inserted. This is what happens in Fig. 5.3, where for $g^4 = 0.5$ we clearly see a finite difference between the ground-state energy and the region outside the Wannier but inside the MPO support (the ‘‘Wannier vacuum’’).

However, these effects can be neglected for mainly two reasons:

- the graph of Fig. 5.3 has energy values represented in log-scale, hence the order of magnitude of the difference between the vacuum of DMRG and the vacuum of the Wannier remain very small ($\sim 10^{-7}$);
- the differences of the previous point can be neglected because after time evolution with TEBD, the error produced by the finite time-steps τ are of the same order of these border effects (about 10^{-7}), hence these very small effects are completely canceled by the real-time simulation.

5.3.2 Performing time evolution with TEBD

In order to perform time-evolution of the MPS, we apply the TEBD algorithm (see section 4.4). One could assert that, since (5.5) holds, the local Hamiltonian is not a 2-site operator, but a 3-site operator, so TEBD cannot be applied as described in section 4.4.

However, we notice that due to the structure of the electric field operators (5.1), for the spin representation $(\frac{1}{2}, 1)$ this is not a problem because we can recast Hamiltonian as a sum of local 2-sites operator:

$$\begin{aligned}
\hat{H} &= \sum \hat{H}_j \\
&= \sum \hat{H}_j^E + \hat{H}_j^B \\
&= \sum \left(\frac{1}{2} \begin{array}{|c|} \hline \uparrow \downarrow \\ \hline \end{array} + \begin{array}{|c|} \hline \uparrow \\ \hline \end{array} + \begin{array}{|c|} \hline \downarrow \\ \hline \end{array} + \frac{1}{2} \begin{array}{|c|} \hline \uparrow \downarrow \\ \hline \end{array} \right) + \begin{array}{|c|} \hline \uparrow \\ \hline \end{array} \\
&= \sum \left(\frac{1}{2} \begin{array}{|c|} \hline \uparrow \downarrow \\ \hline \end{array} + \begin{array}{|c|} \hline \uparrow \\ \hline \end{array} + \begin{array}{|c|} \hline \downarrow \\ \hline \end{array} \right) + \left(\frac{1}{2} \begin{array}{|c|} \hline \uparrow \downarrow \\ \hline \end{array} + \begin{array}{|c|} \hline \uparrow \\ \hline \end{array} \right) \\
&= \sum \begin{array}{|c|} \hline \uparrow \downarrow \\ \hline \end{array} + \begin{array}{|c|} \hline \uparrow \downarrow \\ \hline \end{array} \\
&= \sum \begin{array}{|c|} \hline \uparrow \downarrow \\ \hline \end{array}
\end{aligned} \tag{5.20}$$

However, we notice that there are generalizations of TEBD which allows for time evolution of Hamiltonians with local 3-site non-commuting terms [72]. Hence, even for higher spin representation, where the local Hamiltonian is a 3-site operator due to the 3-site \hat{U} operator, TEBD can in principle always be applied with a generalization of the evolution operator (4.39).

The parameters of the TEBD algorithm are the following:

- **the time step separation** τ : at each iteration step, the state $|\Psi(t)\rangle$ is updated to the state $|\Psi(t + \tau)\rangle$;
- **the SVD cutoff** ϵ , to perform the application of the gates: at each iteration, SVD is applied to each gate to re-obtain the MPS structure, and each singular value $< \epsilon$ is neglected, reducing the bond dimension;
- **maximum bond dimension** χ_{\max} : since at each iteration the bond dimension can increase, an upper limit of χ is set, avoiding the algorithm to be exceedingly slow;
- **total time steps** N ; after N iterations, the algorithm stops; alternatively, one can give as input the total simulation time $T = N \cdot \tau$.

Since the MPS Ansatz can adapt to systems only with *open boundary conditions* (OBC), here are some common types of boundary conditions:

1. **Dirichlet OBC**: the *values* of the function are explicitly specified and fixed during time-evolution at the boundaries;
2. **Neumann OBC**: specify the *derivative* of the function at the boundary; for instance, one can specify a gradient at the boundary or a derivative for a 1-dimensional system;
3. **Robin or mixed OBC**: these conditions involve *a combination* of Dirichlet and Neumann conditions; they typically involve a linear combination of the function value and its derivative at the boundary.

In the ladder case, we will use Dirichlet OBC. In particular, for the zero polarization sector of representation $\left(\frac{1}{2}, 1\right)$, which is that of our interest for the simulations, we can specify *parallel*



or *antiparallel* Dirichlet OBC:



Time evolution of the Wannier localized state with $g = 0.5$

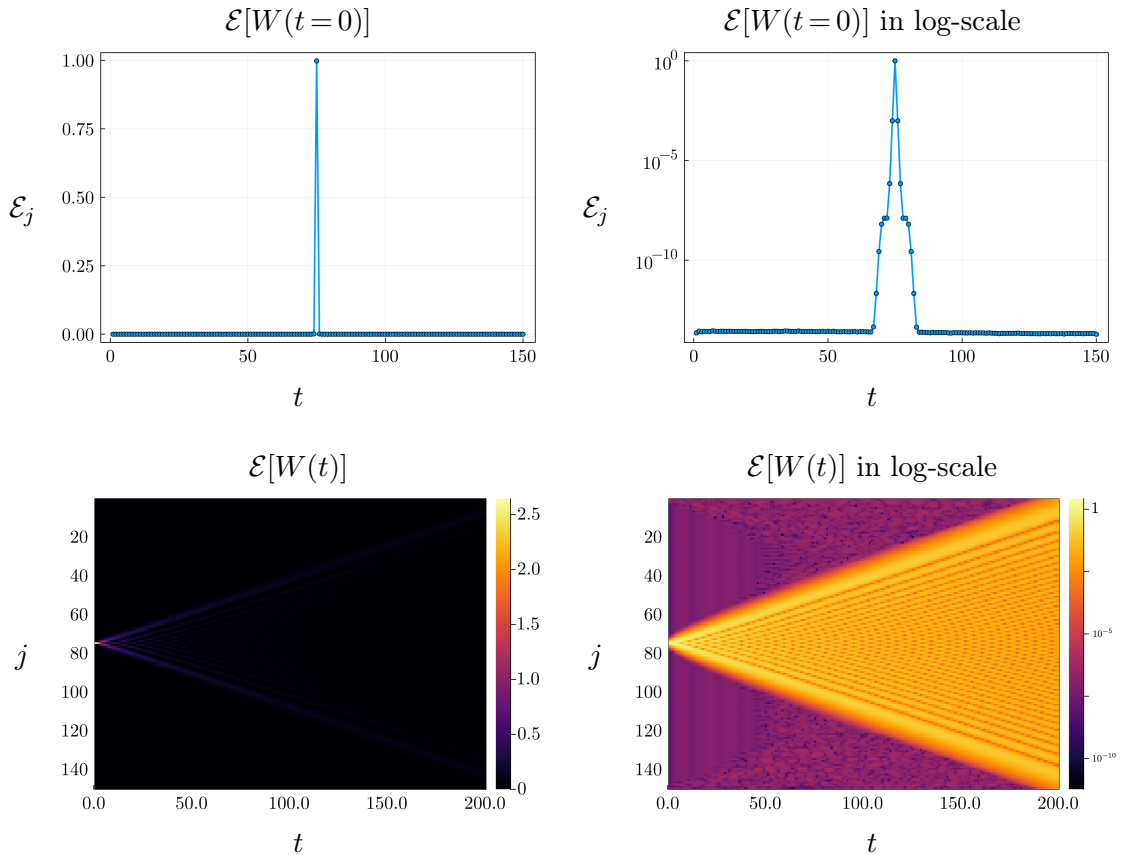


Figure 5.4. Simulation of the dispersion of a maximally localized Wannier state with TNs: an initial maximally localized state is prepared as described in section 5.3.1. The energy density (relative, with respect the ground-state, and normalized) as a function of spacetime plotted. The coupling is set at $g = 0.5$, while the parameters of the simulation are the time step $\tau = 0.05$, the SVD cutoff $\epsilon = 10^{-10}$ and the maximum bond dimension $\chi_{\max} = 30$.

Unless explicitly stated otherwise, from now on, we will use the parallel Dirichlet boundary conditions in all simulations of the following sections.

5.3.3 Dispersion of the localized Wannier state

To the initial Wannier state prepared as described in section 5.3.1 can be applied the time evolution with TEBD. Due to the uncertainty principle, the maximally localized state in the real space is the minimum localized state in the reciprocal space. Thus, we should observe a sudden dispersion whose boundary propagates at the maximum speed obtainable from the dispersion relation of the particle.

Fig. 5.4 shows the time evolution of in a system with $L = 150$, $g = 0.5$, where the localized state is prepared in the site $j = 75$.

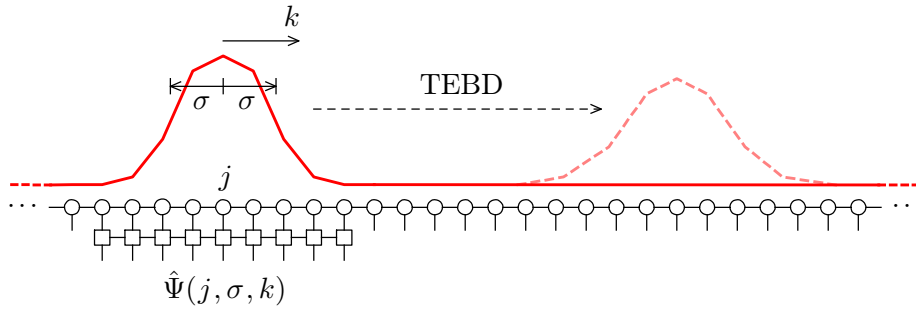


Figure 5.5. Schematic representation of a single-particle photon wave-packet state, generated from an MPO creation operator applied to the vacuum obtained with DMRG. After the state preparation, a time evolution algorithm such as TEBD is applied to simulate the propagation of the photon.

In the log-scale energy time evolution graph of Fig. 5.4, we can clearly see the causal cone whose vertex is at the spacetime $(j, t) = (75, 0)$.

5.3.4 Propagation of a single particle wave-packet

At this stage, we are ready to prepare a single-particle state using the wave-packet MPO creation operator described in section 5.2 to the ground-state, performing time evolution and testing the propagation of a one-dimensional photon. In particular, we prepare initial states corresponding to single-particle photonic Gaussian wave-packets, applying time evolution to study the properties of these wave-packets, such as the velocity and dispersion (Fig. 5.5).

Given a ground-state MPS with $L = 100$ sites, we prepare a Gaussian wave-packet with initial dispersion σ and momentum k , centered in a site \bar{j} of the one-dimensional chain

$\sigma = 3a$, $k = \frac{\pi}{2a}$ photonic Gaussian wave-packet propagation with $g = 0.1$

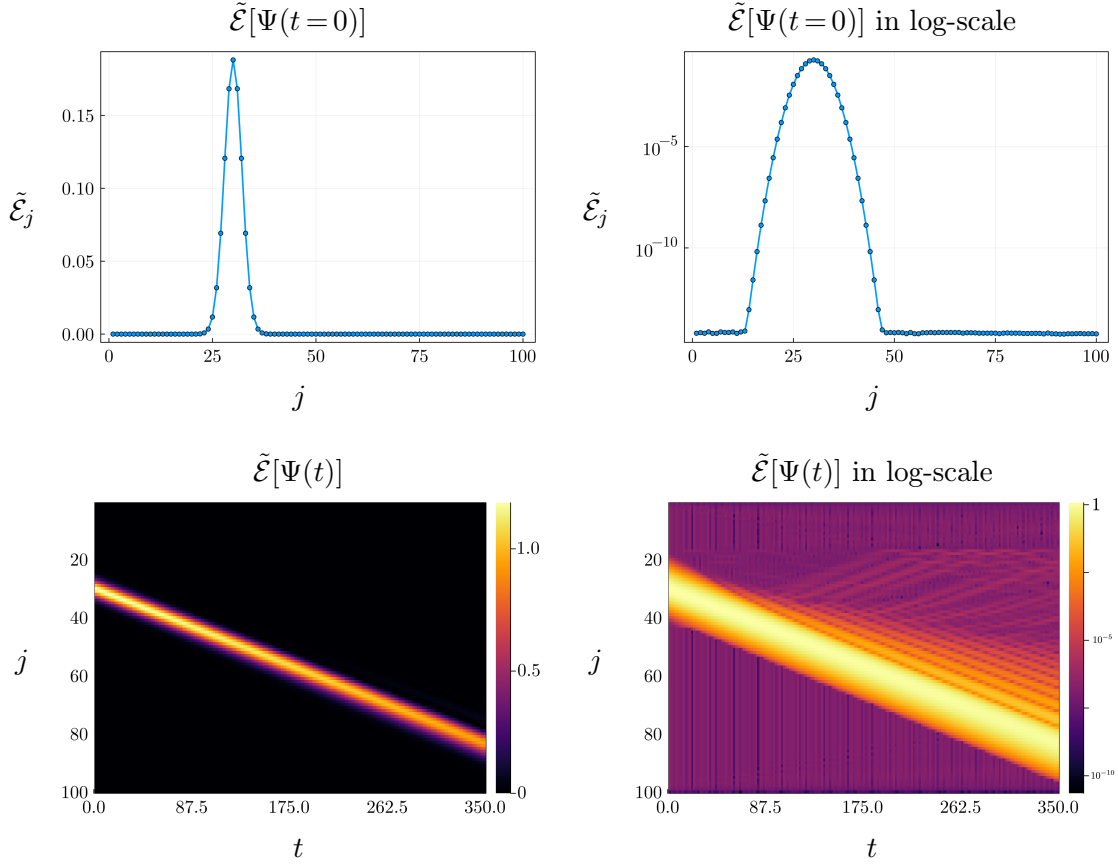


Figure 5.6. TN simulation of a single-particle photonic wave-packet propagation. The energy density (relative, with respect the ground-state, and normalized) as a function of spacetime plotted. The wave-packet state is prepared with $\bar{j} = 30$, $\sigma = 3a$ and $k = \pi/2a$ ($a = 1$). The coupling is set at $g = 0.1$, while the parameters of the simulation are the time step $\tau = 0.05$, the SVD cutoff $\epsilon = 10^{-10}$ and the maximum bond dimension $\chi_{\max} = 30$.

(Fig. 5.6). In order to study the time evolution as the parameters change, we can vary one of the three parameters σ , k , g while keeping the other two fixed.

Varying the coupling g . First, we analyze the velocity of the photon as a function of small values of the coupling g . In section 3.1.2 we found from perturbation theory the dispersion relation of the first energy band:

$$\mathcal{E}_1(k) = \text{const.} - \frac{g^2}{2a} \cos(ka) + \mathcal{O}(g^6). \quad (5.21)$$

Thus, as said in section 2.5.1, we can compute the *group velocity* of the particle as the first derivative of the energy with respect the momentum:

$$\beta(k) = \frac{d}{dk} \mathcal{E}_1(k) = \frac{g^2}{2} \sin(ka) + \mathcal{O}(g^6), \quad (5.22)$$

Local energy density $\mathcal{E}[\Psi(t)]$ with $\sigma = 2a$, $k = \frac{\pi}{2}$ varying the coupling g

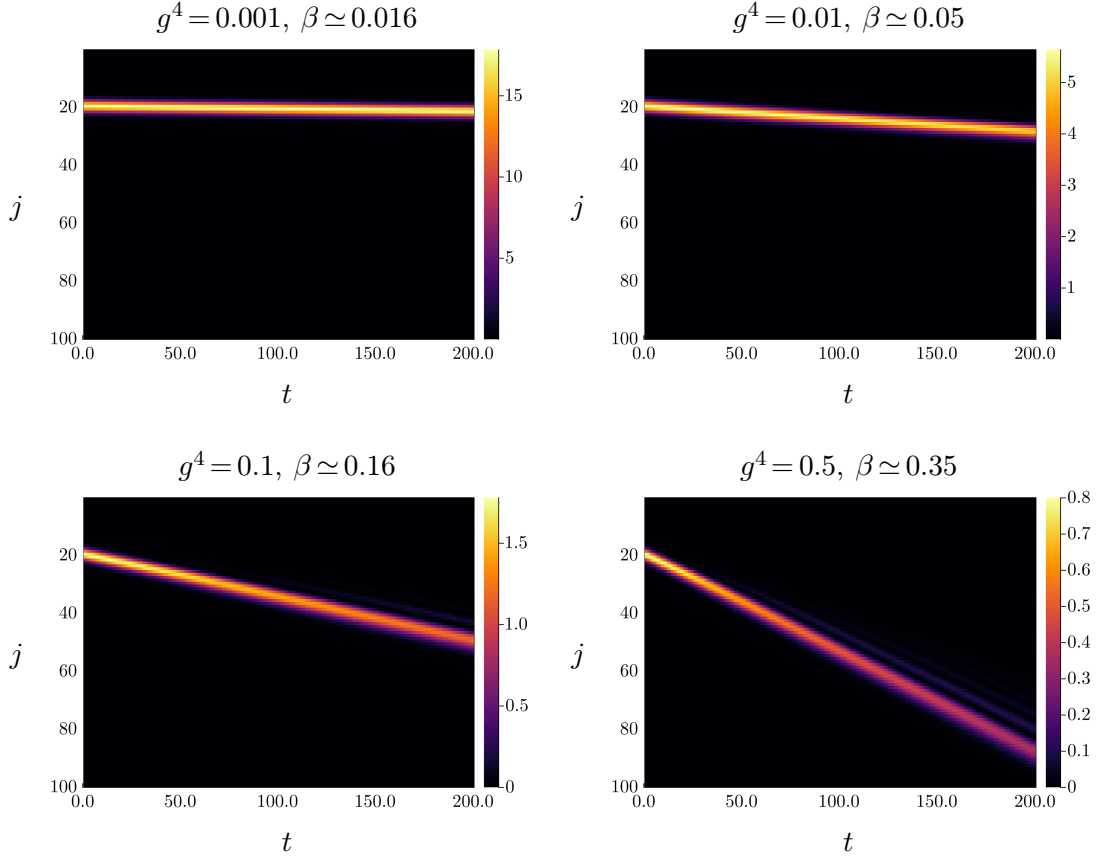


Figure 5.7. TN simulation of a single-particle photonic wave-packet propagation. The energy density (relative, with respect the ground-state, and normalized) as a function of spacetime plotted. The wave-packet state is prepared with $\bar{j} = 20$, $\sigma = 2a$ and $k = \pi/2a$ ($a = 1$). The coupling is varied from $g = 0.01$ to $g = 0.5$, while the parameters of the simulation are the time step $\tau = 0.05$, the SVD cutoff $\epsilon = 10^{-10}$ and the maximum bond dimension $\chi_{\max} = 30$.

while the dispersion coefficient is proportional to the second derivative

$$\beta'(k) = \frac{d^2}{dk^2} \mathcal{E}_1^{(1)}(k) = \frac{ag^2}{2} \cos(ka) + \mathcal{O}(g^6). \quad (5.23)$$

The minimum dispersion is at $\beta'(k) = 0$, so at $k = \pm\pi/2a$. This point of the Brillouin zone is also the point of maximum speed:

$$\beta\left(k = \frac{\pi}{2a}\right) = \frac{g^2}{2} + \mathcal{O}(g^6). \quad (5.24)$$

We can test these relations preparing a wave-packet with momentum $k = \pi/2a$, keeping constant all the parameters and varying only the coupling g (Fig. 5.7). We notice that the speed of the particle increases proportionally to g^2 , accordingly to the relation (5.24).

Varying the initial energy spread σ . Secondly, we study the dispersion of the

Local energy density $\mathcal{E}[\Psi(t)]$ with $g^4 = 0.1$, $k = \frac{\pi}{2}$ varying σ

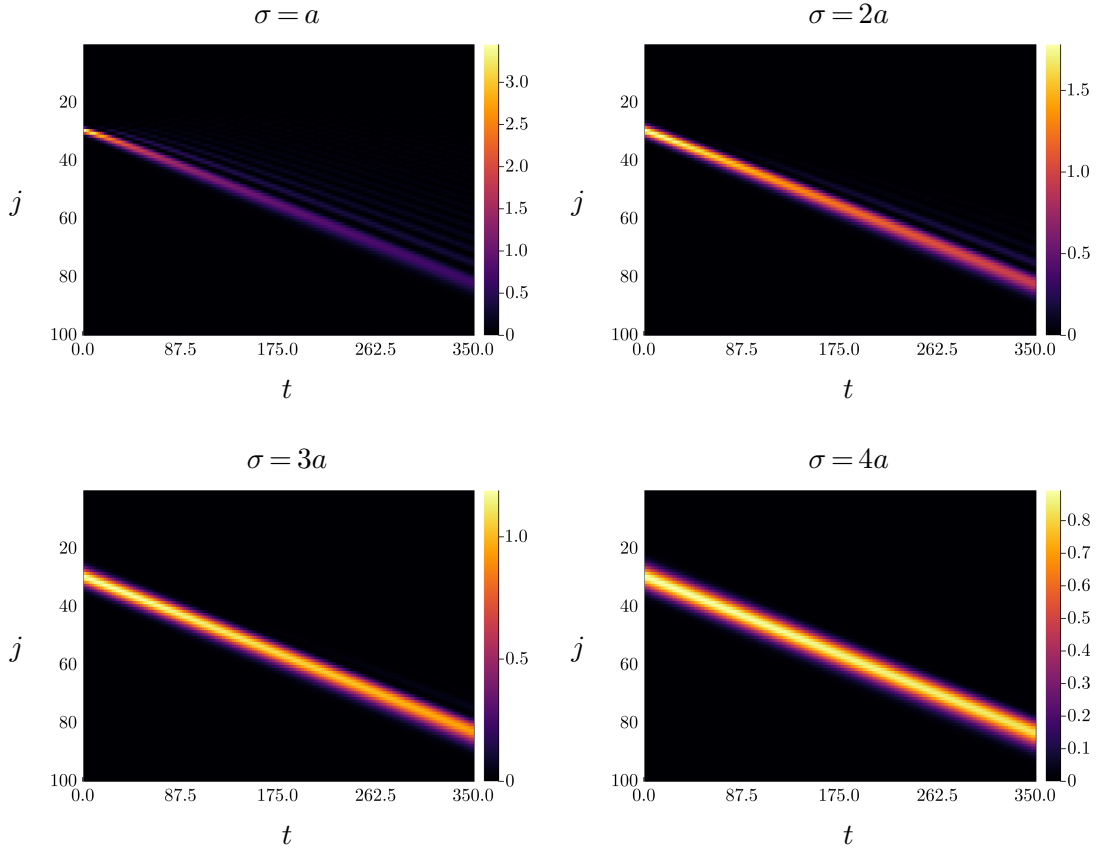


Figure 5.8. TN simulation of a single-particle photonic wave-packet propagation. The energy density (relative, with respect the ground-state, and normalized) as a function of spacetime plotted. The wave-packet state is prepared with $\bar{j} = 30$, $k = \pi/2$ (with $a = 1$) and varying $\sigma = a, 2a, 3a, 4a$. The coupling is fixed to $g = 0.1$ while the parameters of the simulation are the time step $\tau = 0.05$, the SVD cutoff $\epsilon = 10^{-10}$ and the maximum bond dimension $\chi_{\max} = 30$.

wave-packets varying the initial energy spread σ , keeping fixed the momentum k and the coupling g (Fig. 5.8). Clearly the velocity of the wave-packet does not depend on σ . Instead, for small spreads ($\sigma \sim a$) we notice a dispersion effects mainly due to lattice artifacts: we notice that behind the wave packet, additional “tails” are added as the packet propagates. These tails becomes smaller and smaller as the initial size of the wave-packet increases, and totally disappear for large values of the spread ($\sigma \gtrsim 4$). This is coherent with the uncertainty principle: the more σ is large, the more localized the wave-packet is in the reciprocal space, and the less the wave-packet is dispersive.

Varying the momentum k . The last parameter to test is the wave-packet momentum k . Fig. 5.9 shows a wave-packet with initial spread $\sigma = 3a$, with different values of k , evolved

Local energy density $\mathcal{E}[\Psi(t)]$ with $g^4 = 0.1$, $\sigma = 3a$ varying the momentum k

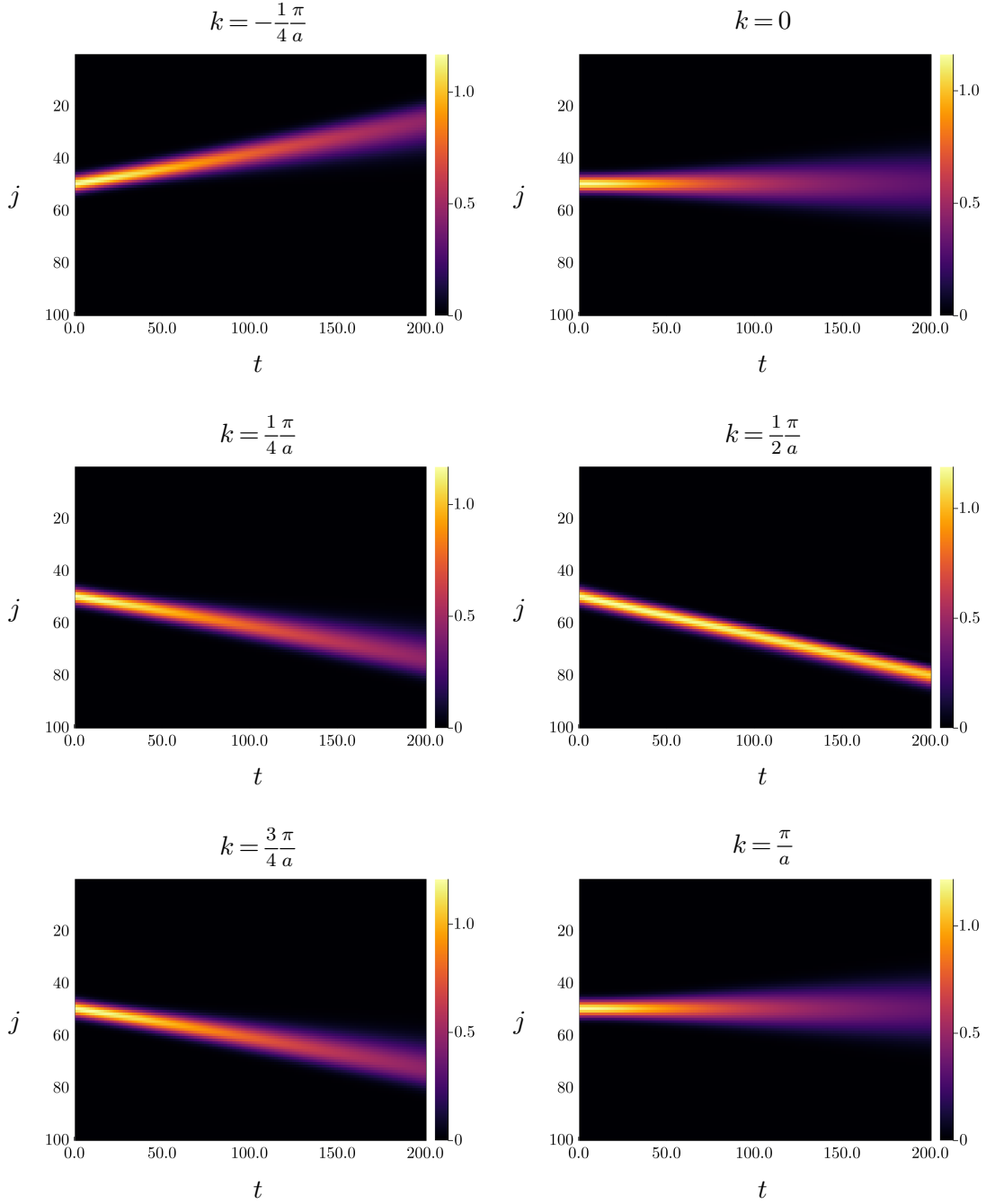


Figure 5.9. TN simulation of a single-particle photonic wave-packet propagation. The energy density (relative, with respect the ground-state, and normalized) as a function of spacetime plotted. The wave-packet state is prepared with $\bar{j} = 50$, $\sigma = 3a$ and varying k (we set $a = 1$). The coupling is fixed to $g = 0.1$ while the parameters of the simulation are the time step $\tau = 0.05$, the SVD cutoff $\epsilon = 10^{-10}$ and the maximum bond dimension $\chi_{\max} = 30$.

with a coupling $g = 0.1$. The behavior of the wave-packet is coherent with the dispersion relation (5.21): the points with maximum dispersion are $k = 0$ and $k = \pi/a$, which are opposite points in the Brillouin zone. The momenta for which there is minimal dispersion

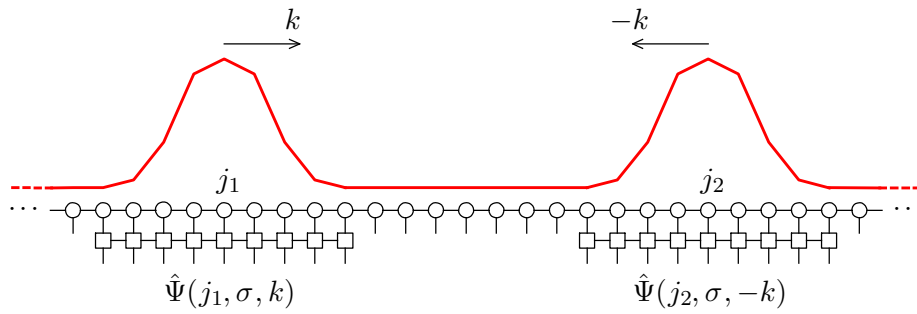


Figure 5.10. Schematic representation of a two-photon initial scattering state, generated from two MPO creation operators applied to the vacuum obtained with DMRG. After the state preparation, a time evolution algorithm such as TEBD is applied to simulate the scattering of the photons.

are instead $k = \pm\pi/2a$, for which the photon has also maximum velocity.

5.3.5 Photon-photon scattering

As previously anticipated, we now simulate a scattering process between two photons with opposite momenta: applying two wave-packet MPO creation operators in two different positions of the ground-state MPS, we can create an initial condition for a photon-photon scattering (Fig. 5.10).

Two $\sigma = 5a$, $|k| = \frac{\pi}{2}$ photonic Gaussian wave-packet scattering with $g = 0.5$

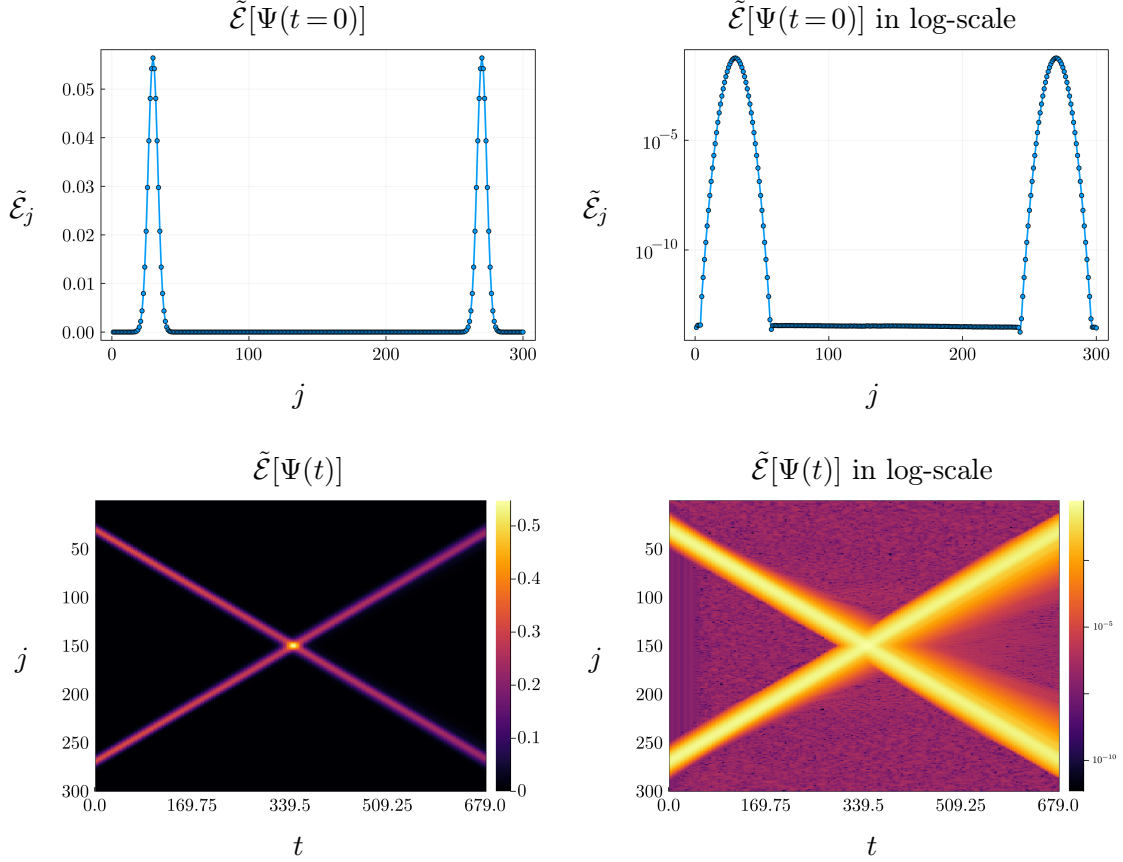


Figure 5.11. TN simulation of a two photonic wave-packet scattering. The energy density (relative, with respect the ground-state, and normalized) as a function of spacetime plotted. A system of $L = 300$ sites is used. The wave-packet states are prepared with $\bar{j}_1 = 30$ and $\bar{j}_2 = 300 - 30 = 270$, $\sigma = 5a$ and opposite momenta $k = \pm\pi/2a$ (we set $a = 1$). The coupling is set at $g = 0.1$, while the parameters of the simulation are the time step $\tau = 0.05$, the SVD cutoff $\epsilon = 10^{-10}$ and the maximum bond dimension $\chi_{\max} = 30$.

In order to have a large resolution of the scattering process, we construct a $L = 300$ sites ground-state MPS with DMRG, preparing two wave-packets with a large spread ($\sigma = 5a$), so that the wave-packets are enough localized in momentum space, and they are not subjected to dispersion and lattice artifacts during propagation. We prepare two wave-packets in a symmetric position with respect the center, but with opposite momenta $k = +\pi/2a$ and $k = -\pi/2a$. In this way, the scattering occur exactly at the center of the chain and the momentum is the one for which the dispersion (5.23) is the lowest.

We consider the highest value of the coupling g we are able to simulate: indeed, in section 3.3.6 we saw that using exact diagonalization with $L = 13$ we cannot exactly recreate a Wannier excitation operator with $g > 0.5$. Hence, $g = 0.5$ is the highest value of the coupling we can consider. In particular, this is the most interacting case we can simulate: if the photons in this regime are almost non-interacting, we can conclude that the photons of this theory are almost non-interacting also for values of $g < 0.5$.

Fig. 5.11 shows the results of the numerical simulation of a two-photon scattering. In the linear scale, we can see that the photon propagation is not perturbed after the scattering. From the energy plot in the log-scale, we can see weak effects: the propagation is perturbed also before the scattering, due to effects of photon self-interaction and lattice artifacts. After the scattering, we can see a weak increase of this phenomena, but further investigation such as computing the *entanglement entropy* would be needed to ensure that the two photons really weakly interacted.

Overall, this is a good result, because this is an evidence that these simulations are faithful with the absence of interaction: as said in the introductory chapter, the fact that the gauge fields do not interact in this theory is a straightforward consequence of the absence of matter in pure QED. In this context, as said in the previous sections, there are three phenomena that could make the interaction survive also without matter:

- a finite lattice spacing a : as stated in section 1.2.1 the lattice approximation brings extra terms proportional to corrections of powers of a in the Hamiltonian; these terms can bring to new higher order interaction terms of the gauge fields, even in absence of matter;
- a low dimensionality of the system: we know that the $(3 + 1)$ -dimensional QED is free under the condition of absence of matter; however, at least in principle, a different space dimensionality can consistently change the nature of the interaction, adding phenomena such as self-interaction of the gauge fields;
- the finite system size during exact diagonalization: in order to construct the maximally localized Wannier state, we had to apply exact diagonalization to a finite lattice system ($L \leq 13$); instead, the MPS dressed vacuum found with DMRG has been found using a large system size ($L \gg 13$); hence, the wave-packet MPO constructed inserted in this vacuum may be affected by these finite lattice size effects.

Chapter 6

Conclusion and Outlook

In this thesis, we described an algorithmic procedure to create one-dimensional single-particle wave-packets with definite momenta and size, and we applied it to a specific toy model relevant for High Energy Physics: the Quantum Link Model formulation of the Hamiltonian Lattice QED on ladder geometries in absence of fermionic degrees of freedom (pure QED). We have designed the procedure to be as possible model-independent, allowing for its implementation across different one-dimensional and quasi-one-dimensional Lattice Gauge Theories. In particular, the *inputs* of this algorithm are basically two: the translation operator \hat{T} of the one-dimensional lattice system, and the Hamiltonian \hat{H} of the theory, which we require to commute with \hat{T} , i.e. to be translationally invariant.

This algorithm exploits the tools of quantum technologies, in particular the framework of Tensor Network methods, presented in chapter 4. More precisely, the *output* of the wave-packet creation algorithm is a wave-packet in a Matrix Product Operator Ansatz form: it is applied to a large system size ($L \sim 10^2$) vacuum in a Matrix Product State form, found with the Density Matrix Renormalization Group algorithm. These MPS states are used as initial scattering states, ready to be time-evolved via standard TN techniques (TEBD or TDVP).

At the beginning of this work, we presented the $(2+1)$ -dimensional Lattice QED and its Quantum Link Model formulation. Hence, we studied the particular case of the ladder lattice geometry, computing all the gauge invariant configurations and defining all the relevant quantum operators of the system and the procedures to computationally construct them. Subsequently, we presented all the details of the construction procedure of the wave-packet creation operator, whose main points can be summed up as follows:

1. simultaneously diagonalizing the Hamiltonian \hat{H} and the translation operator \hat{T} with an intermediate system size ($L = 13$), finding the Bloch states $|k\rangle$ and the dispersion relation of the system;
2. selecting the single-particle states and computing the maximally localized state using a Wannier orbital function method; in this procedure, which is an optimization problem, we also showed that one can halve the parameters to optimize using symmetries of the reflection operator;
3. constructing a creation operator which generates the Wannier localized state when applied to the ground-state of the system (the dressed vacuum) from a sum of composition of localized gauge-invariant plaquette operators;

4. from a linear combination of the Wannier creation operators, constructing a localized wave-packets creation operator with definite average momenta k and average dispersion σ ;
5. converting the wave-packet creation operator of the previous step to an MPO, using well know techniques from Tensor Network methods.

In the final chapter, we performed real-time simulations of out-of-equilibrium processes of the lowest spin representation system, whose initial condition can be constructed creating photons from the vacuum using the wave-packet creation MPO. The real-time simulations of the propagation of single-photons successfully reproduce wave-packets which propagates almost dispersionlessly through the lattice. Some weak self-interaction effects of the photons are probably caused by lattice artifacts or by the low dimensionality of the system. For enough low coupling values, which are coherent with the one-dimensional Lattice QED, the photon-photon scattering simulations reproduce almost non-interacting photons, in accordance with the absence of interaction, which is a direct consequence of the absence of matter in QED. This observation actually warrants repeating our simulation experiment adding also dynamical matter.

Some interesting directions originating from this work include short and long-term projects. Some of the short-term goals, linked to the specific toy model of this work, are:

- implementing the algorithm for higher spin representations, simulating QED processes increasing the degrees of freedom of the gauge fields;
- adding matter (the fermionic degrees of freedom) to the ladder system, allowing the creation of QED charged particles (electrons and positrons); preparing electron-photon initial scattering states, simulating Compton-like processes.

Some of the more long-term goals are instead:

- implementing the algorithm for the one-dimensional QCD, creating single-particle wave-packets of QCD bound states, simulating meson-meson scattering;
- exploring different quasi one-dimensional geometries such as strips and tubular geometries, allowing for electron and photon wave-packet states with a definite chirality;
- understand the extent of applicability of our model-independent method, in pursuit of more complex gauge or non-gauge lattice models; for instance, we could substitute the exact diagonalization part, which is the most computationally involving, with something more flexible, such as Lanczos methods;
- generalizing the wave-packet creation to higher dimensional lattices, towards constructing initial states for two-dimensional scattering processes.

Bibliography

- [1] Steven Weinberg. *The Quantum Theory of Fields*. Cambridge University Press, June 1995. <https://doi.org/10.1017/cbo9781139644167>.
- [2] Michael E. Peskin. *An Introduction To Quantum Field Theory*. CRC Press, May 2018. <https://doi.org/10.1201/9780429503559>.
- [3] David J. Gross. Twenty five years of asymptotic freedom. *Nuclear Physics B - Proceedings Supplements*, 74 (1-3): 426–446, March 1999. [https://doi.org/10.1016/s0920-5632\(99\)00208-x](https://doi.org/10.1016/s0920-5632(99)00208-x). Publisher: Elsevier BV.
- [4] Anastasia Doikou, Stefano Evangelisti, Giovanni Feverati, and Nikos Karaiskos. Introduction To Quantum Integrability. *International Journal of Modern Physics A*, 25 (17): 3307–3351, July 2010. <https://doi.org/10.1142/s0217751x10049803>. Publisher: World Scientific Pub Co Pte Lt.
- [5] Heinz J. Rothe. *Lattice Gauge Theories*. WORLD SCIENTIFIC, March 2012. <https://doi.org/10.1142/8229>.
- [6] Rajan Gupta. Introduction to Lattice QCD, 1998. <https://arxiv.org/abs/hep-lat/9807028>.
- [7] Kenneth G. Wilson. Confinement of quarks. *Physical Review D*, 10 (8): 2445–2459, October 1974. <https://doi.org/10.1103/physrevd.10.2445>. Publisher: American Physical Society (APS).
- [8] Martin Hilbert and Priscila López. The World’s Technological Capacity to Store, Communicate, and Compute Information. *Science*, 332 (6025): 60–65, April 2011. <https://www.science.org/doi/10.1126/science.1200970>. Publisher: American Association for the Advancement of Science.
- [9] Michael Creutz. Monte Carlo study of quantized SU(2) gauge theory. *Physical Review D*, 21 (8): 2308–2315, April 1980. <https://doi.org/10.1103/physrevd.21.2308>. Publisher: American Physical Society (APS).
- [10] Don Weingarten. Monte Carlo evaluation of hadron masses in lattice gauge theories with fermions. *Physics Letters B*, 109 (1-2): 57–62, February 1982. [https://doi.org/10.1016/0370-2693\(82\)90463-4](https://doi.org/10.1016/0370-2693(82)90463-4). Publisher: Elsevier BV.
- [11] E. Y. Loh, J. E. Gubernatis, R. T. Scalettar, S. R. White, D. J. Scalapino, and R. L. Sugar. Sign problem in the numerical simulation of many-electron systems. *Physical Review B*, 41 (13): 9301–9307, May 1990. <https://doi.org/10.1103/physrevb.41.9301>. Publisher: American Physical Society (APS).
- [12] Matthias Troyer and Uwe-Jens Wiese. Computational Complexity and Fundamental Limitations to Fermionic Quantum Monte Carlo Simulations. *Physical Review Letters*, 94 (17), May 2005. <https://doi.org/10.1103/physrevlett.94.170201>. Publisher: American Physical Society (APS).
- [13] C. H. Bennett and P. W. Shor. Quantum information theory. *IEEE Transactions on Information Theory*, 44 (6): 2724–2742, 1998. <https://doi.org/10.1109/18.720553>. Publisher: Institute of Electrical and Electronics Engineers (IEEE).
- [14] I. M. Georgescu, S. Ashhab, and Franco Nori. Quantum simulation. *Reviews of Modern Physics*, 86 (1): 153–185, March 2014. <https://link.aps.org/doi/10.1103/RevModPhys.86.153>. Publisher: American Physical Society.
- [15] Jiajun Chen. Review on Quantum Communication and Quantum Computation. *Journal of Physics: Conference Series*, 1865 (2): 022008, April 2021. .

- <https://dx.doi.org/10.1088/1742-6596/1865/2/022008>. Publisher: IOP Publishing.
- [16] C. L. Degen, F. Reinhard, and Paola Cappellaro. Quantum sensing. *APS*, July 2017. .
<https://dspace.mit.edu/handle/1721.1/124553>. Accepted: 2020-04-09T13:23:04Z Publisher:
 American Physical Society (APS).
- [17] M. C. Bañuls, Rainer Blatt, Jacopo Catani, Alessio Celi, Juan Ignacio Cirac, Marcello Dalmonte, Leonardo Fallani, Karl Jansen, Maciej Lewenstein, Simone Montangero, Christine A. Muschik, Benni Reznik, Enrique Rico, Luca Tagliacozzo, Karel Van Acoleyen, Frank Verstraete, Uwe-Jens Wiese, Matthew Wingate, Jakub Zakrzewski, and Peter Zoller. Simulating lattice gauge theories within quantum technologies. *The European Physical Journal D*, 74 (8), August 2020.
<https://doi.org/10.1140/epjd/e2020-100571-8>. Publisher: Springer Science and Business Media LLC.
- [18] U.-J. Wiese. Ultracold quantum gases and lattice systems: quantum simulation of lattice gauge theories. *Annalen der Physik*, 525 (10-11): 777–796, July 2013.
<https://doi.org/10.1002/andp.201300104>. Publisher: Wiley.
- [19] Mari Carmen Banuls, Krzysztof Cichy, J. Ignacio Cirac, Karl Jansen, and Stefan Kühn. Tensor Networks and their use for Lattice Gauge Theories. In *Proceedings of The 36th Annual International Symposium on Lattice Field Theory — PoS(LATTICE2018)*, volume 334, page 022. SISSA Medialab, May 2019. <https://pos.sissa.it/334/022>. Conference Name: The 36th Annual International Symposium on Lattice Field Theory.
- [20] Richard P. Feynman. Simulating physics with computers. *International Journal of Theoretical Physics*, 21 (6-7): 467–488, June 1982. <https://doi.org/10.1007/bf02650179>. Publisher: Springer Science and Business Media LLC.
- [21] Francesco Tacchino, Alessandro Chiesa, Stefano Carretta, and Dario Gerace. Quantum Computers as Universal Quantum Simulators: State-of-the-Art and Perspectives. *Advanced Quantum Technologies*, 3 (3): 1900052, December 2019. <https://doi.org/10.1002/qute.201900052>. Publisher: Wiley.
- [22] Zohreh Davoudi, Mohammad Hafezi, Christopher Monroe, Guido Pagano, Alireza Seif, and Andrew Shaw. Towards analog quantum simulations of lattice gauge theories with trapped ions. *Physical Review Research*, 2 (2), April 2020. <https://doi.org/10.1103/physrevresearch.2.023015>. Publisher: American Physical Society (APS).
- [23] D. Marcos, P. Widmer, E. Rico, M. Hafezi, P. Rabl, U. J. Wiese, and P. Zoller. Two-dimensional lattice gauge theories with superconducting quantum circuits. *Annals of Physics*, 351: 634–654, December 2014. . <https://www.sciencedirect.com/science/article/pii/S0003491614002711>.
- [24] A. Mezzacapo, E. Rico, C. Sabín, I. L. Egusquiza, L. Lamata, and E. Solano. Non-Abelian SU(2) Lattice Gauge Theories in Superconducting Circuits. *Physical Review Letters*, 115 (24), December 2015. <https://doi.org/10.1103/physrevlett.115.240502>. Publisher: American Physical Society (APS).
- [25] Immanuel Bloch, Jean Dalibard, and Sylvain Nascimbène. Quantum simulations with ultracold quantum gases. *Nature Physics*, 8 (4): 267–276, April 2012. .
<https://www.nature.com/articles/nphys2259>. Number: 4 Publisher: Nature Publishing Group.
- [26] Esteban A. Martinez, Christine A. Muschik, Philipp Schindler, Daniel Nigg, Alexander Erhard, Markus Heyl, Philipp Hauke, Marcello Dalmonte, Thomas Monz, Peter Zoller, and Rainer Blatt. Real-time dynamics of lattice gauge theories with a few-qubit quantum computer. *Nature*, 534 (7608): 516–519, June 2016. <https://doi.org/10.1038/nature18318>. Publisher: Springer Science and Business Media LLC.
- [27] John Kogut and Leonard Susskind. Hamiltonian formulation of Wilson’s lattice gauge theories. *Physical Review D*, 11 (2): 395–408, January 1975. <https://doi.org/10.1103/physrevd.11.395>. Publisher: American Physical Society (APS).

- [28] Leonard Susskind. Lattice fermions. *Physical Review D*, 16 (10): 3031–3039, November 1977. <https://doi.org/10.1103/physrevd.16.3031>. Publisher: American Physical Society (APS).
- [29] S. Chandrasekharan and U.-J. Wiese. Quantum link models: A discrete approach to gauge theories. *Nuclear Physics B*, 492 (1): 455–471, 1997. . <https://www.sciencedirect.com/science/article/pii/S0550321397800417>.
- [30] John Preskill. Quantum Computing in the NISQ era and beyond. *Quantum*, 2: 79, August 2018. <https://quantum-journal.org/papers/q-2018-08-06-79/>. Publisher: Verein zur Förderung des Open Access Publizierens in den Quantenwissenschaften.
- [31] Román Orús. Tensor networks for complex quantum systems. *Nature Reviews Physics*, 1 (9): 538–550, September 2019. . <https://www.nature.com/articles/s42254-019-0086-7>. Number: 9 Publisher: Nature Publishing Group.
- [32] J. Eisert, M. Cramer, and M. B. Plenio. Colloquium: Area laws for the entanglement entropy. *Reviews of Modern Physics*, 82 (1): 277–306, February 2010. <https://doi.org/10.1103/revmodphys.82.277>. Publisher: American Physical Society (APS).
- [33] Román Orús. A practical introduction to tensor networks: Matrix product states and projected entangled pair states. *Annals of Physics*, 349: 117–158, October 2014. <https://doi.org/10.1016/j.aop.2014.06.013>. Publisher: Elsevier BV.
- [34] M. C. Bañuls, Krzysztof Cichy, J. Ignacio Cirac, Karl Jansen, Stefan Kühn, and Hana Saito. Towards overcoming the Monte Carlo sign problem with tensor networks. *EPJ Web of Conferences*, 137: 04001, 2017. <https://doi.org/10.1051/epjconf/201713704001>. Publisher: EDP Sciences.
- [35] Roman Pasechnik and Michal Šumbera. Phenomenological Review on Quark–Gluon Plasma: Concepts vs. Observations. *Universe*, 3 (1): 7, March 2017. . <https://www.mdpi.com/2218-1997/3/1/7>. Number: 1 Publisher: Multidisciplinary Digital Publishing Institute.
- [36] Mark G. Alford, Andreas Schmitt, Krishna Rajagopal, and Thomas Schäfer. Color superconductivity in dense quark matter. *Reviews of Modern Physics*, 80 (4): 1455–1515, November 2008. <https://link.aps.org/doi/10.1103/RevModPhys.80.1455>. Publisher: American Physical Society.
- [37] T. Pichler, M. Dalmonte, E. Rico, P. Zoller, and S. Montangero. Real-Time Dynamics in U(1) Lattice Gauge Theories with Tensor Networks. *Physical Review X*, 6 (1): 011023, March 2016. <https://link.aps.org/doi/10.1103/PhysRevX.6.011023>. Publisher: American Physical Society.
- [38] Marco Rigobello. Scattering Processes via Tensor Network Simulations. Master’s thesis, Università degli Studi di Padova, 2020.
- [39] M. C. Bañuls, K. Cichy, J. I. Cirac, and K. Jansen. The mass spectrum of the Schwinger model with matrix product states. *Journal of High Energy Physics*, 2013 (11), November 2013. [https://doi.org/10.1007/jhep11\(2013\)158](https://doi.org/10.1007/jhep11(2013)158). Publisher: Springer Science and Business Media LLC.
- [40] Giuseppe Magnifico, Timo Felser, Pietro Silvi, and Simone Montangero. Lattice quantum electrodynamics in (3+1)-dimensions at finite density with tensor networks. *Nature Communications*, 12 (1), June 2021. <https://doi.org/10.1038/s41467-021-23646-3>. Publisher: Springer Science and Business Media LLC.
- [41] Pietro Silvi, Enrique Rico, Marcello Dalmonte, Ferdinand Tschirsich, and Simone Montangero. Finite-density phase diagram of a (1+1)-d non-abelian lattice gauge theory with tensor networks. *Quantum*, 1: 9, April 2017. <https://doi.org/10.22331/q-2017-04-25-9>.
- [42] Giovanni Cataldi, Giuseppe Magnifico, Pietro Silvi, and Simone Montangero. (2+1)D SU(2) Yang-Mills Lattice Gauge Theory at finite density via tensor networks, 2023. <https://arxiv.org/abs/2307.09396>.
- [43] Maarten Van Damme, Laurens Vanderstraeten, Jacopo De Nardis, Jutho Haegeman, and Frank Verstraete. Real-time scattering of interacting quasiparticles in quantum spin chains. *Physical Review Research*, 3 (1), January 2021. <https://doi.org/10.1103/physrevresearch.3.013078>. Publisher:

- American Physical Society (APS).
- [44] Marco Rigobello, Simone Notarnicola, Giuseppe Magnifico, and Simone Montangero. Entanglement generation in (1+1)D QED scattering processes. *Physical Review D*, 104 (11), December 2021. <https://doi.org/10.1103/physrevd.104.114501>. Publisher: American Physical Society (APS).
 - [45] Nicola Marzari and David Vanderbilt. Maximally localized generalized Wannier functions for composite energy bands. *Physical Review B*, 56 (20): 12847–12865, November 1997. <https://doi.org/10.1103/physrevb.56.12847>. Publisher: American Physical Society (APS).
 - [46] Nicola Marzari, Arash A. Mostofi, Jonathan R. Yates, Ivo Souza, and David Vanderbilt. Maximally localized Wannier functions: Theory and applications. *Reviews of Modern Physics*, 84 (4): 1419–1475, October 2012. <https://doi.org/10.1103/revmodphys.84.1419>. Publisher: American Physical Society (APS).
 - [47] Jens Nyhegn, Chia-Min Chung, and Michele Burrello. Zn lattice gauge theory in a ladder geometry. *Physical Review Research*, 3 (1), February 2021. <https://doi.org/10.1103/physrevresearch.3.013133>. Publisher: American Physical Society (APS).
 - [48] Sunny Pradhan, Andrea Maroncelli, and Elisa Ercolessi. Discrete Abelian lattice gauge theories on a ladder and their dualities with quantum clock models, 2022. <https://arxiv.org/abs/2208.04182>.
 - [49] David Bosch. The Theory of (2+1)-Dimensional Quantum Electrodynamics and Corresponding β -Function, 2018. https://fse.studenttheses.ub.rug.nl/17757/1/bPHYS_2018_BoschDavid.pdf.
 - [50] Anatoly V. Kotikov and Sofian Teber. Critical Behavior of (2+1)-Dimensional QED: $1/N$ Expansion. *Particles*, 3 (2): 345–354, April 2020. <https://doi.org/10.3390/particles3020026>. Publisher: MDPI AG.
 - [51] Rocco Maggi, Elisa Ercolessi, Paolo Facchi, Giuseppe Marmo, Saverio Pascazio, and Francesco V. Pepe. Dimensional reduction of electromagnetism. *Journal of Mathematical Physics*, 63 (2): 022902, February 2022. <https://doi.org/10.1063/5.0079363>. Publisher: AIP Publishing.
 - [52] Julian Schwinger. Gauge Invariance and Mass. II. *Physical Review*, 128 (5): 2425–2429, December 1962. <https://doi.org/10.1103/physrev.128.2425>. Publisher: American Physical Society (APS).
 - [53] Gregory H. Wannier. The Structure of Electronic Excitation Levels in Insulating Crystals. *Physical Review*, 52 (3): 191–197, August 1937. <https://doi.org/10.1103/physrev.52.191>. Publisher: American Physical Society (APS).
 - [54] Pietro Silvi, Ferdinand Tschirsich, Matthias Gerster, Johannes Jünemann, Daniel Jaschke, Matteo Rizzi, and Simone Montangero. The Tensor Networks Anthology: Simulation techniques for many-body quantum lattice systems. *SciPost Physics Lecture Notes*, March 2019. <https://doi.org/10.21468/scipostphyslectnotes.8>. Publisher: Stichting SciPost.
 - [55] Naoki Nakatani and Garnet Kin-Lic Chan. Efficient tree tensor network states (TTNS) for quantum chemistry: Generalizations of the density matrix renormalization group algorithm. *The Journal of Chemical Physics*, 138 (13), April 2013. <https://doi.org/10.1063/1.4798639>. Publisher: AIP Publishing.
 - [56] E. Miles Stoudenmire and David J. Schwab. Supervised Learning with Quantum-Inspired Tensor Networks, 2016. <https://arxiv.org/abs/1605.05775>. Publisher: arXiv.
 - [57] I. V. Oseledets. Tensor-Train Decomposition. *SIAM Journal on Scientific Computing*, 33 (5): 2295–2317, January 2011. <https://epubs.siam.org/doi/abs/10.1137/090752286>. Publisher: Society for Industrial and Applied Mathematics.
 - [58] F. Fröwis, V. Nebendahl, and W. Dur. Tensor operators: Constructions and applications for long-range interaction systems. *Physical Review A*, 81 (6), June 2010. <https://doi.org/10.1103/physreva.81.062337>. Publisher: American Physical Society (APS).
 - [59] Steven R. White. Density matrix formulation for quantum renormalization groups. *Physical Review Letters*, 69 (19): 2863–2866, November 1992. <https://doi.org/10.1103/physrevlett.69.2863>.

Publisher: American Physical Society (APS).

- [60] Leo P. Kadanoff. Scaling laws for ising models near $\{T\}_c$. *Physics Physique Fizika*, 2 (6): 263–272, June 1966. <https://link.aps.org/doi/10.1103/PhysicsPhysiqueFizika.2.263>. Publisher: American Physical Society.
- [61] Kenneth G. Wilson. Renormalization Group and Critical Phenomena. I. Renormalization Group and the Kadanoff Scaling Picture. *Physical Review B*, 4 (9): 3174–3183, November 1971. <https://link.aps.org/doi/10.1103/PhysRevB.4.3174>. Publisher: American Physical Society.
- [62] U. Schollwöck. The density-matrix renormalization group. *Reviews of Modern Physics*, 77 (1): 259–315, April 2005. <https://link.aps.org/doi/10.1103/RevModPhys.77.259>. Publisher: American Physical Society.
- [63] Ulrich Schollwöck. The density-matrix renormalization group in the age of matrix product states. *Annals of Physics*, 326 (1): 96–192, January 2011. . <https://www.sciencedirect.com/science/article/pii/S0003491610001752>.
- [64] Cornelius Lanczos. An iteration method for the solution of the eigenvalue problem of linear differential and integral operators. *J. Res. Natl. Bur. Stand. B*, 45: 255–282, 1950.
- [65] Sebastian Paeckel, Thomas Köhler, Andreas Swoboda, Salvatore R. Manmana, Ulrich Schollwöck, and Claudius Hubig. Time-evolution methods for matrix-product states. *Annals of Physics*, 411: 167998, December 2019. . <https://www.sciencedirect.com/science/article/pii/S0003491619302532>.
- [66] Steven R. White and Adrian E. Feiguin. Real-Time Evolution Using the Density Matrix Renormalization Group. *Physical Review Letters*, 93 (7): 076401, August 2004. <https://link.aps.org/doi/10.1103/PhysRevLett.93.076401>. Publisher: American Physical Society.
- [67] Guifré Vidal. Efficient Simulation of One-Dimensional Quantum Many-Body Systems. *Physical Review Letters*, 93 (4): 040502, July 2004. <https://link.aps.org/doi/10.1103/PhysRevLett.93.040502>. Publisher: American Physical Society.
- [68] Jutho Haegeman, J. Ignacio Cirac, Tobias J. Osborne, Iztok Pizorn, Henri Verschelde, and Frank Verstraete. Time-Dependent Variational Principle for Quantum Lattices. *Physical Review Letters*, 107 (7): 070601, August 2011. <https://link.aps.org/doi/10.1103/PhysRevLett.107.070601>. Publisher: American Physical Society.
- [69] Masuo Suzuki. Generalized Trotter’s formula and systematic approximants of exponential operators and inner derivations with applications to many-body problems. *Communications in Mathematical Physics*, 51 (2): 183–190, June 1976. . <https://doi.org/10.1007/BF01609348>.
- [70] Giovanni Cataldi, Ashkan Abedi, Giuseppe Magnifico, Simone Notarnicola, Nicola Dalla Pozza, Vittorio Giovannetti, and Simone Montangero. Hilbert curve vs Hilbert space: exploiting fractal 2D covering to increase tensor network efficiency. *Quantum*, 5: 556, September 2021. <https://doi.org/10.22331/q-2021-09-29-556>. Publisher: Verein zur Förderung des Open Access Publizierens in den Quantenwissenschaften.
- [71] G. Vidal. Entanglement Renormalization. *Physical Review Letters*, 99 (22): 220405, November 2007. <https://link.aps.org/doi/10.1103/PhysRevLett.99.220405>. Publisher: American Physical Society.
- [72] Thomas Barthel and Yikang Zhang. Optimized Lie–Trotter–Suzuki decompositions for two and three non-commuting terms. *Annals of Physics*, 418: 168165, July 2020. . <https://www.sciencedirect.com/science/article/pii/S0003491620300981>.